

# "MOISTURE AND ENERGY DYNAMICS IN FIELD SOILS: THE INFLUENCE OF THE DIURNAL CYCLE"

THÈSE N° 6015 (2014)

PRÉSENTÉE LE 15 JANVIER 2014

À LA FACULTÉ DE L'ENVIRONNEMENT NATUREL, ARCHITECTURAL ET CONSTRUIT  
LABORATOIRE DE MÉCANIQUE DES FLUIDES DE L'ENVIRONNEMENT  
PROGRAMME DOCTORAL EN MÉCANIQUE

ÉCOLE POLYTECHNIQUE FÉDÉRALE DE LAUSANNE

POUR L'OBTENTION DU GRADE DE DOCTEUR ÈS SCIENCES

PAR

Francesco CIOCCA

acceptée sur proposition du jury:

Prof. F. Golay, président du jury  
Prof. M. Parlange, Prof. I. Lunati, directeurs de thèse  
Prof. A. Berne, rapporteur  
Prof. S. W. Tyler, rapporteur  
Prof. N. C. van de Giesen, rapporteur



ÉCOLE POLYTECHNIQUE  
FÉDÉRALE DE LAUSANNE

Suisse  
2013



A chi, vicino o distante, ha sempre corso con me ...



# Acknowledgements

I want to address the first big thanks to my advisors, Prof. Ivan Lunati and Prof. Marc Parlange, for having faith in me since the very beginning giving me the chance for a ride on this crazy roller-coaster that is the doctorate.

In particular I am grateful to Ivan for the constant presence, the discussions not only about science, the help and the richness of meaningful suggestions; and to Marc for the support, the incredible enthusiasm that he always transmitted me about both research and running and for his attempts to make me feel forever young ("no problem Francesco, you can do it, you are young..").

Then I express my most sincere thanks to the Professors and Researchers together with I had the privilege to discuss, collaborate, share ideas and enrich my scientific knowledge. I am referring to Shmuel Assouline, who put his immense theoretical and practical experience so often at my disposal; Nick van de Giesen and his crew from Delft (Koen, Stejin, Jop) for the invaluable help with the fiber optics in the lysimeter, Jan Hopmans for having introduced me to the world of the needle heat-pulse probes, Damien Jougnot for the precious suggestions and clear explanations about soil science, Scott Tyler and John Selker for the great c'Temps meetings in Stanford, Andrea Rinaldo for all the important advices. Marc, Ivan, Nick and Scott have been members of my thesis committee; beside them, I also want to thank François Golay and Alexis Berne, the other members.

Moreover, I want to thank the Swiss National Science Foundation for the generous support.

I am a bit sad because my poor english does not allow me properly thanking all my present and former colleagues at the EFLUM. These years would have never been the same without amazing officemates such as Daniel Nadeau ("Daaaaan"), Todor Dinoev and Holly Oldroyd, together with I shared happiness and frustration, satisfactions and disappointments. You stood my dumps, I owe you a beer, and I promise I will water the office plants from now on..

Beside them, a very special thank is addressed to Theo and Raph, close friends and unique traveling companions here and abroad, to Hendrik and his incredible knowledge on field work,

## Acknowledgements

---

to Steven that never refused to answer my (more than often trivial) questions, and to Natalie, Giometz, Susanna, Martin, Thierry, Simone, Silvia, Chad, Nikki, Vincent, Jan, Valentin, all the guys from CRYOS lab. and my apologies to those I am surely forgetting (hopefully no one), I am likely less young than what Marc thinks..

And I know guys that I have almost never come for lunch with you, sometimes because you were eating too early for the Italian customs, more often because bad-people, to who I sincerely express my gratitude, were forcing me to go out for running: especially Michaello, avec lequel j'ai eu la chance de partager la plus longue course, du début à la fin du doctorat ; mais aussi les maîtres skieurs et grimpeurs Marc C. et Marc D., qu'ont toujours essayé de me touer à la montée (merci les gars, vous y avez presque réussi!), Francesco C. (che non sono io ma il "Vecio" del primo piano), et Pierre, Antoine, Grosso, Tobi, Milans, Raph H., Desh, Stef. Varricchio..c'était un grand plaisir de courir (et picoler) avec vous tous.

A géant merci aux tecni-mécaniciens du labo sans lesquelles mes expériences n'auraient jamais pu marcher (ou si elles ont pas marché, même pas commencer) : Jacques (aussi pour les spécialites cuisinées, merci!), Flavio et Pierre Alain. Et merci aux jeunes qui m'ont aidé à fond les jours, les nuits, les week-ends sans jamais hésiter : Varun, Fred e Ivan Bevilaqua (grazie davvero vecchia spugna)..

Le dernier remerciement en français est pour la maman du labo, Marie-Jo, qui a toujours su répondre à toutes nos questions et nous résoudre beaucoup des problèmes.

Out of the EPFL world, a big thank is mandatory to Michael, Matthieu and Ming Yan, who bravely shared the flat with me.

Ma il più grande grazie di cuore va a coloro che hanno davvero permesso di raggiungere questo traguardo, avendo sempre creduto in me: i miei genitori, meglio noti come i Boss (qui tutti vi conoscono così), presenza silenziosa ma sempre viva nonostante la distanza, e tutto il resto della mia famiglia (specie mio fratello con Edo e Lori, mia nonna che chiama sempre alle 7 30 del mattino e gli zii e i cuginetti sparsi per l'Italia).

E dopo tutto questo cammino, che sembra essere passato in un attimo, nonostante non sarà mai abbastanza un grazie ve lo meritate pure voi che avete condiviso con me mille avventure qui e in giro per il mondo (facendomi perdere non pochi capelli): Poolletto e Ele, T(L,J,I..??)ungo e Dani (+2), Ila e Till (i primi conosciuti a Losanna), Mino Mauri Piera, Deb. Branda e tutti gli altri giù a Torino, gli amici di Riccia e di Roma (Bozz e Deb., G., Perri, Pasqualone, ZioNik, U Marinaje, Nik Santo, Vane, Coromà, le VPG, Capozio, Albè, Buba, Isa, Cri, le bagnine del Bosco, e tanti altri), Biasiù, Maska e (La) Robi (scusate fatico ancora a mettere l'articolo davanti al nome), Capitan Pisano, Il Maresciallo (Aaaattenti!) e Silvia, Ale, Carina, Giulio, Creatura, Kenza e Lore, Spillo e Marti, Milans e Silvia, (La) Vale (vedi Robi) e Matassi, Cesca, Iurgo, Fede, Carla e Messi, Seb. e Bilge, Lore Gorla, Giulia, Silvia, ragazzi/e del CRET, Koko e altri sparsi per l'EPFL con cui ho condiviso momenti importanti, arricchito il mio bagaglio di esperienze o bevuto svariate birre..e con questo direi che è tutto.

Ah, prima che mi dimentichi..

..GRAZIE Marta..questa pagina è tutta per te.

*Lausanne, 24 Septembre 2013*

F. C.

## Acknowledgements

---



## Riassunto

L'umidità del suolo è fondamentale per il ciclo dell'acqua in quanto influenza l'infiltrazione, il run-off e le interazioni suolo-atmosfera. In suoli secchi il ruolo dei flussi di vapore diventa cruciale e genera uno stretto legame tra i movimenti di umidità nel suolo e il trasferimento di calore che complica la possibilità di misurare e modellizzare. Essendo necessari progressi sia sulla teoria che sulle tecniche sperimentali, ci siamo concentrati su entrambi: abbiamo realizzato studi teorico-numeriche delle dinamiche di umidità del suolo e energia alla superficie del suolo; testato nuove tecniche di misura, in laboratorio come sul campo, con l'intento di fornire nuove informazioni sulle dinamiche di umidità del suolo e contribuire alla formulazione di una teoria generale sul trasporto accoppiato di energia e umidità.

Poichè le dinamiche di molti sistemi fisici sono descritte da equazioni di conservazione, è pratica comune stimare quantità che non possono essere misurate direttamente (ad esempio i flussi di vapore) dai residui delle equazioni di conservazione. In laboratorio così come in esperimenti sul campo, i residui sono calcolati da misure discontinue in tempo e spazio. Abbiamo teoricamente e numericamente mostrato come l'utilizzo di misure discrete possa portare a grandi residui anche in assenza di errori di misura e modello. Abbiamo dimostrato che i residui sono molto sensibili alla distanza tra le misure e che crescono in presenza di processi non-lineari, come il trasporto di umidità nel suolo. Un'accurata analisi dell'errore è necessaria per poter stabilire l'affidabilità dei residui calcolati da dati discreti ed evitare errate interpretazioni dei processi fisici investigati.

Un altro elemento cruciale nel regolare le dinamiche di umidità nel suolo e l'evaporazione nell'atmosfera è la ritenzione di acqua nel suolo. I modelli parametrici più comuni di curve di ritenzione di ritenzione presentano un potenziale di ritenzione che diventa infinito a saturazione residua, che rappresenta il contenuto idrico del suolo sotto cui il flusso di liquido si arresta. Poche estensioni delle curve di ritenzione sono state proposte, e vengono utilizzate di rado in pratica. Noi abbiamo studiato gli effetti di modelli diversi sul trasporto di acqua liquida e vapore. Abbiamo mostrato che le parametrizzazioni che permettono flussi di vapore sotto saturazione residua predicono flussi di vapore più grandi che generano una superficie del suolo più asciutta mentre il suolo in profondità resta più bagnato. Quando il forcing giornaliero è introdotto, l'evaporazione potenziale è ridotta durante il regime limitato dall'energia e aumentata durante quello limitato dall'umidità. Abbiamo stabilito che in questo caso i

modelli estesi di ritenzione di acqua nel suolo predicono flussi calore maggiori che potrebbero avere importanti effetti su modelli ad ogni scala (anche in modelli di circolazione globale).

La discriminazione tra descrizioni teoriche diverse e modelli parametrici richiede esperimenti che monitorino le dinamiche di energia e umidità nel suolo. Questo necessita dell'utilizzo di sensori accurati e tecniche di misura in grado di monitorare simultaneamente diverse quantità (ad esempio umidità nel suolo, temperatura, proprietà termiche del suolo, concentrazione di soluto nell'acqua del suolo). poichè in generale vengono utilizzati diversi sensori, emergono problemi dovuti alle diverse risoluzioni spazio-temporali e ai differenti volumi di suolo campionati. I sensori multi-funzione a impulso di calore (MFHPPs) sono stati concepiti per superare questi problemi permettendo una misura simultanea di tutte le variabili necessarie. Abbiamo stabilito l'abilità dei MFHPPs nel misurare il flusso di calore nel suolo, che deve essere conosciuto accuratamente per evitare importanti scompensi nel bilancio energetico alla superficie del suolo. Abbiamo usato un setup sperimentale in grado di generare un campo di flusso di calore non uniforme e abbiamo dimostrato che gli MFHPPs possono misurare fedelmente intensità e direzione dei flussi. Questo permette di ottenere un'informazione molto più completa rispetto ai sensori classici (ad esempio i dischi per flusso di calore nel suolo).

Per monitorare lo stato del suolo a grande scala abbiamo investigato la possibilità di ottenere profili distribuiti di conducibilità termica e umidità nel suolo lungo un cavo di fibra ottica. L'informazione è ottenuta monitorando la risposta termica del suolo a un impulso di calore attivamente generato dall'armatura in metallo che protegge il cavo ottico, e analizzando le differenze di temperatura durante la fase di raffreddamento, controllate ogni metro da un sistema distribuito sensibile alla temperatura (DTS). Abbiamo mostrato che l'umidità nel suolo ottenuta dalla risposta termica del suolo (registrata dal DTS) è in buon accordo con misure indipendenti in regimi di suolo bagnato e mediamente bagnato; tuttavia in suoli più secchi il contenuto idrico nel suolo è sottostimato e ulteriori tests sono necessari per poter migliorare la tecnica in condizioni di suolo secco.

In questa tesi abbiamo migliorato in maniera significativa la conoscenza del trasporto accoppiato di energia e umidità nel suolo sia teorico-numericamente che sperimentalmente. Abbiamo dimostrato come misure affidabili possano essere ottenute a diverse scale spazio-temporali, e fornito metodi prognostici e diagnostici per ottimizzarne l'uso. Infine, abbiamo suggerito miglioramenti fondamentali ai modelli numerici che potrebbero avere effetti non solo sulle dinamiche legate al suolo.

**Parole chiave:** Fibre Ottiche Scaldate Attivamente - Flusso di calore nel suolo - Flusso di vapore - Ritenzione di acqua nel suolo - Saturazione residua - Sensing di Temperatura Distribuito Attivo - Sensori multi funzione a impulso di calore - Trasporto di calore - Trasporto di umidità - Umidità del suolo.

# Résumé

L'humidité du sol est essentielle pour le cycle de l'eau car elle affecte l'infiltration, le ruissellement et les interactions sol-atmosphère. Dans les sols secs, les flux de vapeur d'eau ont un rôle essentiel car ils créent un couplage étroit entre la dynamique de l'humidité du sol et le transfert de chaleur, ce qui rend les mesures et la modélisation extrêmement difficiles. Comme des progrès sont nécessaires aussi bien en théorie que pour les méthodes expérimentales, nous nous sommes concentrés sur ces deux aspects. Nous avons effectué des études théoriques et numériques de l'humidité des sols et des dynamiques énergétiques à la surface de la terre. Ensuite, nous avons testé de nouvelles techniques de mesure, en laboratoire et à l'échelle du terrain. Tout cela contribue à fournir de nouvelles perspectives sur la dynamique de l'humidité des sols et à développer une théorie globale du transport couplé d'énergie et humidité.

Comme les dynamiques des systèmes physiques sont dictées par des équations de conservation, il est courant d'estimer les quantités qui ne peuvent être mesurées directement (par exemple les flux de vapeur) à partir des résidus des équations de bilan. En laboratoire, ainsi que lors des expériences sur le terrain, les résidus sont calculés à partir de mesures qui sont discrètes dans l'espace et dans le temps. Nous avons montré théoriquement et numériquement comment l'utilisation des données discrètes peut conduire à de grands résidus, même sans erreurs des mesures ou du modèle. Nous avons démontré que les résidus sont très sensibles à la distance entre les mesures et qu'ils augmentent en présence de processus non linéaires, tels que le transport de l'humidité. Une analyse d'erreur attentive est nécessaire pour évaluer la fiabilité des résidus calculés à partir de données discrètes et éviter des interprétations erronées des processus physiques sous-jacents.

Un autre élément crucial pour dicter les dynamiques de l'humidité du sol et de l'évaporation dans l'atmosphère est la rétention d'eau. Les modèles paramétriques usuels de courbes de rétention présentent un potentiel matriciel qui devient infinie à saturation résiduelle, i.e. lorsque la teneur en eau est inférieure à celle pour laquelle le flux de liquide s'arrête. Quelques extensions des courbes de rétention d'eau ont été proposées, mais elles restent rarement utilisées en pratique. Nous avons étudié les effets de différents modèles de transport de liquide et de vapeur et montré que des paramétrages qui permettent le flux de vapeur au niveau de la saturation résiduelle donnent de plus grands flux de vapeur. Cela se traduit par une surface du sol plus sèche, tandis que le sol profond reste relativement humide. Quand le

forçage journalier est pris en compte, l'évaporation potentielle est réduite durant le régime limité par l'énergie et augmentée durant le régime limité par l'humidité. Nous avons établi que dans ce cas les modèles étendus de rétention d'eau prédisent des flux de chaleur plus grands qui pourraient avoir une incidence critique sur les modèles à grande échelle (compris éventuellement les modèles de circulation globale).

La discrimination entre les différentes descriptions théoriques et les modèles paramétriques demande des données expérimentales des dynamiques d'humidité et d'énergie. Cela requiert l'utilisation de capteurs précis et de techniques de mesure qui sont aptes à surveiller simultanément plusieurs quantités (par exemple, l'humidité, la température, les propriétés thermiques du sol, la concentration du soluté dans l'eau du sol). Comme différentes sondes sont généralement utilisées, des problèmes surgissent en raison des différentes empreintes et des volumes de sols échantillonnés. Des sondes multifonctionnelles à impulsions de chaleur (MFHPPs) ont été conçues pour surmonter ces problèmes en permettant la mesure simultanée de toutes les variables requises. Nous avons évalué la capacité des MFHPPs à mesurer le flux de chaleur du sol, qui doit être connue avec précision pour éviter des déséquilibres significatifs dans le bilan énergétique de surface. Pour cela, nous avons utilisé un dispositif expérimental capable de générer un champ de flux thermique non uniforme et nous avons démontré que les MFHPPs peuvent capturer de manière fiable les grandeurs et les directions des flux. Cela permet une information plus complète sur les flux de chaleur du sol que celle obtenue par les sondes classiques (par exemple des disques mesurant le flux de chaleur du sol).

Pour contrôler l'état du sol sur les terrains à grande échelle, nous avons étudié la possibilité de déduire la conductivité thermique distribuée et les profils d'humidité du sol avec une fibre optique. L'information est obtenue en mesurant la réponse du sol à une impulsion de chaleur active générée au long du bouclier métallique du câble optique, et en analysant les différences de température lors de la phase de refroidissement. La température est contrôlée mètre par mètre grâce à un système de détection de température distribuée (DTS). Nous avons montré que les mesures d'humidité du sol présumées des réponses thermiques du sol (enregistré par le DTS) sont en bon accord avec des mesures indépendantes dans les sols humides et presque humide, mais dans les sols secs la teneur en eau est sous-estimé. D'autres investigations sont nécessaires pour améliorer cette technique pour conditions sèches.

Dans cette étude, nous avons considérablement amélioré la connaissance du transport couplé d'énergie et d'humidité sur les plans théorique, numérique et expérimentale. Nous avons prouvé que des mesures fiables peuvent être obtenues à différentes échelles spatio-temporelles, et nous avons développé des méthodes pronostic et diagnostic afin d'optimiser leur utilisation. Enfin, nous avons proposé des améliorations cruciales pour les modèles numériques qui pourraient avoir des implications au-delà des dynamiques des sols du terrain.

**Mots clés :** Evaporation - Fibres optiques chauffées - Flux de chaleur - Rétention d'eau du sol - Saturation résiduelle - Sondes multifonctionnelles à impulsions de chaleur - Teneur en eau.

# Abstract

Soil moisture is crucial to water-cycle as it affects infiltration, runoff and land-atmosphere interactions. In dry soils the role of water vapor fluxes becomes essential and causes a tight coupling between soil moisture dynamics and heat transfer, which makes measurements and modeling extremely difficult. Since advances in both theory and experimental techniques are required, we have focused on both aspects: we have performed theoretical-numerical investigations of soil moisture and energy dynamics at the land surface; tested novel measurements techniques, in laboratory and at field scale, to provide new insights into soil moisture dynamics and contribute to a comprehensive theory of coupled energy and moisture transport.

As the dynamics of physical systems are dictated by conservation equations, it is common practice to estimate quantities that cannot be directly measured (e.g. vapor fluxes) from the residuals of balance equations. In laboratory as well as in field experiments, residuals are calculated from measurements that are sparse in space and discrete in time. We have theoretically and numerically shown how the use of discrete data may lead to large residuals even without measurements or model errors. We have demonstrated that residuals are very sensitive to the distance between the measurements and that they increase in presence of nonlinear processes, such as moisture transport. A careful error analysis is required to assess the reliability of residuals computed from discrete data and avoid misinterpretations of the underlying physical processes.

Another crucial element dictating soil moisture dynamics and evaporation into the atmosphere is soil water-retention. Popular parametric models of the retention curve present a matric potential that becomes infinite at residual saturation, which is the water content below which liquid flow stops. Few extensions of the water-retention curves have been proposed, which remain rarely used in practice. We have studied the effects of different models on liquid and vapor transport. We have shown that parameterizations that allow vapor flux below residual saturation yield larger vapor fluxes that result in a drier soil surface, whereas deep soil remains relatively wet. When diurnal forcing is considered, potential evaporation is reduced in the energy-limited regime and enhanced in the moisture-limited regime. We have established that in this case extended water-retention models predict larger heat fluxes that might critically impact models at whole scales (possibly including global circulation models).

## Abstract

---

Discrimination between different theoretical descriptions and parametric models requires experiments that monitor moisture and energy dynamics. This demands the use of accurate sensors and measurement techniques that are able to simultaneously monitor several quantities (e.g. soil moisture, temperature, soil thermal properties, solute concentration in soil water). As in general different probes are used, problems arise due to different footprints and sampled soil volumes. Multi functional heat pulse probes (MFHPPs) have been conceived to overcome these issues by allowing simultaneous measurements of all required variables. We have assessed MFHPPs ability to measure ground heat flux, which has to be accurately known to avoid significant imbalances in the surface energy budget. We have employed an experimental setup able to generate a non-uniform heat-flux field and we have demonstrated that MFHPPs can reliably capture the magnitudes and directions of the fluxes. This allows more complete information on ground heat flux than that obtained by the classic probes (e.g. ground heat flux plates).

To monitor soil state in large-scale field applications we have investigated the possibility to infer distributed thermal conductivity and soil moisture profiles with an optical fiber. Information is obtained by monitoring soil response to an active heat pulse generated from the metal shield armoring the optic cable, and analyzing the temperature differences of the cooling phase, monitored each meter by a distributed temperature sensing system (DTS). We have shown that soil moisture measurements inferred from soil thermal response (recorded by the DTS) are in good agreement with independent measurements in wet and intermediately wet soils; however in dry soils moisture content is underestimated and further investigations are required to improve this technique for dry conditions.

In this study we have significantly improved the knowledge of coupled energy and moisture transport on both theoretical-numerical and experimental sides. We have proven that reliable measurements can be obtained at different spatiotemporal scales, and provided both prognostic and diagnostic methods to optimize their use. Finally, we have suggested crucial improvements to numerical models which might have implications beyond field-soils dynamics.

**Keywords:** Active Distribute Temperature Sensing - Actively Heated Fiber Optics - Ground heat flux - Heat transport - Moisture transport - Multi functional heat pulse probes - Residual saturation - Soil moisture - Soil water retention - Vapor flux.

# Contents

<b>Acknowledgements</b>	<b>v</b>
<b>Riassunto</b>	<b>ix</b>
<b>Résumé</b>	<b>xi</b>
<b>Abstract</b>	<b>xiii</b>
<b>1 Introduction</b>	<b>1</b>
1.1 The PdV Theory . . . . .	2
1.2 The Mismatch Theory-Experiment: Enhancement Mechanisms and Alternative Hypothesis . . . . .	5
1.3 The Midday Moisture Content Rise . . . . .	7
1.4 Research Questions and Thesis Organization . . . . .	8
<b>2 Error Induced by Discrete Flux Calculation</b>	<b>15</b>
2.1 Introduction . . . . .	15
2.2 Analysis Performed . . . . .	16
2.3 Results . . . . .	17
2.3.1 Cumulative Residual . . . . .	19
2.4 Conclusions . . . . .	19
<b>3 Retention Curves and Evaporation Part I: the Isothermal Case</b>	<b>25</b>
3.1 Introduction . . . . .	26
3.2 Water-retention curve and vapor density . . . . .	26
3.3 Modified retention models . . . . .	27
3.4 Isothermal evaporation from soil columns . . . . .	29
3.5 Results and discussion . . . . .	30
3.6 Conclusions . . . . .	32
<b>4 Retention Curves and Evaporation Part II: the Diurnal Atmospheric Forcing</b>	<b>39</b>
4.1 Introduction . . . . .	40
4.2 Transport equations . . . . .	40
4.2.1 Liquid and vapor transport equation . . . . .	41
4.2.2 Heat transport equation . . . . .	42
	xv

## Contents

---

4.3	Water-retention curves and unsaturated hydraulic conductivity . . . . .	42
4.4	Evaporation from soil columns with diurnal forcing . . . . .	43
4.5	Results and discussion . . . . .	45
4.A	Appendixes: Parameterizations . . . . .	48
4.A.1	Hydraulic Parameters . . . . .	48
4.A.2	Thermal Parameters . . . . .	49
4.A.3	Atmospheric forcing parameterizations . . . . .	50
<b>5</b>	<b>Multi Functional Heat Pulse Probes for Planar Heat Flux Measurements: a Laboratory Experiment</b>	<b>55</b>
5.1	Introduction . . . . .	56
5.2	MFHPP Theory . . . . .	57
5.3	Experimental Set-up and Measurements . . . . .	59
5.4	Analysis . . . . .	61
5.5	Results and Discussion . . . . .	62
<b>6</b>	<b>Heated Optical Fiber for Distributed Soil-Moisture Measurements: A Lysimeter Experiment</b>	<b>71</b>
<b>7</b>	<b>Conclusions and Future Work</b>	<b>83</b>
<b>A</b>	<b>Other Author's Contribution</b>	<b>87</b>
	<b>Curriculum Vitae</b>	<b>99</b>



# 1 Introduction

"What is soil moisture?"

*"Soil moisture is difficult to define because it means different things in different disciplines. [...] Generally, however, soil moisture is the water that is held in the spaces between soil particles."*

"Why is measuring soil moisture important?"

*"Soil moisture is a key variable in controlling the exchange of water and heat energy between the land surface and the atmosphere through evaporation and plant transpiration... [...] soil moisture plays an important role in the development of weather patterns and the production of precipitation. [...] Soil moisture information is valuable to a wide range of government agencies and private companies concerned with weather and climate, runoff potential and flood control, soil erosion and slope failure, reservoir management, geotechnical engineering, and water quality"*

From <http://wwwghcc.msfc.nasa.gov/landprocess/>, [December 1999].

In these few lines NASA scientists highlight three fundamental concepts:

1. the tight link between soil moisture movement and energy transfer, mainly occurring through evaporation.
2. the role played by soil moisture in the water cycle, by affecting the land-atmosphere interactions (see Fig. 1.1).
3. the need in many fields of accurate monitoring and modeling of soil moisture dynamics, from local to global scale.

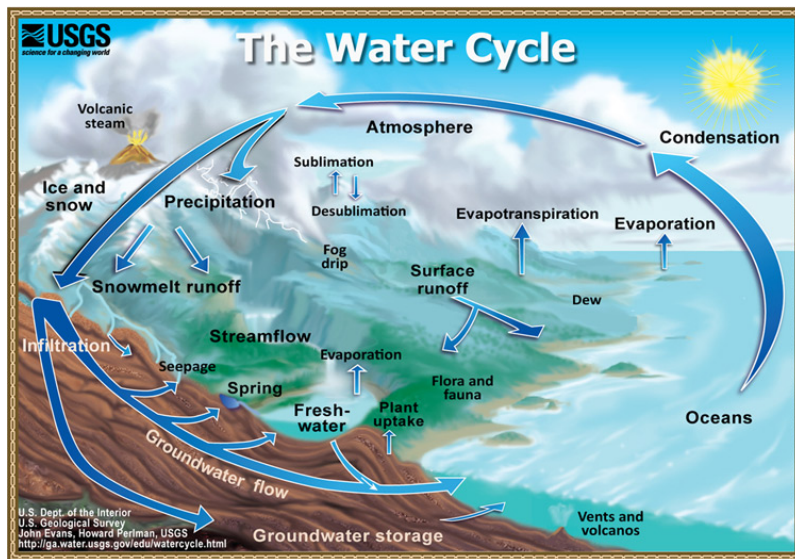


Figure 1.1: The water cycle: Evapotranspiration (evaporation from water bodies or soil surface and transpiration from plant stomata) represent almost the total moisture mass flux from the earth surface back into the atmosphere (sublimation representing a small fraction) and about 80% of the energy flux in form of latent heat [Brutsaert, 2005]. Picture obtained from USGS website.

None of this concepts is of recent discovery. However, although almost one century has already passed since the coupling between the movement of moisture and temperature in the soil has been recognized [Bouyoucos, 1915], and more than 60 years since Philip and de Vries [1957] and de Vries [1958] have proposed the first mathematical description of the coupled heat and mass transfer in soils (henceforth PdV theory, see Sec. 1.1), some discrepancies between theory and experiments (especially noticed in field applications, see Sec. 1.2 and Sec. 1.3) suggest that an exhaustive understanding and description of the mechanisms involved has not been yet reached.

This is mainly due to the challenges of modeling vapor flux at the land-surface interface, particularly in dry-media, and to the difficulties in obtaining accurate field measurements to validate the models. Both these topics represent the focus of the dissertation.

## 1.1 The PdV Theory

After Bouyoucos [1915], it was known that the total heat flux is not only driven by pure conduction but also by moving water in both liquid and vapor phase (mainly related to latent heat transport), and that temperature gradients can drive mass transfer through their influence on the unsaturated flow parameters.

Decades later, during laboratory experiments several investigators (i.e. Gurr et al. [1952];

*Rollins et al.* [1954]; *Taylor and Cavazza* [1952]) notice that:

- the observed water vapor transport under thermal gradients greatly exceeds the prediction by the simple theory of vapor diffusion, which does not account for any temperature effect;
- the observed moisture transfer under temperature gradients is negligibly small both in very dry and in very wet media, but attains a fairly well-defined maximum at an intermediate moisture content which appears to depend both on soil matric potential and on the air-filled porespace. The maximum in vapor transport predicted by the simple theory of vapor diffusion is generally at too low moisture content to agree with observations.

In the attempt to reconcile theory with experiments and observations, *Philip and de Vries* [1957] develop a mathematical description of the physical mechanisms relevant to vapor and liquid water transport in soils, mutually influenced by heat transfer. *de Vries* [1958] corrects some problems of the first formulation (especially in the heat transfer description), and relaxes some constraints, but since he basically preserves the main structure of *Philip and de Vries* [1957] as PdV theory here and henceforth is intended the *de Vries* [1958] formulation.

PdV assume a purely diffusive vapor flux based on Fick's law, which is written in the form

$$\mathbf{j}_v = -D_v \nabla \rho_v, \quad (1.1)$$

where  $D_v$  is the water-vapor molecular diffusivity in the unsaturated porous medium and  $\rho_v$  is the vapor density; and a Darcian liquid flux, i.e.,

$$\mathbf{j}_l = -\rho_l K \nabla \Psi, \quad (1.2)$$

where the total potential  $\Psi = \psi + z$  includes the matric potential (since vapor advection is neglected, the vapor potential is constant and the water pressure is identical to the capillary pressure) and the gravity potential and  $K$  is the unsaturated hydraulic conductivity. They choose the temperature  $T$  and the volumetric liquid moisture content  $\theta_l$  as independent variables (i.e.  $\psi = \psi(T, \theta_l)$ ) and assume local equilibrium between liquid and vapor phase through the Kelvin equation (here in the exponential form by *Edlefsen and Anderson* [1943]):

$$\rho_v = \rho_v^* h = \rho_v^*(T) \exp(\psi g / RT) \quad (1.3)$$

where  $h$  is the relative humidity of water vapor,  $\rho_v^*$  the saturated vapor density of bulk water,  $R$  is the gas constant for water vapor and  $g$  the gravity constant. PdV write a total soil moisture balance equation of the form

$$\rho_l \frac{\partial(\theta_l + \theta_v)}{\partial t} = -\nabla \cdot (\mathbf{j}_l + \mathbf{j}_v) = \rho_l \nabla \cdot (D_T \nabla T + D_\theta \nabla \theta_l + K \hat{z}), \quad (1.4)$$

where the liquid is assumed incompressible and  $\theta_v = (\phi - \theta_l) \rho_v / \rho_l$  represents the volumetric vapor content of precipitable water.

## Chapter 1. Introduction

---

The thermal diffusivity

$$D_T = D_{T,l} + D_{T,v} = K \frac{\partial \psi}{\partial T} + \eta D_v h \frac{1}{\rho_l} \frac{d\rho_v^*}{dT}, \quad (1.5)$$

and the isothermal diffusivity

$$D_\theta = D_{\theta,l} + D_{\theta,v} = K \frac{\partial \psi}{\partial \theta_l} + D_v \frac{g\rho_v}{\rho_l RT} \frac{\partial \psi}{\partial \theta_l}. \quad (1.6)$$

which relate the mass flux to the gradients of  $T$  and  $\theta_l$ , respectively. Both diffusivities include liquid and vapor contributions, indicated by the subscripts  $l$  and  $v$ , respectively. PdV assume that the matric potential varies with the temperature only due to change in the surface tension  $\sigma$ ,  $\frac{\partial \psi}{\partial T} = \frac{\psi}{\sigma} \frac{d\sigma}{dT}$  and the hypothesis that the relative humidity is independent of the temperature,  $\frac{\partial h}{\partial T} = 0$  or  $\frac{\partial \psi}{\partial T} - \frac{\psi}{T} = 0$ , is relaxed.

In Eq. 1.5, PdV introduce a mechanistic enhancement factor  $\eta$

$$\eta = \begin{cases} \frac{\phi}{\tau(\phi - \theta_l)} \frac{(\nabla T)_a}{\nabla T} & \text{if } \theta_l < \theta_{l,cont} \\ \frac{\phi + (\theta_l - \theta_{l,cont})}{\tau(\phi - \theta_{l,cont})} \frac{(\nabla T)_a}{\nabla T} & \text{if } \theta_l > \theta_{l,cont} \end{cases} \quad (1.7)$$

to account for transfer through liquid islands during vapor transfer and for larger temperature gradients in the air filled pores  $(\nabla T)_a$ ;  $\theta_{l,cont}$  is the threshold below which liquid continuity fails, while  $\phi$  and  $\tau$  are the medium porosity and a-dimensional tortuosity factor for vapor diffusion, respectively. The role of  $\eta$  is discussed in Sec. 1.2.

They describe the heat transport by a conservation equation in the form

$$\frac{\partial}{\partial t} (CT + L\rho_l\theta_v + c_l\rho_l(T - T_0)(\theta_l + \theta_v) + \rho_l W\theta_l) = -\nabla \cdot \mathbf{j}_h = \nabla \cdot (-\lambda \nabla T + L\mathbf{j}_v + c_l(T - T_0)(\mathbf{j}_l + \mathbf{j}_v)) \quad (1.8)$$

where  $C$  indicates the volumetric soil heat capacity (for solid, liquid and gas phase),  $L$  the latent heat of vaporization,  $c_l$  the specific heat of liquid water,  $\mathbf{j}_h$  the heat flux and  $\lambda$  the thermal conductivity of the soil.

The heat storage (l.h.s of Eq. 1.8) accounts not only for the soil heat capacity (first term), but also for the volumetric release of latent heat due to evaporation at temperature  $T$  (second term), for the accumulation of sensible heat in both liquid and vapor phase with respect to a reference temperature  $T_0$  (third term) and for the differential heat of wetting  $W$ , defined as the amount of heat released per unit mass of added water when an infinitesimal quantity of free liquid water is added to the medium. Based on *Edlefsen and Anderson* [1943] PdV assume  $W = RT^2 \frac{\partial \ln h}{\partial T} = \frac{RT^2}{h} \frac{\partial h}{\partial T} = -g(\psi - T \frac{\partial \psi}{\partial T})$ .

On the r.h.s, they define the heat flux  $\mathbf{j}_h$  as the sum of the heat conduction (first term), the advection of latent heat by vapor flux (second term) and the advection of sensible heat by total moisture flux (third term).

## 1.2 The Mismatch Theory-Experiment: Enhancement Mechanisms and Alternative Hypothesis

PdV postulate the existence of an enhancement mechanism for the thermally driven water vapor flux because the additional diffusion (for both liquid and vapor phase) provided by  $T$  gradients (i.e. Eq. 1.5, without accounting for  $\eta$ ) is not big enough to explain the experimental observations reported in Sec. 1.1. They assume that at pore scale vapor diffusion is enhanced both by local condensation and evaporation occurring around isolated liquid islands within the porous medium and by local temperature gradients ( $\nabla T_a$  in Eq. 1.7) in the vapor phase larger than the average macroscopic temperature gradient  $\nabla T$  in the porous medium.

Including  $\eta$ ,  $D_{T,v}$  enhances by a factor ten in some cases which improves the comparison with experiments.

Enhancements mechanisms of vapor diffusion are deeply investigated and debated, and the estimate of the real vapor contribution in moving both energy and mass becomes the objective of many numerical, theoretical and experimental studies.

*Jury and Letey* [1979] and *Cass et al.* [1984] consider wrong estimates of  $\eta$  a major issue in PdV theory and propose an empirical relation for the water vapor enhancement factor. However, this does not yield a satisfactory agreement with field data (e.g. *deVries* [1987]).

*Rose* [1968a,b] and Jackson and coworkers [*Jackson*, 1973; *Jackson et al.*, 1974] perform significant field-scale tests to define the role of thermally driven vapor fluxes under different surface forcing conditions provided by diurnal cycles. They combine temperature and soil moisture measurements at different depths in the upper 15 cm soil layer. In both cases gravimetric observations collected around 1 cm depth show a diurnal trend of  $\theta_l$  which is anti-correlated with soil temperature and characterized by a decrease at daytime (soon after sunrise until sunset, usually with a minimum after the air temperature peak is reached) and a stabilization or a rise at nighttime due to capillary redistribution and vapor condensation (Fig. 1.3,a,b). At deeper layers, instead,  $\theta_l$  diurnal oscillations are sensibly damped and in some cases an atypical behavior of  $\theta_l$  which rises around midday is clearly observed (Fig. 1.3,a,b). This particular effect, also noticed by other investigators (e.g. *Cahill and Parlange* [1998]; *Verhoef et al.* [2006]), is discussed in detail in Sec. 1.3.

They both solve the mass balance with the thermal vapor as unknown, and they find that while the liquid flux is mainly oriented upward, the thermal vapor oscillates following the temperature trend and enhances the diurnal increase (night)/decrease (day) of  $\theta_l$ . They conclude that the amount of vapor water transported through a shallow soil is of the same magnitude as the fluctuations of volumetric moisture content.

*Westcot and Wierenga* [1974], combining field experiments and a numerical model calculate from the energy balance that the heat transported by vapor flux is on the same order as heat flux by conduction and accounts for 40-60% of total heat flux in the top 2 cm of soil. *Ho and Webb* [1998] assert that there is no direct experimental evidence for enhanced vapor transport mechanisms, even though they admit the possibility of such mechanisms to exist, demonstrating theoretically that the vapor mass transfer through the liquid islands is one order of magnitude bigger than the standard Fickian diffusion around the liquid islands.

*Cahill and Parlange* [1998] compare the water vapor flux calculated from both the energy and moisture balance equations, finding reasonable agreement and a contribution for vapor transport to heat flux comparable to *Westcot and Wierenga* [1974], whereas a smaller (but still significant) vapor contribution to the total moisture flux (10-30%) is calculated. They show how the same vapor fluxes calculated using PdV theory instead than energy/mass balance equations are sensibly smaller (Fig. 1.2), concluding that PdV theory is incomplete with respect to the description of vapor transport. *Parlange et al.* [1998] suggest that the contraction/ex-

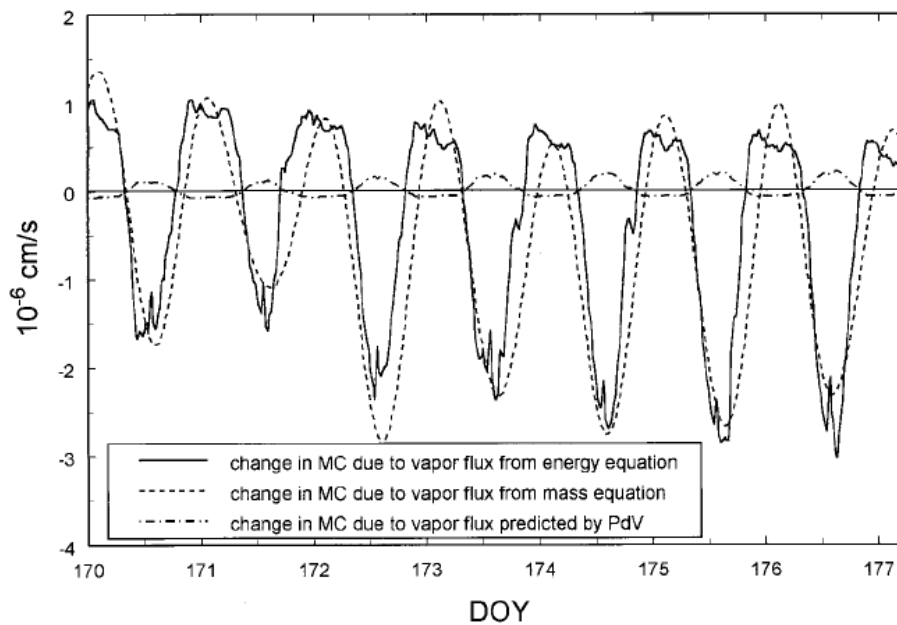


Figure 1.2: Comparison of the changes in the moisture content (MC) in the 7- to 10-cm soil layer due to vapor transport calculated from the energy equation (Eq. 1.8) and the moisture equation (Eq. 1.4). Positive values indicate a net transport of vapor to the soil layer; negative values indicate that more vapor is leaving the layer than entering. Also shown is the vapor flux through this layer calculated with the Philip and de Vries [1957] expressions for the vapor diffusion coefficients  $D_{T,v}$  and  $D_{\theta,v}$ . Figure from *Cahill and Parlange* [1998].

pansion of air near the soil surface under the diurnal cooling/heating could transport water vapor by convection and fix the discrepancy between the theory and their measurements (Sec. 1.3). *Milly* [1982] converts the PdV formulation (including the enhancement factor) to one that employs the matric potential  $\psi$  and  $T$  as main variables. This allows to incorporate hysteresis and soil heterogeneity into the theory. Following *Kay and Groenevelt* [1974] he also includes the effects of adsorbed liquid flow due to temperature gradients. His simulations show that isothermal vapor diffusion is more important than thermal vapor diffusion which can contribute by only 5-15% to daily average evaporation in dry conditions, and even less important in moister cases (*Milly* [1984]). *Nassar and Horton* [1989, 1992a] modify PdV theory to include osmotic pressure effects due to the presence of non-volatile solute in the soil water.

Although they manage to predict in a reasonable manner the temperature and liquid moisture content profile generated in laboratory in 10 cm-long soil columns under nonisothermal wet conditions, predictions of soil moisture content exceeds measured values when the soil dries. *Griffoll et al.* [2005] numerically the role of the advective vapor flux by adding a third equation for the air phase to the PdV equations. They note that the dispersion of water vapor can account for up to 35% of total vapor transport, especially in very dry conditions. However, they refer to a very thin soil layer from 0 to 0.5 cm from the surface, and in several case in their study cases the moisture contents are underestimated by about 30%.

*Lehmann et al.* [2008]; *Shokri et al.* [2008b]; *Shokri et al.* [2009] investigate experimentally and theoretically the effects of capillary-induced liquid flow through unsaturated zone during evaporation, never properly considered in the previous citations, in which liquid discontinuity (with the consequent formation of liquid islands responsible of the enhancing mechanisms) is assumed. They conclude that there is no need for postulating unobservable local thermal gradients or any other enhancing mechanism for thermal vapor fluxes if the total moisture flux accounts for both Fickian vapor diffusion and capillary flows. Despite the assertions of *Ho and Webb* [1998] and *Shokri et al.* [2009], the existence of enhancements factors for thermally driven vapor flux, although questionable, is commonly accepted and  $\eta$  is widely adopted, even in commercial codes such as Hydrus (see, e.g. *Saito et al.* [2006]).

### 1.3 The Midday Moisture Content Rise

In general, in field tests, at depths between 2-15 cm, the  $\theta_l$  time series show atypical rise positively correlated with soil temperature [see, e.g., *Rose* [1968a]; *Jackson et al.* [1974]; *Monji et al.* [1990]; *Cahill and Parlange* [1998]; *Verhoef et al.* [2006]]. If *Verhoef et al.* [2006]; *Cahill and Parlange* [1998]; *Monji et al.* [1990] measurements are taken with dielectric probes which may be affected by the dependence of the dielectric constant on temperature [*Or and Wraith*, 2000]), the gravimetric observations by *Rose* [1968a]; *Jackson* [1973] which are not affected by any temperature influence, show the same behavior (Fig. 1.3).

*Assouline et al.* [2010] observe this effect during their measurements with time domain reflectometry (TDR, see e.g. *Topp et al.* [1980]) placed at 5-10-15 cm depth in a 25 cm-height sand bucket exposed to strong diurnal cycles for several days. Their analysis excludes temperature influence on the dielectric permittivity as main responsible for the positive correlation between  $\theta_l$  at  $T$ , whereas attributes this fact to a water redistribution due to liquid water fluxes resulting from the temperature-gradient dynamics within the sand profile at those depths.

However, numerical simulations performed using Hydrus 1-D with enhanced heat transport (e.g. *Saito et al.* [2006]), are unable to predict the  $\theta_l$  lowering at nighttime and tend to underestimate the rise at noon.

If few doubts about the physically existence of this phenomenon persist, how model it properly remains an open challenge.

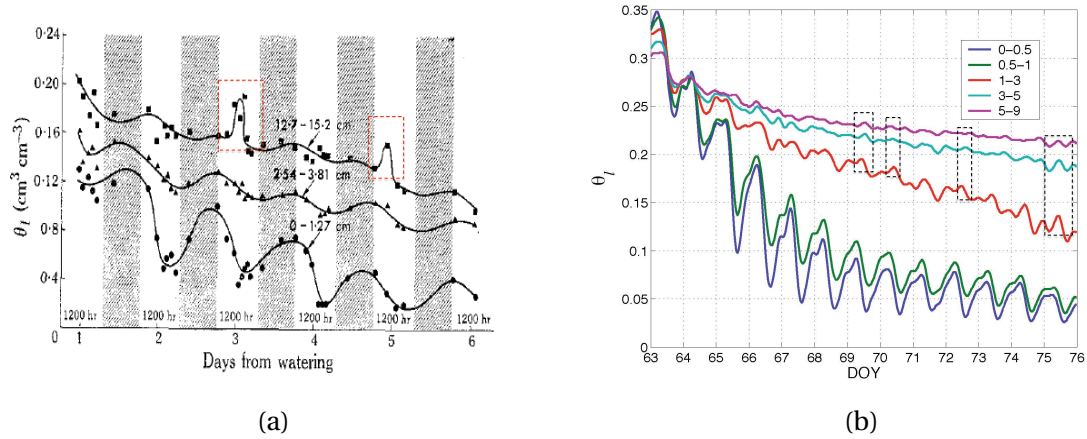


Figure 1.3: Gravimetric  $\theta_l$  time series at different depths [cm] observed by *Rose* [1968a] (a) and *Jackson* [1973] (b). (a) is adapted from *Rose* [1968a], (b) is a plot from *Lunati, I.* (internal report) of observations from 0:00 AM day of the year 63 (DOY) to 0.00 AM DOY 76. Dashed red (a) and black (b) rectangles highlight atypical  $\theta_l$  rises around midday.

## 1.4 Research Questions and Thesis Organization

In previous sections we have described the failure of the efforts to reconcile experimental observations with PdV theory for coupled heat and moisture transfer in soils by including all the investigated modifications, new parametrization, different formulations. This gap is particularly evident in field-studies when the soil, dried by diurnal temperature forcing, reaches low levels of moisture content and vapor dynamics are more important.

The overall objective of the present work is both to advance the knowledge of transport phenomena in soils by testing recently developed local and distributed techniques in laboratory and field; and to improve, by analytical and numerical investigations of the behavior of PdV equations, the theoretical framework for predicting soil-moisture dynamics, with particular attention to the investigation of dry regimes induced by evaporation. We also provide indications about possible misinterpretation of data analysis based on discrete measurements.

In Chap. 2, we investigate the systematic errors induced by mass and energy budgets computed directly from discrete measurements, which is a common approach in many studies. We address the following research questions: (i) What is the error introduced by computing heat and moisture balances by using discrete data, with respect to the analytical/numerical solutions, and when is this error more/less important? (ii) How much is this error sensitive to the different spacing of the discrete measurements? (iii) What are possible solutions to overcome this discretization issue?



## 1.4. Research Questions and Thesis Organization

---

In Chap. 3, we question the use of residual saturation in standard retention models as lower limit for  $\theta_l$ , at which capillary pressure becomes infinite. In isothermal conditions and applying an evaporation at the soil surface dependent on the delta of absolute humidity between the surface and the air above, we numerically compare the effects on liquid and vapor fluxes for two different soils, using as retention curve the standard Van Genuchten *Van Genuchten* [1980] and two "extended" versions, which allow for vapor flow in the zone below the residual saturation. The questions we address are: (i) What are the effects induced on liquid and in particular vapor dynamics by the extension of the retention curves in the below-residual saturation zone, and what are the implications for laboratory to planetary scale? (ii) May these effects help in the reconciliation of theory and experiments and reduce the need for empirical enhancement factors?

In Chap. 4 we follow up the numerical investigations of Chap.3, but we include the effects of the radiative forcing at the soil surface and assign atmosphere dependent boundary conditions based on aerodynamic diffusion relationships. We compare the standard retention curve with the two extended already employed in Chap.4, for a loam, without accounting for any enhancement factor of water vapor. We address the following research questions: (i) Is there an impact of the diurnal forcing on the cumulative evaporation with respect to the steady-forcing case investigated in Chap. 3 (ii) What are the effects induced on liquid and in particular vapor dynamics by the extension of the retention curves in the below-residual saturation zone in presence of diurnal radiative forcing?

In Chap. 5, we present laboratory measurements performed to investigate the ability of multi functional heat pulse probes (MFHPPs) to monitor soil heat flux which is not accurately measured by the commonly adopted probes such as the heat flux plates, despite the fundamental component of the surface energy balance. Taking advantage of the penta-needles structure of the MFHPPs and releasing the common hypothesis of mono-dimensionality of the soil heat flux, not true, we test the MFHPPs by generating 2D heat fluxes in cylindrical symmetry across oven-dried sand. We show a comparison of measured and simulated heat fluxes. The main question we address is: (i) Are the MFHPPs reliable for the measurement of soil heat fluxes which are not vertically aligned?

In Chap. 6 we test the accuracy of the actively heated fiber optics method (AHFO) to provide distributed thermal conductivity and, therefore, soil moisture profiles along a fiber optics cable buried in a large coil in a soil exhibiting different wetting regimes with depth. The AHFO is based on the asymptotic analysis of the thermal response of the soil, monitored by a distributed temperature sensing system (DTS) which is proportional to the amount of water stored, to the distributed heat pulses along the metal shield protecting the buried fiber optics cable. We compare the AHFO measurements with independent soil moisture measurements. The research questions we address are the following: (i) Is the AHFO able to detect thermal conductivity and therefore moisture variations in the soil surrounding the cable? (ii) What

## **Chapter 1. Introduction**

---

is the accuracy of the detection? (iii) May the AHFO become a reliable source of distributed inputs to provide to numerical models?

Finally, Chap. 7 presents an overview of the main findings of this dissertation and give recommendations for future works.

# Bibliography

- Assouline, S., Narkis, K., Tyler, S.W., Lunati, I., Parlange, M.B. and Selker, J.S. On the diurnal soil water content dynamics during evaporation using dielectric methods. *Vadose Zone J.*, 9, 709-718, 2010.
- Bouyoucos, G.T. Effect of temperature on the movement of water vapor and capillary moisture in soils. *J. Agric. Res.*, 5, 141-172, 1915.
- Brutsaert, W.H. Hydrology: an introduction. *Cambridge Univ. Press.*, 605 pages, 2005.
- Cahill, A.T. and Parlange M.B. On water vapor transport in field soils *Water Resour. Res.*, 34(4), 731-739, 1998.
- Cass, A., Campbell, G.S. and Jones, T.L. Enhancement of thermal water-vapor diffusion in soil. *Soil Sci. Soc. Am. J.*, 48(1), 25-32, 1984.
- de Vries, D.A. Simultaneous transfer of heat and moisture in porous media. *Eos Trans. AGU*, 39(5), 909-916, 1958.
- de Vries, D.A. The theory of heat and moisture transfer in porous media revisited. *Int. J. Heat Mass Transfer*, 30(7), 1343-50, 1987.
- Edlefsen, N.E. and Anderson, A.B.C. The thermodynamics of soil moisture *Hilgardia*, 16, 31-299, 1943.
- Grifoll, J., Gasto, L.M. and Cohen, Y. Non isothermal soil water transport and evaporation, *Adv. Water Res.*, 28, 1254-1266, 2005.
- Gurr, C.G., Marshall, T.J. and Hutton, J.T. Movement of water in soil due to a temperature gradient *Soil Sci.*, 74, 335-345, 1952.
- Ho, C.K. and Webb, S.W. Review of porous media enhanced vapor-phase diffusion mechanisms, models, and data—Does enhanced vapor-phase diffusion exist? *J. Porous Media*, 1(1), 71-92, 1998.
- Jackson, R.D. Diurnal changes in soil water content during drying *Field Soil Water Regime, Spec. Publ.*, 5, edited by R. R. Bruce et al., pp 37-55, Soil Sci. Soc. of Am., Madison, Wis., 1973.

## Bibliography

---

- Jackson, R.D., Reginato, R.J., Kimball, B.A. and Nakayama, F.S. Diurnal soil-water evaporation: Comparison of measured and calculated soil-water fluxes *Soil Sci. Soc. Am. J.*, 38, 861-866, 1974.
- Jury, W. A. and Letey, J. Water vapor movement in soil: Reconciliation of theory and experiment *Soil Sci. Soc. Am. J.*, 43(5), 823- 827, 1979.
- Kay, B.D. and Groenevelt, P.H. On the interaction of water and heat in frozen and unfrozen soils, 1, Basic Theory: the vapor phase. *Soil Sci. Soc. Am. J.*, 38(3), 395-400, 1974.
- Lehmann, P., Assouline, S. and Or, D. Characteristic lengths affecting evaporative drying of porous media *Phys. Rev. E*, 77, 056309, doi:10.1103/PhysRevE.77.056309, 2008.
- Milly, P.C.D. Moisture and heat transport in hysteretic, inhomogeneous porous media: a matrix-head based formulation and a numerical model., *Water Resources Research*, 18(3), 489-498,1982.
- Milly, P.C.D. A simulation analysis of thermal effects on evaporation from soil, *Water Resources Research*, 20, 1087-1098,1984.
- Monji, N., Hamotani, K., Omoto, Y. Dynamic behavior of the moisture near the soil-atmosphere boundary, *Bull. Univ. Osaka*, 42, Ser. B, 1990.
- Nassar, I.N. and Horton, R. Water transport in unsaturated nonisothermal salty soil: II. Theoretical development *Soil Sci. Soc. Am. J.*, 53, 1330-1337, 1989.
- Nassar, I.N. and Horton, R. Simultaneous transfer of heat, water, and solute in porous media. I. Theoretical development *Soil Sci. Soc. Am. J.*, 56, 1350-1356, 1992.
- Or, D. and Wraith, J.M. Comment on On water vapor transport in field soils. *Water Resour. Res.*, 36,3103-5, 2000.
- Parlange, M.B., Cahill A.T., Nielsen D.R., Hopmans J.W. and Wendroth, O. Review of heat and water movement in field soils. *Soil Tillage Res*, 47:5-10, 1998.
- Philips, J.R. and de Vries D.A. Moisture movements in porous materials under temperature gradients, *Transaction of American Geophysical Union*, 1957.
- Rollins, R.L., Spangler, M.G. and Kirkham, D. Movement of soil moisture under a thermal gradient *Highway Res. Board Proc.*, 33, 492-508, 1954.
- Rose, C.W. Water transport in soil with a daily temperature wave, I, Theory and experiment. *Aust. J. Soil Res.*, 6, 31-44, 1968a.
- Rose, C.W. Water transport in soil with a daily temperature wave, II. *Aust. J. Soil Res.*, 6, 45-57, 1968b.
- Saito,H., Simunek, J., Mohanty and P. Binayak Numerical analysis of coupled water, vapor, and heat transport in the Vadose zone *Vadose Zone Journal*, 5, 784-800, 2006.

- Shokri, N., Lehmann, P. and Or, D. Effects of hydrophobic layers on evaporation from porous media *Geophys. Res. Lett.*, 35, L19407, 2008b.
- Shokri, N., Lehmann, P. and Or, D. Critical evaluation of enhancement factors for vapor transport through unsaturated porous media *Water Resour. Res.*, 45, W10433, 2009.
- Taylor, S.A. and Cavazza, L. The movement of soil moisture in response temperature gradients. *Soil Sci. Soc. Amer. Proc.* , 18, 351-358, 1954.
- Topp, G.C., Davis, J.L. and Annan, A.P. Electromagnetic determination of soil water content: measurement in coaxial transmission lines. *Water Resour. Res.*,16, 574-582,1980.
- Van Genuchten, M. A closed-form equation for predicting the hydraulic conductivity of unsaturated soils, *Soil Sci. Soc. Amer. J.*,44, 892-898, 1980.
- Verhoef, A., Fernández-Gávez, J., Diaz-Espejo, A., Main, B.E. and El-Bishi, M. The diurnal course of soil moisture as measured by various dielectricsensors: Effects of soil temperature and the implications for evaporation estimates. *J. Hydrol.* 321:147-162, 2006.
- Westcot, D.W. and Wierenga, P.J. Transfer of heat by conduction and vapor movement in a closed system. *Soil Sci. Soc. Am. J.*, 38, 9-14, 1974.



## 2 Error Induced by Discrete Flux Calculation

This short chapter resumes the results of a theoretical analysis that we have conducted about the systematic errors induced by the use of discrete data for flux-estimates, whose relevance for this thesis is crucial. The full paper, *Lunati et al.* [2012] is attached in Appendix A.

### 2.1 Introduction

Fluxes from discrete measurements are calculated in the gradient method [*Tanner*, 1963], to compute heat flux in field soils [*Kimball et al.*, 1976; *Cobos and Baker*, 2003; *Liebenthal et al.*, 2005; *Assouline et al.*, 2010] or snow [*Jeffries and Morris*, 2005; *Sturm et al.*, 2001], and, more recently, diffusive fluxes of greenhouse gases during soil respiration [*Hirano*, 2005; *Barron-Gafford et al.*, 2011; *Wolf et al.*, 2011]. The residual of discrete balance equations is also used to estimate sensible [*Sharratt et al.*, 1992] or latent-heat flux at the land surface [*Mayocchi and Bristow*, 1995; *Castellvi and Snyder*, 2010]; subsurface soil-water evaporation [*Heitman et al.*, 2008a,b]; or ground surface temperature [*Bhumralkar*, 1975; *Lin*, 1980]. *Rose* [1968a,b]; *Jackson et al.* [1974]; *Cahill and Parlange* [1998]; *Parlange et al.* [1998] use the residual of discrete balance equations for total moisture (Eq. 1.4) and for energy (Eq. 1.8) to estimate thermal vapor fluxes. This approach results in general in vapor fluxes which are much larger than those predicted by PdV theory, even accounting for enhancing mechanisms.

As seen in Sec. 1.2 many investigators ascribe this mismatch to a poor description of the involved processes and to wrong physical descriptions, focusing their research accordingly. We tackle the problem from a different perspective and we analyze the systematic errors that arise calculating mass and energy balances from discrete measurements.

We show how large residuals may result when finite difference approximations are used to compute fluxes and storage terms, even assuming no measurements or model errors. We

## Chapter 2. Error Induced by Discrete Flux Calculation

Table 2.1: Thermal diffusivity,  $D$  [ $\text{m}^2/\text{s}$ ], and penetration depth  $1/k$  [m] for different materials and different forcing periods  $\tau$ .

	$D$ [ $\text{m}^2/\text{s}$ ]	$1/k$ [m]					
		$\tau = 1y$	$\tau = 1d$	$\tau = 0.5d$	$\tau = 1h$	$\tau = 1min$	$\tau = 1s$
Quartz sand, dry	$2.0 \cdot 10^{-7} \text{ }^a$	1.42	0.074	$5.2 \cdot 10^{-2}$	$1.5 \cdot 10^{-2}$	$2.0 \cdot 10^{-3}$	$2.5 \cdot 10^{-4}$
Quartz sand, water 8.3%	$3.4 \cdot 10^{-7} \text{ }^a$	1.85	0.097	$6.8 \cdot 10^{-2}$	$2.0 \cdot 10^{-2}$	$2.5 \cdot 10^{-3}$	$3.3 \cdot 10^{-4}$
Sandy clay, water 15.0%	$3.8 \cdot 10^{-7} \text{ }^a$	1.95	0.102	$7.2 \cdot 10^{-2}$	$2.1 \cdot 10^{-2}$	$2.7 \cdot 10^{-3}$	$3.5 \cdot 10^{-4}$
Soil (average)	$4.6 \cdot 10^{-7} \text{ }^b$	2.15	0.112	$8.0 \cdot 10^{-2}$	$2.3 \cdot 10^{-2}$	$3.0 \cdot 10^{-3}$	$3.8 \cdot 10^{-4}$
Calcareous earth, water 43.0%	$1.9 \cdot 10^{-7} \text{ }^a$	1.38	0.072	$5.1 \cdot 10^{-2}$	$1.5 \cdot 10^{-2}$	$1.9 \cdot 10^{-3}$	$2.5 \cdot 10^{-4}$
Snow (fresh)	$5.0 \cdot 10^{-7} \text{ }^b$	2.24	0.127	$8.3 \cdot 10^{-2}$	$2.4 \cdot 10^{-2}$	$3.1 \cdot 10^{-3}$	$4.0 \cdot 10^{-4}$
Snow (densely packed)	$4.1 \cdot 10^{-7} \text{ }^a$	2.03	0.106	$7.5 \cdot 10^{-2}$	$2.2 \cdot 10^{-2}$	$2.8 \cdot 10^{-3}$	$3.6 \cdot 10^{-4}$
Water	$1.4 \cdot 10^{-7} \text{ }^b$	1.20	0.063	$4.5 \cdot 10^{-2}$	$1.3 \cdot 10^{-2}$	$1.7 \cdot 10^{-3}$	$2.1 \cdot 10^{-4}$

<sup>a</sup>Ingersoll and Koepp [1924]. <sup>b</sup>Carslaw and Jaeger [1959].

demonstrate that this happens in particular when the thickness of the soil layer where the balance is computed is comparable to the penetration depth  $1/k$  of the temperature forcing acting on that layer.

Looking at Tab. 2.1 for several sands and a finer soil (characterized by different thermal diffusivities  $D$ ) exposed to natural diurnal solar forcing ( $\sim 6\text{-}12$  cm), it appears that this is easily the case in many studies.

## 2.2 Analysis Performed

To investigate mass and energy residuals in case of simultaneous heat and soil moisture transfer we numerically solve the coupled PdV equations (Eq. 1.4) and (Eq. 1.8) (heat of wetting  $W$ , vapor advection and any enhancement factor for vapor fluxes are neglected). A time-implicit finite-volumes scheme is used.

We simulate the evaporation from a soil bucket similar to the experiment by Assouline *et al.* [2010] for a sand, a loam and a clayey loam soils.

A temperature forcing and an evaporative flux (based on values measured by Assouline *et al.* [2010]) are assigned at the upper boundary, representing the soil surface, whereas at the bottom no-flux conditions are imposed.

$T$  and  $\theta_l$  profiles are calculated every 60 s at 0.1 cm spatial resolution over 25 cm of height, but we only use the values at two depths ( $z_T$  and  $z_B$ ) and three depths ( $z_U$ ,  $z_C$ ,  $z_D$ ) to define a control layer of thickness  $\Delta z$  (shadowed zone in Fig. 2.1) where we estimate the heat and



moisture balances with the corresponding residuals (normalized by the amplitude of the corresponding storage term, Eq. 2.1), adopting a direct flux (DM), a finite difference (FD) and a linearly interpolated finite difference (LFD) approximation (higher order than FD), respectively.

The normalized residuals for the three approximations are given by:

$$R_i(t) = \frac{Q_i(t) - F_i(t)}{|Q_i|}, \quad i = \text{fd, lfd, dm} \quad (2.1)$$

where  $Q_i(t)$  and  $F_i(t)$  are the storage and fluxes terms, respectively.

We fix  $z_U = 1$  cm and  $z_D = 10$  cm and we perform the analysis for three different positions of the mid-probe at  $z_C = 4$  cm ( $\alpha = 1/3$ ), 5.5 cm ( $\alpha = 1/2$ ), and 7 cm ( $\alpha = 2/3$ ) to investigate the sensitivity of the residuals to the distance between the measurements.

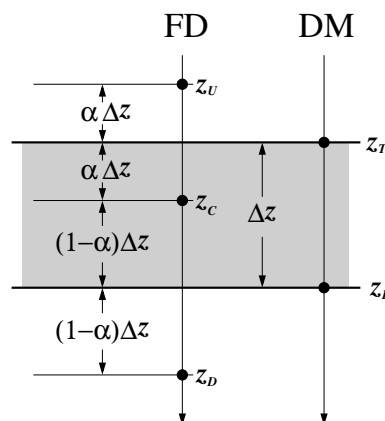


Figure 2.1: The control interval for the Finite Difference (FD, left) and the Direct flux measurement (DM, right) methods (not used).  $\alpha$  measures the relative position of  $z_C$  in the control layer; if  $\alpha = 1/2$  the layer is centered on  $z_C$ ; if  $\alpha < 1/2$ ,  $z_C$  is closer to the top of the layer; and if  $\alpha > 1/2$ ,  $z_C$  is closer to the bottom

## 2.3 Results

Fig. 2.2 shows  $T$  and  $\theta_l$  temporal evolution (a),(b) at three depths for the case of a loamy soil exposed to a three days of evaporation and temperature forcing. The corresponding energy (c) and mass (d) budgets, calculated using the FD scheme and normalized by the amplitude of the respective storage terms. The control layer is 4.5 cm thick, whereas the calculated penetration depth of about 10 cm is also shown assuming an average thermal diffusivity in the  $\theta_l$  interval simulated.

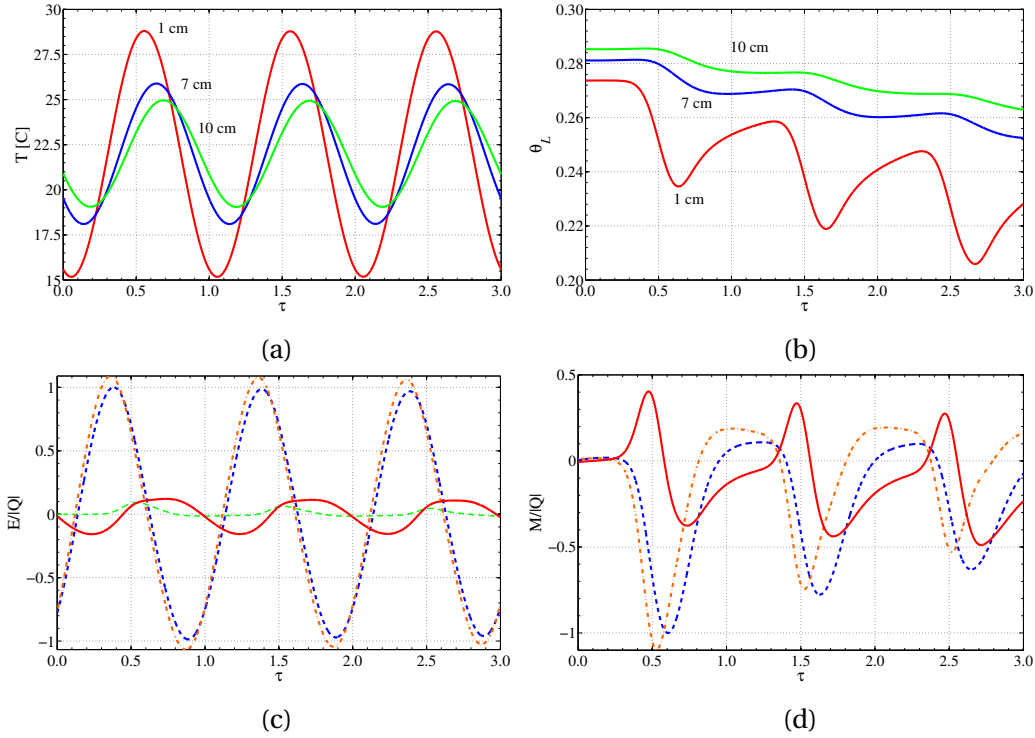


Figure 2.2: Simulated temperature (a) and soil moisture (b) evolution at at three different depths for the loamy soil. These depths correspond to a control layer of thickness  $\Delta z = 4.5$  cm and  $\alpha = 2/3$ . An analysis of the energy balance with this discrete data (c) shows that the contribution of the convective heat fluxes (dotted line) is small compared to the conductive heat flux (dot-dashed line) and the storage (dashed line). The normalized energy residual (solid line) is  $|R_{fd}| \approx 0.14$ . The analysis of the soil moisture balance (d) yields a much larger normalized residual (solid line); the contribution of vapor fluxes is not shown because it is negligible compared to liquid flux (dot-dashed line) and storage (dashed line).

### Energy Residual

In Fig. 2.2 (c) we see that conduction is the dominant heat transport mechanism whereas convection is negligible. Even in this simple 1-D heat diffusion problem, the energy residual has peaks of  $\sim 14\%$ . This is mainly due to the irregular spacing between  $z_U$ ,  $z_C$  and  $z_D$  ( $\alpha = 2/3$ ), to which the system is very sensitive. When  $\alpha = 1/2$ , the energy residual drops to values around 4% (Fig. 2.3 (a)).

### Mass Residual

The same analysis performed for the mass balance equation reveals that mass balance residuals are much larger. This is caused by the nonlinearity of Eq. 1.4 in which hydraulic conductivity and matric potential depend on  $\theta_l$ . Nonlinear effects increase in drier media and lead to larger residual for later evaporative cycles. In Fig. 2.2(d), the peak-to-peak amplitude varies from 80% of the storage term in the first evaporative cycle, to more than 100% at the third day.

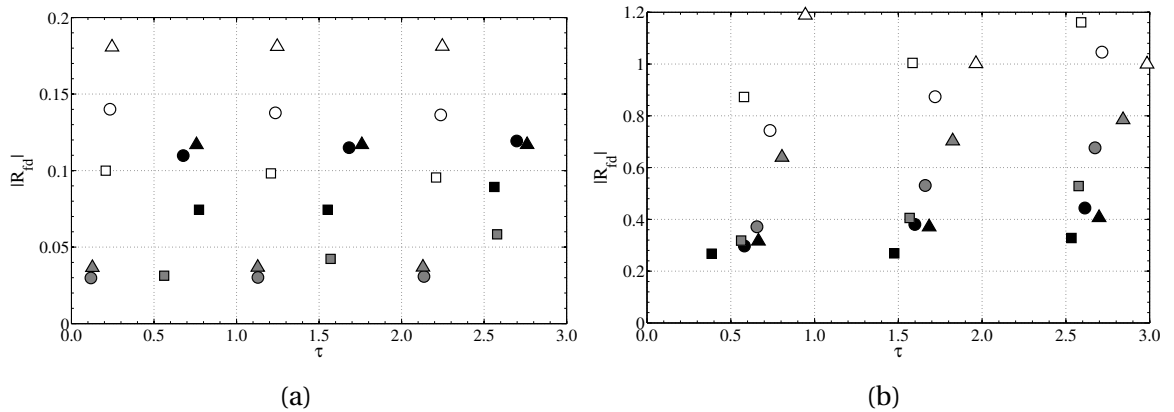


Figure 2.3: Normalized energy (a) and mass (b) balance residual computed with the FD scheme: daily amplitudes for sand (squares), loam (circles), and clayey loam (triangles); the colors correspond to different values of  $\alpha$ , i.e.  $1/3$  (black),  $1/2$  (gray), and  $2/3$  (white). For each evaporative cycle, symbols are placed at the time corresponding to the minimum (most negative) residual.

Better results are obtained for  $\alpha = 1/3$ , but  $|R_{fd}|$  still varies between 25% and 45%. The LFD approximation improves the estimate of the storage term and leads to a lower residual in particular for loam and sand for  $\alpha = 1/2$  but not for clayey loam, for which the mass balance error is dominated by inaccurate shallowest fluxes, not improved by the LFD scheme.

### 2.3.1 Cumulative Residual

For coupled heat and moisture transfer the cumulative residual over time are not zero. This is due to the presence of an evaporative trend and to nonlinear effects. While the cumulative residual for energy is characterized by periodic oscillations around a mean negative value which remains stable with the evaporative cycles, a clear negative trend is visible in the cumulative mass residual indicating that the error due to the use of discrete fluxes and accumulation terms does not average out at longer time scale (Fig. 2.4). We observe that the predicted trend is consistent with the drying of the bucket. In a field situation, where measurements of vapor flux and storage are not available, this residual could be misinterpreted as a real subsurface evaporation.

## 2.4 Conclusions

Although in theory the error induced by the direct use of discrete measurements of continuous quantities could be arbitrarily reduced by increasing the spatial resolution, in practice several

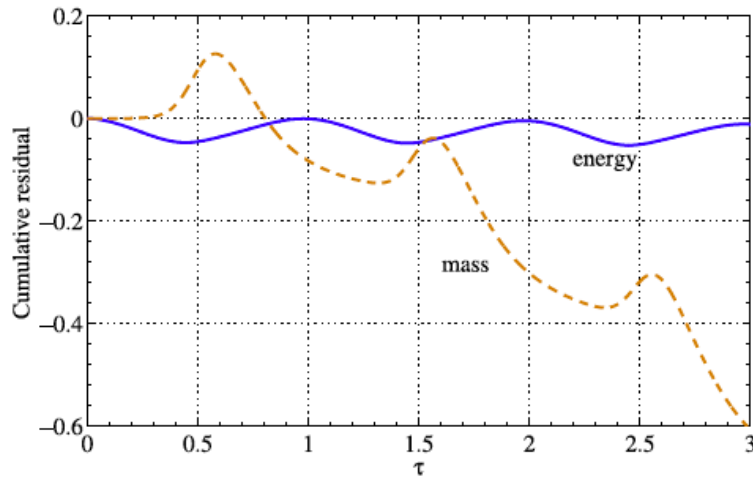


Figure 2.4: Cumulative mass (dotted line) and energy (solid line) residuals for the loamy soil. The case corresponds to that shown in Fig. 2.2

physical limitations (e.g., the finite size or the finite footprint of the sensors) and logistic constraints (e.g., the maximum number of probes available or manageable in a field campaign) set an upper limit to the highest possible spatial resolution.

We show that careful assessment of the systematic energy and mass error introduced by the use of spatially discrete data is required before using residuals computed directly from field measurements, particularly when solar radiation induces diurnal cycles of surface temperature and evaporation.

We find that large residuals arise also without experimental or model errors and any uncertainty on soil properties, only caused by the inability of a linear approximation to capture temperature and water content profile with a satisfactory level of accuracy.

Larger residuals are expected in poorly conductive or highly capacitive soils, as well as in presence of high-frequency forcing. To obtain a satisfactory balance closure, it is necessary to consider control layers which are sufficiently smaller than the penetration depth.

We also proved that residuals are very sensitive to the displacement of the mid-measurement point.

Whenever possible, an equal spacing associate with a LFD (or higher order) approximation is the best solution to reduce both residuals. However, the nonlinear nature of liquid fluxes (due to the dependence of relative conductivity and matric potential on the water contents) can lead to extremely large errors also in this case.

Although we have investigated the case of conduction dominated heat transport, the results naturally extend to any problem which is diffusion dominated and provide an indication of the applicability of the gradient based method to compute field fluxes. In particular, they naturally extend to recent applications of the gradient method to compute diffusive gas fluxes during soil respiration.

## Bibliography

- Assouline, S., Narkis, K., Tyler, S.W., Lunati, I., Parlange, M.B. and Selker, J.S. On the diurnal soil water content dynamics during evaporation using dielectric methods. *Vadose Zone J.*, 9, 709-718, 2010.
- Barron-Gafford, G.A., Scott, R.L., Jenerette, G.D. and Huxman, T.E. The relative controls of temperature, soil moisture, and plant functional group on soil CO<sub>2</sub> efflux at diurnal, seasonal, and annual scales. *J. Geophys. Res.* 116:G01023, 2011.
- Bhumralkar, C.M. Numerical experiments on the computation of ground surface temperature in an atmospheric general circulation model. *J. Appl. Meteor.*, 14:1246-1258, 1975.
- Cahill, A.T. and Parlange M.B. On water vapor transport in field soils *Water Resour. Res.*, 34(4), 731-739, 1998.
- Carsel, R.F. and Parrish, R.S. Developing joint probability distributions of soil water retention characteristics. *Water Resour. Res.*, 24(5):755-769, 1988.
- Carlsaw, H.S. and Jaeger, J.C. *Conduction of heat in solids*. 2nd ed., Clarendon Press, Oxford, U. K., 13.7.3-4, pp 344-345, 1959.
- Carlsaw, H.S. and Jaeger, J.C. *Conduction of heat in solids* 2nd ed., Clarendon Press, Oxford, U. K., 10.4, pp 261-262, 1959.
- Castellví, E. and Snyder, R.L. A comparison between latent heat fluxes over grass using a weighing lysimeter and surface renewal analysis. *Journal of Hydrology*, 381, 213-220, 2010.
- Cobos, D.R. and Baker, J.M. In situ measurement of soil heat flux with the gradient method. *Vadose Zone J.*, 2: 589-594, 2003.
- Heitman, J.L., Horton, R., Sauer, T.J. and De Sutter, T.M. Sensible heat observations reveal soil-water evaporation dynamics. *J. Hydrometeorol.*, 9, 165-171, 2008.
- Heitman, J.L., Xiao, X., Horton, R. and Sauer, T.J. Sensible heat measurements indicating depth and magnitude of subsurface soil water evaporation. *Water Resour. Res.*, 44:W00D05, 2008.
- Hirano, T. Seasonal and diurnal variations in topsoil and subsoil respiration under snowpack in a temperate deciduous forest. *Global Biogeochem. Cycles* 19:GB2011, 2005

## Bibliography

---

- Ingersoll, L.R. and Koepp, O. A. Thermal Diffusivity and Conductivity of some Soil Materials. *Phys. Rev.*24:92-93, 1924.
- Jackson, R.D. Diurnal changes in soil water content during drying *Field Soil Water Regime, Spec. Publ.*, 5, edited by R. R. Bruce et al., pp 37-55, Soil Sci. Soc. of Am., Madison, Wis., 1973.
- Jackson, R.D., Reginato, R.J., Kimball, B.A. and Nakayama, F.S. Diurnal soil-water evaporation: Comparison of measured and calculated soil-water fluxes *Soil Sci. Soc. Am. J.*, 38, 861-866, 1974.
- Jeffries, M.O. and Morris, K. Instantaneous daytime conductive heat flow through snow on lake ice in Alaska. *Hydrol. Process.*, 20:803-815, 2006.
- Kimball, B.A., Jackson, R.D., Nakayama, F.S., Idso, S.B. and Reginato, R.J. Soil-heat flux determination: Temperature gradient method with computed thermal conductivities. *Soil Sci. Soc. Am. J.* 40:25-28, 1976.
- Liebenthal, C., Huwe, B. and Foken, T. Sensitivity analysis for two ground heat flux calculation approaches. *Agricultural and Forest Meteorology*, 132:253-262, 2005.
- Lin, J.D. On the force-restore method for prediction of ground surface temperature. *J. Geophys. Res.*, 85:3251-3254, 1980.
- Lunati, I., Ciocca, F. and Parlange, M.B. On the use of spatially discrete data to compute energy and mass balance *Water Resour. Res.*, 48, 1-10, 2012.
- Mayocchi, C.L. and Bristow, K.L. Soil surface heat flux: some general questions and comments on measurements. *Agricultural and Forest Meteorology* 75:43-50, 1995.
- Mualem, Y. A new model for predicting the hydraulic conductivity of unsaturated porous media *Water. Resour. Res.* 12(3), 513-522, 1976b.
- Parlange, M.B., Cahill A.T., Nielsen D.R., Hopmans J.W. and Wendroth, O. Review of heat and water movement in field soils. *Soil Tillage Res*, 47:5-10, 1998.
- Rose, C.W. Water transport in soil with a daily temperature wave, I, Theory and experiment. *Aust. J. Soil Res.*, 6, 31-44, 1968a.
- Rose, C.W. Water transport in soil with a daily temperature wave, II. *Aust. J. Soil Res.*, 6, 45-57, 1968b.
- Sharratt, B.S., Campbell, G.S. and Glenn, D.M. Soil heat flux estimation based on the finite-difference form of the transient heat flow equation. *Agricultural and Forest Meteorology*, 61:95-111, 1992
- Sturm, M., Holmgren, J. and Perovich, D.K. Spatial variations in the winter heat flux at SHEBA: estimates from snow-ice interface temperatures. *Annals of Glaciology*, 33:213-220, 2001.

- Tanner, C.B. Basic instrumentation and measurements for plant environment and micrometeorology. *Soils Bull.*, 6, Dep. of Soil Sci., Univ. of Wisconsin, Madison, 1963.
- Van Genuchten, M.Th. A closed form equation for predicting the hydraulic conductivity of unsaturated soils. *Soil Sci. Soc. Am. J.*, 44:892-898, 1980.
- Wolf, B., Chen, W., Brueggemann, N., Zheng, X., Pumpanen, J. and Butterbach-Bahl, K.. Applicability of the soil gradient method for estimating soil-atmosphere CO<sub>2</sub>, CH<sub>4</sub>, and N<sub>2</sub>O fluxes for steppe soils in Inner Mongolia. *J. Plant Nutr. Soil Sci.* 174:359-372, 2011.





# 3 Retention Curves and Evaporation

## Part I: the Isothermal Case

This chapter has been submitted for publication with the following citation:

Ciocca, F., Lunati, I., Parlange, M.B. (2013): Effects of the water-retention curve on evaporation from dry soils. *Geophysical Research Letters*.

**Abstract:** *Water retention curves which approach infinity at residual water content are widely employed to model soil-moisture dynamics. These retention models fail to satisfactorily describe evaporation from dry soil (moisture-limited regime) because they do not allow the soil to dry below residual water content. We show that simple modifications can be introduced to prevent infinite water retention at residual water content and predict more physically sound moisture dynamics: modified retention models that allow drying below residual, predict a moisture-limited regime characterized by a thin subsurface evaporation zone, and produce vapor fluxes three times larger than classical retention models, which might reduce the needs to introduce empirical enhancement factors. Predictions of the modified retention curves are more consistent with experimental observations and improve the capability of modeling evaporation into the atmosphere and runoff in dry regions.*

### 3.1 Introduction

Water-retention and unsaturated-conductivity curves dictate soil moisture dynamics in field soils and determine infiltration, runoff, and evaporation into the atmosphere. As accurate measurements are difficult and costly, particularly in dry soils, information about water-retention curve for a wide spectrum of water content are rarely available.

In most applications, typical values are taken from the literature or obtained by fitting water-content and matric-potential data to parametric models [*Brooks and Corey*, 1964; *Brutsaert*, 1966; *Van Genuchten*, 1980]; and the unsaturated hydraulic conductivity is calculated from the water-retention curve by means of analytical models [*Burdine*, 1952; *Mualem*, 1976]. This tight relationship between conductivity and matric potential has led to a widespread use of water-retention curves that approach infinite at the residual water content and that are not defined below this threshold. Whereas this has no significant implication if only liquid flux is considered, it severely limits the ability to correctly model vapor dynamics.

From a physical viewpoint, a residual water content arises due to the existence of a percolation threshold below which the liquid phase is not connected and cannot flow according to Darcy-Buckingham equations [see, e.g., *de Gennes*, 1983; *Wilkinson and Willemsen*, 1983]. When liquid connectivity is lost, however, water vapor is still present in the system and the menisci of the trapped liquid clusters have a finite curvature.

A matric potential that becomes infinite at residual water content contrasts with the microscopic observation of finite curvature of the menisci and implies zero vapor density. Establishing the exact behavior of the water retention curves close to (or below) the residual water content is difficult because measurements are time consuming and data are rare; essentially, only one reliable dataset is available in the literature [*Campbell and Shiozawa*, 1992]. Few modified water-retention models have been proposed to better describe these data [e.g., *Campbell and Shiozawa*, 1992; *Rossi and Nimmo*, 1994; *Fayer and Simmons*, 1995; *Webb*, 2000]. However, only few recent studies have employed these models to simulate soil moisture dynamics [*Silva and Grifoll*, 2007; *Sakai et al.*, 2009; *Smits et al.*, 2012; *Tang and Riley*, 2013] whereas standard water-retention curves that approach infinite at residual water content remain widely employed [see, e.g. *Grifoll et al.*, 2005; *Mortensen et al.*, 2006; *Sakaki and Illan-gasekare*, 2007; *Assouline et al.*, 2010; *Shokri and Salvucci*, 2011; *Smits et al.*, 2011; *Assouline*, 2013; *Campoy et al.*, 2013; *Mirus and Loague*, 2013]. In this letter, we demonstrate the effects of the water-retention behavior close to residual on the evaporative fluxes from dry soils and we discuss their implications for soil moisture dynamics.

### 3.2 Water-retention curve and vapor density

Although the analysis can be applied to any classical retention model, we focus on the *Van Genuchten* [1980] model (hereafter VG) which is one of the most popular in soil science. Then, the matric potential is

$$\psi(S_{\text{eff}}) = \frac{1}{\alpha} \left( S_{\text{eff}}^{-\frac{n}{n-1}} - 1 \right)^{1/n}, \quad (3.1)$$

where  $\alpha > 0$  and  $n > 1$  are two model parameters related to the inverse air-entry suction and to the pore-size distribution, respectively;  $S_{\text{eff}} = \frac{\theta_l - \theta_r}{\theta_m - \theta_r}$  is the effective saturation (or normalized water content);  $\theta_l$  the liquid water content;  $\theta_m$  is the maximum water content, which is in general assumed equal to the porosity  $\phi$ ; and  $\theta_r$  is the residual water content. The VG model is typically employed together with the Mualem model, which yields the unsaturated conductivity [Mualem, 1976]:

$$K(S_{\text{eff}}) = K_s S_{\text{eff}}^{1/2} \left[ 1 - \left( 1 - S_{\text{eff}}^{\frac{n}{n-1}} \right)^{1-1/n} \right]^2, \quad (3.2)$$

where  $K_s$  is the saturated conductivity of the soil.

At equilibrium, the vapor density,  $\rho_v$ , is related to the matric potential,  $\psi$ , through the Kelvin equation [Edlefsen and Anderson, 1943],

$$\rho_v = \rho_v^* \exp\left(-\frac{\psi g}{RT}\right), \quad (3.3)$$

where  $\rho_v^*$  is the saturated vapor density of bulk water;  $T$  the temperature;  $R$  the gas constant of water; and  $g$  the gravity acceleration. When the water content approaches the residual value, the unsaturated conductivity becomes zero and liquid fluxes vanish. At the same time, the matric potential approaches infinity and Eq. 3.3 implies that  $\rho_v$  vanishes, which precludes the soil from drying below residual saturation due to the absence of vapor fluxes.

### 3.3 Modified retention models

If models are modified to prevent infinite values of matric potential above zero water content, the soil can dry below residual saturation as a result of vapor fluxes that continue to remove soil water after liquid fluxes stop. There are several ways to achieve this. The simplest one is to replace the effective saturation by the saturation,  $S = \theta_l / \phi$ , in Eq. 3.1, i.e.,

$$\psi_{\text{MVG}}(S) = \frac{1}{\alpha} \left( S^{-\frac{n^*}{n^*-1}} - 1 \right)^{1/n^*}, \quad (3.4)$$

whereas the unsaturated conductivity remains a function of  $S_{\text{eff}}$ . This choice highlights the fact that, whereas the conductivity is related to the connectivity of the liquid phase and must vanish at residual water content, the matric potential is related to the variation of surface free energy [Ferrari and Lunati, 2013], which is well defined and nonzero also when the liquid connectivity is lost. In the following we will refer to this model as the Modified Van Genuchten model (henceforth MVG).

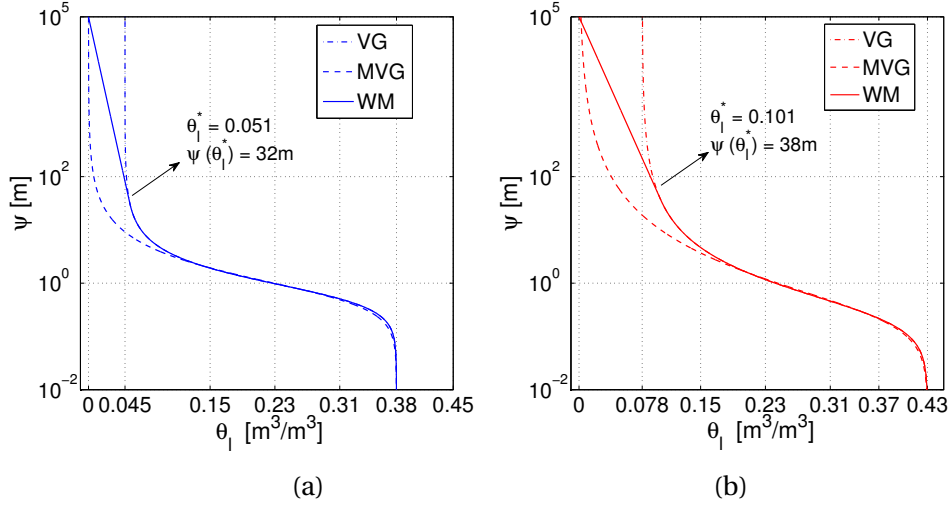


Figure 3.1: Plots of the matric potential-water content relationships used for sand (a) and loam (b): the dashed-dotted curves correspond to the standard van Genuchten model (VG); the dashes curves are modified van Genuchten curves (MVG); and the solid curves correspond to the Webb model (WM).

Another possibility is to use one of the extensions proposed to fit the *Campbell and Shiozawa* [1992] dataset. Here we focus on the *Webb* [2000] model (henceforth WM), which modifies the VG model to account for the exponential dependency of the matric potential on the water content that *Campbell and Shiozawa* [1992] have observed in the dry region for six soil types. In dry soils, *Webb* [2000] assumes that if  $\theta_1 > \theta_1^*$  the VG model is valid, whereas

$$\psi_W(\theta_1) = 10^{[\gamma(\theta_1 - \theta_1^*) + \log_{10} \psi^*]} \quad \text{if } \theta_1 < \theta_1^*, \quad (3.5)$$

where  $\theta_1^*$  is the water content value at matching point for which Eq. 3.5 is tangent to the VG retention curve, Eq. 3.1, and  $\psi^* = \psi(\theta_1^*) = \psi_W(\theta_1^*)$ . Given a finite intercept at zero saturation,  $\psi_0 = \psi_w(0)$ , the matching point is uniquely defined.

In general  $\psi_0 = 10^5 \text{m}$ , which is the common oven-dried value of matric potential found in many experiments [e.g. *Ross et al.*, 1991].

The retention curves of typical sand and loam soils obtained with the three models (VG, MVG, and WM) are plotted in Fig. 3.1 for the parameters listed in Tab. 3.1. Notice that the pore-size distribution parameter of the MVG curve,  $n^*$ , is different from the VG curve and has been chosen to guarantee the maximum overlap between the three models in the wet region where data are in general more common and reliable. As a results, the MVG curves diverge from the VG curves at water content about twice higher than residual, whereas the WM and the VG curves diverge at the matching, which is closer to the residual saturation.

### 3.4. Isothermal evaporation from soil columns

	Hydraulic properties <sup>a,b</sup>							Atmospheric parameters				
	$K_s$ [m/s]	$\alpha$ [1/m]	$n$ [-]	$\theta_r$ [-]	$\phi$ [-]	$\theta_1^*$ [-]	$n^*$ [-]	$H_r^{\text{air}}$ [%]	$\rho_v^a$ [kg/m <sup>3</sup> ]	$U_{\text{air}}$ [m/s]	$E_{\text{max}}$ [mm/d]	$T$ [°C]
SA <sup>a</sup>	8.49 10 <sup>-5</sup>	1.51	2.04	0.045	0.38	0.051	1.810	60	0.0138	0.56	0.95	25
LO <sup>b</sup>	2.89 10 <sup>-6</sup>	3.6	1.56	0.078	0.43	0.101	1.404	30	0.0069	1.0	3.00	25

Table 3.1: Hydraulic parameters for sand (SA) and loam (LO), and atmospheric forcing. The temperature  $T$  is constant both in the air and the soil.

<sup>a</sup> Carsel and Parrish [1988].

<sup>b</sup> From API database: <http://www.env.gov.bc.ca/epd/remediation/reports/pdf/LNAPL-guidance.pdf>.

### 3.4 Isothermal evaporation from soil columns

To investigate the effects of the three retention models on evaporation we simulate the drying of two columns of height 0.1 m that have been homogeneously packed with two different soils: a medium grained sand and a loam whose hydraulic properties are listed in Tab. 3.1. We assume isothermal conditions (25°C) and equilibrium between the water vapor and liquid water (Eq. 3.3). Soil moisture dynamics are governed by the mass balance equation [Philips and de Vries, 1957]

$$\frac{\partial}{\partial t} [\rho_l(\theta_l + \theta_v)] + \frac{\partial}{\partial z} [j_l(\theta_l) + j_v(\theta_l)] = 0 \quad (3.6)$$

where  $\theta_v = (\phi - \theta_l)\rho_v/\rho_l$  is the water vapor content (expressed as volumetric content of the equivalent liquid water of density  $\rho_l$ );

$$j_v = -D_v(\theta_l)\nabla\rho_v, \quad (3.7)$$

is the Fickian vapor fluxes, where  $D_v = (\phi - \theta_l)^{10/3}\phi^{-2}D_v^m$  is the unsaturated diffusion coefficient in the porous medium and  $D_v^m$  the molecular diffusion coefficient of water vapor in air;

$$j_l = \rho_l K(\theta_l) \left( \frac{d\psi}{d\theta_l} \frac{\partial\theta_l}{\partial z} - 1 \right) \quad (3.8)$$

is the liquid flux that includes matric potential and gravity component;  $K$  is the unsaturated hydraulic conductivity described by the Mualem-van Genuchten model (Eq. 3.2).

Drying is simulated with the three different water retentions models (VG, MVG, and WM) starting from the same initial conditions ( $\theta_0 = 0.37$ ). After 4 days of relaxation to equilibrate with gravity, the soil surface is exposed to atmospheric forcing and evaporation starts. While the bottom boundary is impermeable to water flux, at the top boundary we assign an evaporative forcing described by the aerodynamic diffusion relationship [Anderson, 1976]:

$$E = \frac{k^2 U_{\text{air}} \gamma}{\rho_1 [\ln(z_a/z_0)]^2} (\rho_v^s - \rho_v^a) \quad (3.9)$$

where  $k = 0.35$  is the von Karman's constant;  $\gamma = 1$  the stability factor;  $z_0 = 0.001\text{m}$  the surface roughness length;  $\rho_v^s$  is the vapor density at the soil surface;  $z_a = 2\text{m}$  the screen height in the atmosphere at which the wind speed,  $U_{\text{air}}$ , and the air moisture density (or absolute humidity),  $\rho_v^a$ , are assigned.

Values for  $U_{\text{air}}$  and  $\rho_v^a$  are listed in Tab. 3.1 together with the corresponding air relative humidity,  $H_r^{\text{air}}$ , and the potential evaporation rates,  $E_{\text{max}}$ .

The equations above are discretized on a one dimensional grid consisting of 100 equally-spaced cells of individual size 0.001 m and solved numerically (further details on the numerical method can be found in *Lunati et al.* [2012]).

### 3.5 Results and discussion

Evaporation can be classified into two main regimes: an energy-limited regime, characteristic of wet soil, and a moisture-limited regime, typical of dry conditions [see, e.g. *Brutsaert*, 1982]. In the energy-limited regime, the evaporation occurs at the soil surface and at potential evaporation rate,  $E_{\text{max}}$ , which depends on the atmospheric demand and not on the soil moisture. Initially, drying follows this regime and the cumulative evaporation increases steadily with time (Fig. 3.2). The energy-limited regimes last about 32 days after evaporation started in the sand and 6 days in the loam columns. During this period, all three retention models predict the same evaporation because they are very similar for wet soils. At drier conditions, water fluxes become unable to sustain the potential evaporation,  $E_{\text{max}}$ , and moisture loss is limited not by the atmospheric demand but by moisture availability and removal from the deeper soil. In this regime, the differences between the three retention models are significant. In the sand column (Fig. 3.2.a) the VG model predicts a short moisture-limited regime: after about 14 days the whole column is at residual water content and evaporation stops. MVG and WM simulations exhibit a longer evaporation that continues after the average soil moisture has reached the residual value. During the moisture-limited regime the MVG model predicts a cumulative evaporation three times larger than the VG model (the WM more than two times larger). Drying stops only when the soil vapor density is equal to the air vapor density (i.e.,  $\exp[-\psi(\theta_1)g/RT] = H_r^{\text{air}}$ ).

The loam column displays a similar behavior: in the moisture-limited regime the cumulative evaporation is two times larger with the MVG than with the VG model and with the latter evaporation stops at day 65, when the column water content has reached the residual value (Fig. 3.2.b). The spatiotemporal evolution of the soil moisture in the loam column is shown in Fig. 3.3.

Laboratory observations of evaporation from porous media reveal a persistent moisture-

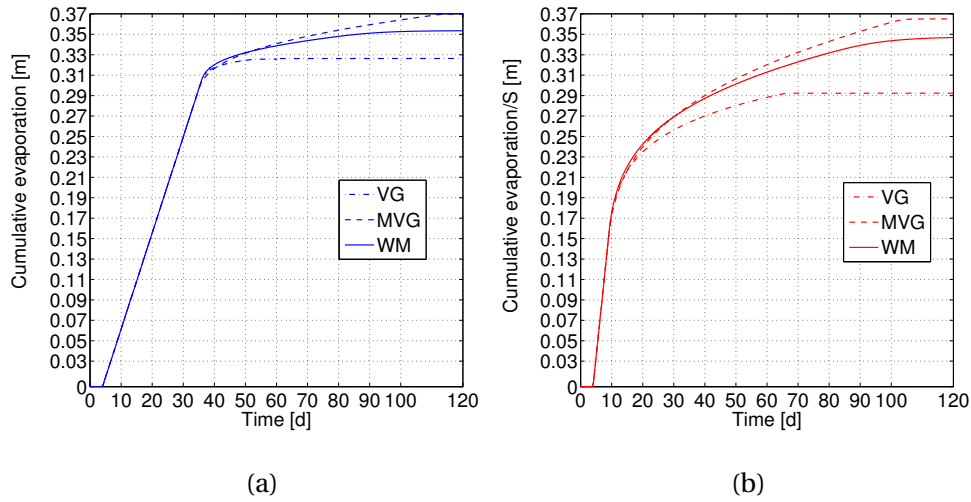


Figure 3.2: Plots of the cumulative evaporation in sand (a) and loam (b). The dashed-dotted curves correspond to the standard van Genuchten model (VG); the dashes curves are modified van Genuchten curves (MVG); and the solid curves correspond to the Webb model (WM).

limited regime for a wide range of grain sizes [Shokri and Or, 2011]. After a rapid transition, Shokri and Or [2011] found that the initial moisture-limited regime exhibited a seemingly constant evaporation rate (below potential) for grain size close to medium-textured sands (0.25-0.50 mm); whereas a steadily decreasing rate was observed with finer grains of size comparable to loam. This behavior is qualitatively well reproduced by the WM and MVG models, but not by the VG model (Fig. 3.2). A detailed inspection of the fluxes supplying

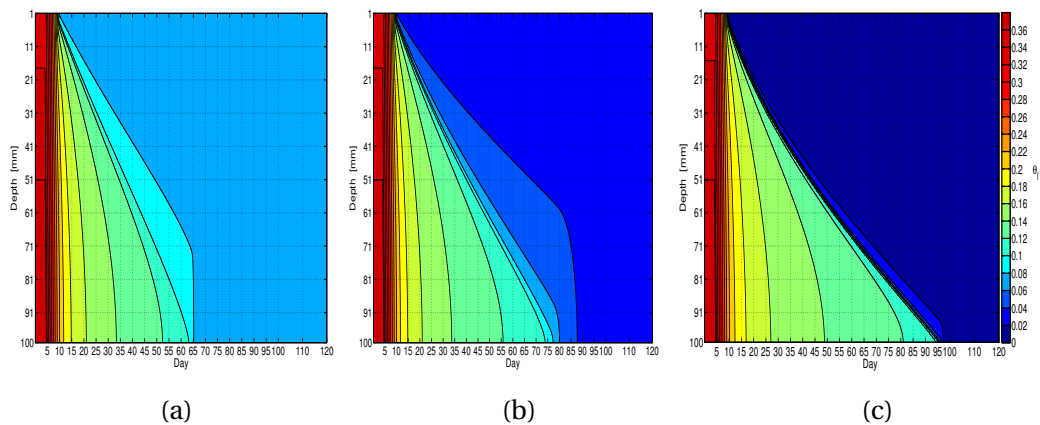


Figure 3.3:  $\theta_1$  trends for loam as function of time (x-axis) and depth (y-axis) simulated using VG (a), WM (b) and MVG (c).

water to the soil surface is shown in Fig. 3.4.a for the loam column. During the energy-limited regime (day 5 through 9) liquid flux is the dominant mechanism which allows sustaining the

potential evaporation rate. During this period the moisture loss into the atmosphere remains constant, whereas the flux from the deeper soil decreases steadily indicating a slow drying of the surface, which progressively reduces the ability of the soil to transport liquid water. The transition to the moisture-limited regime is characterized by an abrupt drop of liquid fluxes followed by a raise of the vapor-flux contribution which reaches a maximum in approximately 0.5 days and then decreases steadily (Fig. 3.4.a1).

During the moisture-limited regime, vapor fluxes are higher and more persistent with the modified models (and in particular with the MVG); the VG model predicts a drastic drop after day 65 which stops the evaporation. Liquid and vapor fluxes along the column profile at day 65 (just before the vapor flux drop in the VG model) are shown in Fig. 3.4.b. In WM and MVG models an evaporation region below the surface can be detected. The MVG model predicts a thinner vaporization region of thickness less than 1 cm (approximately from depth 65 to 72 cm in Fig. 3.4.b), which is located right above the depth of residual water content (see also Fig. 3.3) and it is partially fed by liquid flux from deeper soil. Again, this is in qualitative agreement with laboratory experiments that have observed thin subsurface evaporation regions [Lehmann *et al.*, 2008; Shokri and Or, 2011].

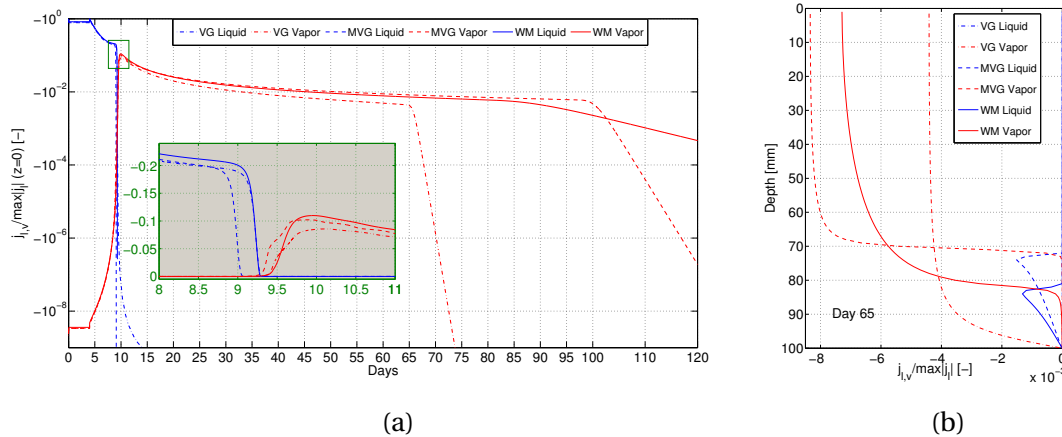


Figure 3.4: Liquid  $j_l$  and vapor flux  $j_v$  for loam as a function of time at the surface in semi-log scale (a). Inset (a1) zooms in at the end of liquid dominated and onset of vapor dominated regime, in linear scale. Figure (b) shows  $j_v$  and  $j_l$  along a vertical profile after 65 days (61 days since evaporation started).

### 3.6 Conclusions

The VG model is unable to correctly predict evaporation in the moisture-limited regime because vapor density becomes zero at residual liquid-water content, and vapor fluxes are suppressed together with liquid fluxes. This seriously limits the ability of this retention model



to describe soil moisture dynamics because it cannot describe vapor-dominated moisture transport. The MVG model overcomes this difficulty by simply postulating that water retention is a function of the saturation, rather than of the effective saturation; the WM assumes that below a threshold value the water retention deviates from the VG model and is an exponential function of the water content. Both models yield a more physically sound description of the moisture-limited regime: vapor fluxes allow drying below residual and stop only when the vapor density is in thermodynamical equilibrium with the atmosphere; evaporation occurs in a thin subsurface evaporation region (less than 1 cm with the MVG model); and vapor fluxes are large (two to three times larger than predicted by the VG retention curve for the cases investigated here), which might largely reduce the needs for empirical enhancement factors introduced to match experimental evaporation rates [see, e.g. *Philips and de Vries*, 1957; *Cass et al.*, 1984]. The simple examples presented demonstrate the importance of the retention curve to describe the moisture-limited regime. When modeling moisture dynamics in semiarid regions, the modified models would lead to significantly higher vapor fluxes into the atmosphere and to larger runoff component due to dryer soil surface. Implications go beyond field-soil dynamics and might also affect global-scale predictions, where the mismatch between in-situ water content data and modeled values at the grid-scale is still unsolved [see, e.g. *Campoy et al.*, 2013]. Our results demand a more careful experimental characterization of water retention close and below residual water content. Although further studies are required to assess the performance of modified retention models in presence of diurnal fluctuations and hysteretic effects, their use to model moisture-limited evaporation regimes is recommended.

**Acknowledgements:** Francesco Ciocca is supported by the SNSF grant number 200021-1222088/1. Ivan Lunati is Swiss National Science Foundation (SNSF) Professor at the University of Lausanne (SNSF grants number PP00P2-123419/1 and 200020-143626/1).



# Bibliography

- Anderson, E. A. (1976), A point energy and mass balance model of a snow cover, *Tech. Rep. Tech. Rep NWS-19*, NOAA, Silver Spring, Md.
- Andraski, B. J. (1996), Properties and variability of soil and trench fill at an arid waste-burial site, *Soil Sci. Soc. Am. J.*, 60, 54–66.
- Assouline, S. (2013), Infiltration into soils : Conceptual approaches and solutions, *Water Resour. Res.*, 49, 1755–1772.
- Assouline, S., K. Narkis, S. W. Tyler, I. Lunati, M. B. Parlange, and J. S. Selker (2010), On the diurnal soil water content dynamics during evaporation using dielectric methods, *Vadose Zone J.*, 9, 709–718.
- Bittelli, M., F. Ventura, G. S. Campbell, R. L. Snyder, F. Gallegati, and P. Rossi Pisa (2008), Coupling of heat, water vapor, and liquid water fluxes to compute evaporation in bare soils, *Journal of Hydrol.*, 362, 191–205.
- Brooks, R. H., and A. T. Corey (1964), Hydraulic properties of porous media, *Hydrology Paper No. 3*, Colorado State Univ.
- Brutsaert, W. H. (1966), Probability laws of pore-size distributions, *Soil Sci.*, 101, 85–91.
- Brutsaert, W. H. (1982), *Evaporation into the Atmosphere: Theory, History and Applications*, 299 pp., Springer, Dordrecht, Netherlands and Boston, MA.
- Burdine, N. T. (1952), Relative permeability calculations from pore-size distribution data, *Trans. Am. Inst. Min. Metall. Pet. Eng.*, 198, 71–78.
- Campbell, G. S., and S. Shiozawa (1992), Prediction of hydraulic properties of soils using particle size distribution and bulk density data, international Workshop on Indirect Methods for Estimating the Hydraulic Properties of Unsaturated Soils, 1992.
- Campoy, A., A. Ducharne, F. Cheruy, F. Hourdin, J. Polcher, and J. C. Dupont (2013), Response of land surface fluxes and precipitation to different soil bottom hydrological conditions in a general circulation model, *Journal of Geophysical Research, Atmosphere*, doi:10.1002/jgrd.50627, accepted article.

## Bibliography

---

- Carsel, R. F., and R. S. Parrish (1988), Developing joint probability distributions of soil water retention characteristics, *Water Resour. Res.*, 24(5), 755–769.
- Cass, A., G. S. Campbell, and T. L. Jones (1984), Enhancement of thermal water vapor diffusion in soil, *Soil Sci. Soc. Am. J.*, 48, 25–32.
- de Gennes, P. G. (1983), Theory of slow biphasic flows in porous media, *Phys. Chem. Hydrol.*, 4(2), 175–185.
- Edlefsen, N. E., and A. B. C. Anderson (1943), Thermodynamics of soil moisture, *Hilgardia*, 15, 31–298.
- Fayer, M. J., and C. S. Simmons (1995), Modified soil water retention functions for all matric suctions, *Water Resour. Res.*, 31(5), 1233–1238.
- Ferrari, A., and I. Lunati (2013), Direct numerical simulations of interface dynamics to link capillary pressure and total surface energy, *Advances in Water Resources*, 57(0), 19 – 31, doi:10.1016/j.advwatres.2013.03.005.
- Grifoll, J., J. M. Gasto, and Y. Cohen (2005), Non-isothermal soil water transport and evaporation, *Adv. Water Res.*, 28, 1254–1266.
- Haverkamp, R., M. Vauclin, J. Touma, P. J. Wierenga, and V. G. (1977), A comparison of numerical simulation models for one dimensional infiltration, *Soil Sci. Soc. Am. J.*, 41, 285–294.
- Lehmann, P., S. Assouline, and D. Or (2008), Characteristic lengths affecting evaporative drying of porous media, *Phys. Rev. E*, 77, 056,309, doi:10.1103/PhysRevE.77.056309.
- Lunati, I., F. Ciocca, and M. B. Parlange (2012), On the use of spatially discrete data to compute energy and mass balance., *Water Resour. Res.*, 48, W05542.
- Mirus, B. B., and K. Loague (2013), How runoff begins (and ends): Characterizing hydrologic response at the catchment scale, *Water Resour. Res.*, 49, 2987–3006.
- Mirus, B. B., B. A. Ebel, C. S. Heppner, and K. Loague (2011), Assessing the detail needed to capture rainfall?runoff dynamics with physics?based hydrologic response simulation, *Water Resour. Res.*, 47(3).
- Morel-Seytoux, H. J., and J. R. Nimmo (1999), Soil water retention and maximum capillary drive from saturation to oven dryness, *Water Resour. Res.*, 35, 2031–2041.
- Mortensen, A. P., J. W. Hopmans, Y. Mori, and J. Simunek (2006), Multi-functional heat pulse probe measurements of coupled vadose zone flow and transport, *Adv. Water Res.*, 29, 250–267.
- Mualem, Y. (1976), A new model for predicting the hydraulic conductivity of unsaturated porous media, *Water Resour. Res.*, 12(3), 513–522.

- Philips, J. R., and D. A. de Vries (1957), Moisture movements in porous materials under temperature gradients, *Transaction of American Geophysical Union*.
- Ross, P. J., J. Williams, and K. L. Bristow (1991), Equations for extending water-retention curves to dryness, *Soil Sci. Soc. Am. J.*, 55, 923–927.
- Rossi, C., and J. R. Nimmo (1994), Modeling of soil water retention from saturation to oven dryness, *Water Resour. Res.*, 30(3), 701–708.
- Sakai, M., N. Toride, and S. J. (2009), Water and vapor movement with condensation and evaporation in a sandy column, *Soil Sci. Soc. Am. J.*, 73(3), 707–717.
- Sakaki, T., and T. H. Illangasekare (2007), Comparison of height-averaged and point-measured capillary pressure-saturation relations for sands using a modified tempe cell, *Water Resour. Res.*, 43, doi:10.1029/2006WR005814.
- Schneider, M., and K. Goss (2012), Prediction of water retention curves for dry soils from an established pedotransfer function: Evaluation of the webb model, *Water Resour. Res.*, 48(6).
- Shokri, N., and D. Or (2011), What determines drying rates at the onset of diffusion controlled stage-2 evaporation from porous media?, *Water Resour. Res.*, 47, W09513, doi:doi:10.1029/2010WR010284.
- Shokri, N., and G. D. Salvucci (2011), Evaporation from porous media in the presence of a water table, *Vadose Zone J.*, 10, doi:doi:10.2136/vzj2011.0027.
- Shokri, N., P. Lehmann, and D. Or (2008b), Effects of hydrophobic layers on evaporation from porous media, *Geophys. Res. Lett.*, 35, L19407.
- Shokri, N., P. Lehmann, and D. Or (2009a), Characteristic of evaporation from partially wettable porous media, *Water Resour. Res.*, 45, W02415.
- Silva, O., and J. Grifoll (2007), A soil-water retention function that includes the hyper-dry region through the bet adsorption isotherm, *Water Resour. Res.*, 43(11).
- Smits, K. M., A. Cihan, T. Sakaki, and T. H. Illangasekare (2011), Evaporation from soils under thermal boundary conditions: Experimental and modeling investigation to compare equilibrium- and nonequilibrium-based approaches, *Water Resour. Res.*, 47, doi:10.1029/2007WR005975.
- Smits, K. M., V. V. Ngo, A. Cihan, T. Sakaki, and T. H. Illangasekare (2012), An evaluation of models of bare soil evaporation formulated with different land surface boundary conditions and assumptions, *Water Resour. Res.*, 48(12).
- Tang, J., and W. Riley (2013), Impacts of a new bare-soil evaporation formulation on site, regional, and global surface energy and water budgets in clm4, *JAME*, doi:10.1002/jame.20034, accepted article.

## Bibliography

---

- Van Genuchten, M. T. (1980), A closed-form equation for predicting the hydraulic conductivity of unsaturated soils, *Soil Sci. Soc. Amer. J.*, 44, 892–898.
- Webb, S. W. (2000), A simple extension of two-phase characteristic curves to include the dry region, *Water Resour. Res.*, 36(6), 1425–1430.
- Wilkinson, D., and J. F. Willemsen (1983), Invasion percolation: a new form of percolation theory, *J. Phys. A: Math. Gen.*, 16, 3365–3376.
- Zhang, Z. F. (2011), Soil water retention and relative permeability for conditions from oven-dry to full saturation, *Vadose Zone J.*, 10, 1299–1308.

## 4 Retention Curves and Evaporation

### Part II: the Diurnal Atmospheric Forcing

This chapter, representing a follow-up of the work presented in Chap.3, is aimed to be submitted for publication with the following citation:

Ciocca, F, Lunati, I., Parlange, M.B. (2013): Evaporation and Extended Retention Curves: the Effect of the Diurnal Cycle on Dry Soils. *in progress*.

**Abstract:** *Evaporation from dry soils (moisture-limited regime) is dictated by vapor dynamics, which are largely determined by soil-water retention. Widely used, classical water-retention models approach infinity at non-zero residual saturation which prevents vapor transport from drying the soil below residual water content and fails to correctly describe evaporation in the moisture-limited regime. Modified water-retention curves that allow vapor flux below residual saturation predict isothermal moisture dynamics at dry regimes more consistent with experimental observations [Ciocca et al., 2013]. Since at dry conditions moisture dynamics are tightly coupled with energy dynamics, we compare the effects of a modified water-retention model on evaporation by simulating the drying of a soil bucket exposed to a diurnal atmospheric forcing. Reduced but longer sustained potential evaporation in the liquid dominated stage (energy-limited regime) and larger evaporation in the moisture-limited regime are predicted with the diurnal forcing. The modified curve produces vapor fluxes three times larger than classical model at the peak of atmospheric forcing in the moisture-limited regime, and larger temperature fluctuations which result in significantly larger sensible and ground heat fluxes at the soil surface.*

### 4.1 Introduction

Evaporation into the atmosphere is crucial to water balance, and is largely affected by hydraulic soil properties such as water-retention and hydraulic conductivity [Smits *et al.*, 2012], which also determine infiltration (see, e.g. Assouline [2013] for a detailed review) and runoff [Mirus *et al.*, 2011; Mirus and Loague, 2013]. Several empirical parameterizations have been proposed to describe the relation between the soil liquid water content  $\theta_L$  and the matric potential  $\psi$  [Brooks and Corey, 1964; Brutsaert, 1966; Haverkamp *et al.*, 1977; Van Genuchten, 1980]. From the water-retention curve, analytical models [Burdine, 1952; Mualem, 1976] can be used to calculate the relative hydraulic conductivity,  $K_r$ , which is the ratio between the unsaturated,  $K$ , and the saturated,  $K_s$ , conductivities. This tight relationship between conductivity and matric potential has resulted in a wide use of water-retention curves that approach infinity at the residual water content,  $\theta_r$ , and that are not defined below this threshold. This unphysical behavior poses severe limitations to the ability of correctly modeling vapor dynamics [Ciocca *et al.*, 2013]. The few modifications proposed to better represent water-retention close and below residual water content [Campbell and Shiozawa, 1992; Rossi and Nimmo, 1994; Fayer and Simmons, 1995; Morel-Seytoux and Nimmo, 1999; Webb, 2000; Silva and Grifoll, 2007; Zhang, 2011], have been used only in few recent studies to simulate soil moisture dynamics [e.g., Silva and Grifoll, 2007; Sakai *et al.*, 2009; Smits *et al.*, 2012; Ciocca *et al.*, 2013; Tang and Riley, 2013] whereas standard water-retention curves that approach infinity at residual water content remain widely employed [see, e.g. Grifoll *et al.*, 2005; Mortensen *et al.*, 2006; Sakaki and Illangasekare, 2007; Bittelli *et al.*, 2008; Shokri *et al.*, 2008b, 2009a; Assouline *et al.*, 2010; Shokri and Salvucci, 2011; Smits *et al.*, 2011; Assouline, 2013; Campoy *et al.*, 2013; Mirus and Loague, 2013]. Ciocca *et al.* [2013] compared the standard and the modified water-retention curves by simulating the drying of soils columns in isothermal and steady atmospheric conditions, and found that the modified curves produced results more consistent with experimental evaporations in the moisture-limited regime. However, thermal effects together with variable atmospheric conditions affect the evaporation [Smits *et al.*, 2012] and, particularly at dry regimes, might have a significant impact. We investigate the effects of water-retention models on evaporation from moist to very dry soils, in presence of a strong diurnal atmospheric forcing and we compare the results with the isothermal case investigated by Ciocca *et al.* [2013].

### 4.2 Transport equations

Conservation of the total soil moisture (which includes both the liquid and the vapor component) and the energy are described by two coupled balance equations according to Milly [1982] (henceforth Milly); the main variables are the matric potential  $\psi$  (assumed negative in unsaturated soil) and the temperature  $T$ . Milly's equations refer to the pioneering theory by Philips and de Vries [1957] and de Vries [1958], (henceforth PdV), in which the main variables are the liquid soil moisture content  $\theta_L$  and  $T$ .



### 4.2.1 Liquid and vapor transport equation

We consider the total moisture flux:

$$\mathbf{j}_M = \mathbf{j}_L(\psi, T) + \mathbf{j}_V(\psi, T) \quad (4.1)$$

where

$$\mathbf{j}_L(\psi, T) = -\rho_L(T)K(\psi, T)\nabla(\psi + z), \quad (4.2)$$

represents a Darcian liquid flux, in which  $\rho_L$  is the liquid water density (temperature dependent),  $K$  is the hydraulic conductivity and  $z$  the vertical space coordinate (positive upwards);

$$\mathbf{j}_V(\psi, T) = -D_V(\psi, T)\nabla\rho_V(\psi, T), \quad (4.3)$$

$\mathbf{j}_V$  is the Fickian vapor flux,  $D_V(\psi, T)$  is the water-vapor molecular diffusivity in the unsaturated soil, and  $\rho_V(\psi, T)$  the water vapor density.

The adsorbed liquid flow due to thermal gradients introduced by *Kay and Groenevelt* [1974], since this term has little impact on the evaporation [see, e.g. *Milly*, 1984]. The vapor density is defined, according to the Kelvin equation [*Edlefsen and Anderson*, 1943],

$$\rho_V(\psi, T) = \rho_V^*(T)h = \rho_V(T)^* \exp(\psi g / R_V T), \quad (4.4)$$

which describes the local thermodynamic equilibrium between liquid and vapor phase. In Eq. 4.4,  $\rho_V^*$  is the saturation vapor density;  $h$  the relative humidity of water vapor in capillaries with respect to a flat liquid/vapor interface and varies between 0 and 1;  $R_V$  the gas constant for water vapor; and  $g$  the gravity acceleration. Expanding  $\nabla\rho_V$  in Eq. 4.3 in terms of  $\nabla\psi$  and  $\nabla T$  we obtain, after some manipulations:

$$\mathbf{j}_M(\psi, T) = -\rho_L \left[ (K + D_{\psi,V})\nabla\psi + D_{T,V}\nabla T + K\hat{z} \right], \quad (4.5)$$

where  $\hat{z}$  is the unit vector pointing upwards and  $D_{\psi,V}(\psi, T)$  and  $D_{T,V}(\psi, T)$  are the diffusion coefficients for water vapor driven by gradients of matric potential and temperature, respectively.

The total moisture balance equation is obtained by imposing the conservation of the total water mass in the soil, defined as  $\rho_L(T)\theta_L(\psi, T) + \rho_V(\psi, T)\theta_V(\psi, T)$ , where  $\theta_V(\psi, T) = \phi - \theta_L(\psi, T)$  is the volumetric vapor content, and  $\phi$  the soil porosity. Expanding in the primary variables and applying Eq. 4.5 we obtain:

$$\begin{aligned} & \left[ (\rho_L - \rho_V) \frac{\partial\theta_L}{\partial\psi} \Big|_T + \theta_V \frac{\partial\rho_V}{\partial\psi} \Big|_T \right] \frac{\partial\psi}{\partial t} \\ & + \left[ (\rho_L - \rho_V) \frac{\partial\theta_L}{\partial T} \Big|_\psi + \theta_V \frac{\partial\rho_V}{\partial T} \Big|_\psi \right] \frac{\partial T}{\partial t} \\ & = \nabla \cdot \rho_L \left[ (K + D_{\psi,V})\nabla\psi + D_{T,V}\nabla T \right] + \rho_L \frac{\partial K}{\partial z}. \end{aligned} \quad (4.6)$$

## Chapter 4. Retention Curves and Evaporation Part II: the Diurnal Atmospheric Forcing

The specific forms of the functions appearing in Eq. 4.6, along with the main values of the parameters employed are given in Appendix (Sec. 4.A.1).

### 4.2.2 Heat transport equation

Heat transport is described neglecting both the source term represented by the differential heat of wetting given by *Edlefsen and Anderson* [1943]; *de Vries* [1958]) and the advection of heat of wetting due to matric potential gradients. Therefore, the heat flux is:

$$\mathbf{j}_H = -\lambda(\psi, T)\nabla T + \rho_L(T)L(T)D_{\psi,V}(\psi, T)\nabla\psi + c_L(T - T_0)\mathbf{j}_M \quad (4.7)$$

where  $\lambda(\psi, T)$  represents the soil thermal conductivity, which varies with the amount of water in the soil,  $L(T)$  the latent heat of vaporization at temperature  $T$ ,  $c_L$  the specific heat of liquid water and  $T_0$  a reference temperature.

The stored energy,  $E_H$ , is:

$$E_H(\psi, T) = C(\psi, T)(T - T_0) + L_0\rho_V(\psi, T)\theta_V(\psi, T) \quad (4.8)$$

where  $C(\psi, T)$  is the soil volumetric heat capacity. Equating the energy accumulation,  $\partial_t E_H$ , expanded in the primary variables and net flux contribution,  $-\nabla \cdot \mathbf{j}_H$ , leads to the energy balance equation:

$$\begin{aligned} & \left[ C + L\theta_V \frac{\partial \rho_V}{\partial T} \Big|_{\psi} - \rho_V L \frac{\partial \theta_L}{\partial T} \Big|_{\psi} \right] \frac{\partial T}{\partial t} \\ & + \left[ L\theta_V \frac{\partial \rho_V}{\partial \psi} \Big|_T - \rho_V L \frac{\partial \theta_L}{\partial \psi} \Big|_T \right] \frac{\partial \psi}{\partial t} \\ & \nabla \cdot [\lambda \nabla T - L \mathbf{j}_V] - c_L \mathbf{j}_M \cdot \nabla T. \end{aligned} \quad (4.9)$$

The specific forms of the functions appearing in Eq. 4.9, along with the main values of the parameters employed are presented in Appendix (Sec. 4.A.2).

### 4.3 Water-retention curves and unsaturated hydraulic conductivity

To describe the dependence of the soil moisture content  $\theta_L$  on the matric potential  $\psi$ , which is crucial to evaporation, we use the classical retention model by *Van Genuchten* [1980] (hereafter VG), although our considerations can be applied to every retention model presenting similar features [see, e.g. *Brooks and Corey*, 1964; *Brutsaert*, 1966].

We also include the temperature-induced effects on water-retention investigated in many studies [see, e.g., *Philips and de Vries*, 1957; *Jury and Miller*, 1974; *Hopmans and Dane*, 1986; *Nimmo and Miller*, 1986; *Grant and Salehzadeh*, 1996]. We use the empirical correction proposed by *Grant and Salehzadeh* [1996], which introduces an empirical factor  $\beta_0 < 0$ . Therefore, the retention model is:

#### 4.4. Evaporation from soil columns with diurnal forcing

$$\theta_L(\psi, T) = \theta_r + (\phi - \theta_r) \left( \frac{1}{\left[ \alpha |\psi(T_0)| \left( \frac{\beta_0 + T_0 + 273.15\text{K}}{\beta_0 + T + 273.15\text{K}} \right) \right]^n + 1} \right)^{1-1/n} \quad (4.10)$$

where the parameters  $\alpha$  ( $\text{m}^{-1}$ ) and  $n > 1$  (-) are related to the inverse of the air-entry suction and to the pore size distribution, respectively, and  $\theta_r$  is the residual water content.

In this study, we assume  $\beta_0 = -766.45$  K which accounts only for the changes in interfacial tension of liquid water against its saturated vapor, as originally suggested by PdV [Grant and Salehzadeh, 1996].

We describe the relative unsaturated conductivity  $K_r$  adopting the standard Mualem-VanGenuchten model [Mualem, 1976]:

$$K_r(\psi) = \frac{(1 - (\alpha|\psi|)^{n-1} [1 + (\alpha|\psi|)^n]^{-m})^2}{[1 + (\alpha|\psi|)^n]^{m/2}} \quad (4.11)$$

where ( $m = 1 - 1/n$ ).

Eq. 3.1 shows that  $\theta_r$  is attainable only for  $\psi = -\infty$ , when the unsaturated conductivity becomes zero (Eq. 4.11) and  $\rho_V$  vanishes (Eq. 4.4).

VG model precludes the soil from drying below residual saturation due to the absence of both vapor and liquid fluxes. Retention models can be modified to avoid this issue and allow the soil to dry below residual saturation. Ciocca *et al.* [2013] investigated two possible modifications: one simply set  $\theta_r = 0$  whereas the other is the extension proposed by Webb [2000] to fit the Campbell and Shiozawa [1992] dataset. Both solutions showed similar effects on predictions of vapor dynamics. In this study, we present only the former extension, which always predicted larger vapor fluxes. Webb's model leads to similar results. We refer to this as the modified van Genuchten model (hereafter MVG), which differs from the classical VG due to the zero residual saturation and the pore-size distribution parameter,  $n_{\text{MVG}}$ , which is modified to guarantee the best overlap with the VG curve in the wet and intermediate region, where data are in general available and reliable. As in Ciocca *et al.* [2013], we refer to it as the Modified van Genuchten model (hereafter MVG). The MVG model differs from the classical VG for residual saturation set to zero and for the pore-size distributed parameter, which guarantees the best overlap with the VG curve in the wet and intermediate region, where data are in general more common and reliable. The hydraulic and thermal properties of the soil investigated are listed in Tab. 4.1 and the resulting VG and MVG retention curves are plotted in Fig. 4.1.

#### 4.4 Evaporation from soil columns with diurnal forcing

To investigate the effects of the retention models on moisture and energy dynamics, we simulate the evaporation from a column of height 0.1 m homogeneously packed with the loam

hydraulic properties <sup>a</sup>							thermal properties <sup>b,c</sup>		
$K_s$	$\alpha$	$n$	$\theta_r$	$\phi$	$\theta_L^*$	$n_{MVG}$	$b_1$	$b_2$	$b_3$
[m/s]	[1/m]	[-]	[-]	[-]	[-]	[-]	[W/m°C]	[W/m°C]	[W/m°C]
$2.89 \cdot 10^{-6}$	3.6	1.56	0.078	0.43	0.101	1.404	0.243	0.393	1.534

Table 4.1: Hydraulic and thermal parameters for the loam.

<sup>a</sup> Carsel and Parrish [1988].

<sup>b</sup> Chung and Horton [1987].

<sup>c</sup> Grant and Salehzadeh [1996].

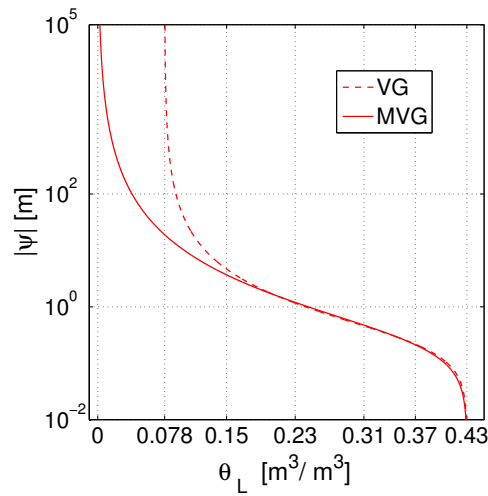


Figure 4.1: Plot of the matric potential-water content relationship,  $|\psi(\theta)|$ , for the soil used; the dashed curve corresponds to the standard van Genuchten model (VG); the solid curve is modified van Genuchten curves (MVG).

soil exposed to a diurnal atmospheric forcing at the surface. We compare the results with the isothermal evaporation which has been investigated by *Ciocca et al.* [2013].

We employ a modified version of the Matlab code used in *Lunati et al.* [2012] and *Ciocca et al.* [2013] to numerically solve the coupled system of Eq. 4.6 and Eq. 4.9 by a sequentially implicit finite volume scheme, on a one dimensional grid consisting of 100 equally-spaced cells of size 0.001 m. We assume an initial water content  $\theta_0 = 0.37$  and a soil and air temperature of  $25^\circ\text{C}$ ; and we impose a no-flux condition for water and heat at the bottom boundary.

After 4 days of relaxation (only the air temperature oscillates) to equilibrate with gravity, the soil surface is exposed to the diurnal forcing, which is described by an evaporative moisture flux  $E$  and a heat flux  $\mathbf{j}_H|_{z=0}$ . According to the aerodynamic diffusion relationships by *Anderson* [1976], the evaporative forcing  $E$  is:

$$\mathbf{j}_M|_{z=0} = E = \frac{k^2 U_{\text{air}} \gamma}{[\ln(z_a/z_0)]^2} (\rho_V|_{z=0} - \text{Ha}_{\text{air}}) \quad (4.12)$$

where  $z_0 = 0.001$  m is the surface roughness length,  $k = 0.4$  the von Karman's constant,  $\gamma = 1$  a stability factor,  $z_a = 2$  m the screen height in the atmosphere at which the wind speed  $U_{\text{air}}$ , kept constant at  $1 \text{ m s}^{-1}$  and the absolute air humidity  $\text{Ha}_{\text{air}}$  are assigned. The heat flux  $\mathbf{j}_H|_{z=0}$

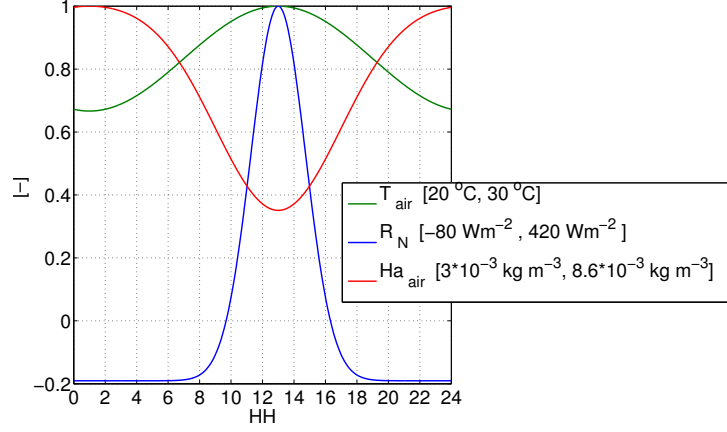


Figure 4.2: Periodic atmospheric variables normalized by the respective daily maxima. The squared brackets in the legend contain the minimum and the maximum assigned value for each variable.

results from the energy conservation at the soil-atmosphere interface, expressed as:

$$\mathbf{j}_H|_{z=0} = R_N - \rho_L [L + c_L(T|_{z=0} - T_0)] E - H, \quad (4.13)$$

where  $T|_{z=0}$  is the soil surface temperature (computed by the numerical model),  $R_N$  is the net radiation and  $H$  the turbulent diffusion of sensible heat into the atmosphere given by:

$$H = \frac{\rho_{\text{air}} c_{p,\text{air}} k^2 U_{\text{air}} \gamma}{[\ln(z_a/z_0)]^2} (T|_{z=0} - T_{\text{air}}), \quad (4.14)$$

where  $\rho_{\text{air}} c_{p,\text{air}} = 1.231 \cdot 10^3 \text{ J m}^{-3}$  is the volumetric heat capacity of air at constant pressure and  $T_{\text{air}}$  is the air temperature.

The diurnal fluctuations of  $\text{Ha}_{\text{air}}$ ,  $T_{\text{air}}$  and  $R_N$  are plotted in Fig. 4.2 (normalized by the respective daily maxima); the detailed parameterizations are described in Appendix (Sec. 4.A.3).

## 4.5 Results and discussion

As long as the water availability at the soil surface is sufficiently large, evaporation is dictated by the atmospheric demand and not by the soil moisture content. During this energy-limited regime [see, e.g., *Brutsaert*, 1982], evaporation occurs at the soil surface at the potential rate  $E_{\text{pot}}$ , which is defined by replacing the vapor density  $\rho_V$  by the saturated value  $\rho_V^*$  in Eq. 4.12. Drying follows the energy-limited regime for about 15 days, during which the cumulative mass loss predicted by both the VG and MVG curves decrease on average at a constant rate; small

diurnal oscillations induced by the atmospheric forcing are visible during the energy-limited regime (Fig. 4.3).

Compared to the isothermal case, the energy-limited regime is longer, but the evaporation rate is lower. This effect is introduced by the diurnal atmospheric forcing, and it is likely more imputable to the fluctuations of air humidity  $H_{\text{air}}$  and air temperature  $T_{\text{air}}$  than to the net radiation cycle, which is expected to increase the soil temperature during a daily fluctuation since the positive component is greater and lasts longer than the negative (Fig. 4.2); this induces larger  $\rho_V^*$  (Eq. 4.20) and therefore larger evaporation ratio than the isothermal case during the energy-limited regime. However, the total water mass that evaporates during the

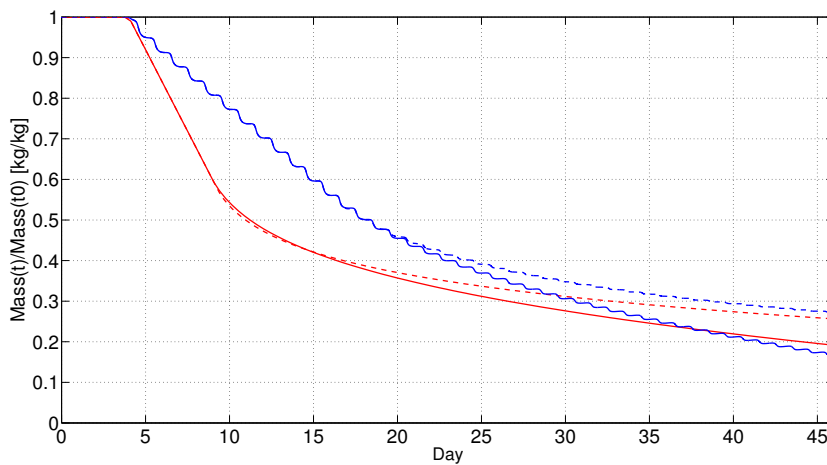


Figure 4.3: Plots of the normalized cumulative mass loss; the solid blue curve corresponds to the Modified van Genuchten model (MVG) and the dashed blue curve to the standard van Genuchten model (VG) for this study. The solid red curve corresponds to the Modified van Genuchten model (MVG) and the dashed blue curve to the standard van Genuchten model (VG) for the isothermal case [Ciocca *et al.*, 2013].

energy-limited regime in presence of diurnal forcing is  $\sim 20\%$  higher. Periodic fluctuations of moisture allow evaporation at the surface at the potential rate for a longer time (Fig. 4.3).

Approaching the moisture-limited regime, evaporation slows down and the differences between the two retention models become significant: the VG model predicts an earlier suppression of the evaporation, which results in a very limited cumulative mass loss after 30 days, when the water content in the whole column is about to reach residual saturation. In the same time period, the MVG model predicts a two times larger cumulative mass loss (Fig. 4.3).

Compared to the isothermal case, the moisture-limited regimes predicted by both models are characterized by larger and shorter evaporation rates. The MVG simulation exhibits a faster drying resulting in a crossover with the isothermal case at day 37 (Fig. 4.3), whereas the cumulative water removal predicted by the VG model is still lower than the isothermal case.

The quasi constant oscillations of potential evaporation observed during the energy-limited regime (Fig. 4.4) reflect small temperature variations at the soil surface. After onset of the

moisture-limited regime (day 18), the growth of  $E_{\text{pot}}$  predicted by both the VG and MVG models indicates that the surface temperature increases at daytime.

The increase of the maximum potential evaporation (at daily peak of solar radiation when drier conditions are reached) predicted by the MVG model becomes significantly larger, compared to the VG model (Fig. 4.4). Moreover, because of the larger drying at the soil surface allowed by the MVG model, slightly lower minima of potential evaporation are predicted at nighttime, indicating a larger surface cooling. The simulated evaporation  $E_{\text{sim}}$ , equal to the potential evaporation during the energy-limited regime, exhibit fast decays during the first days of moisture-limited regime (Fig. 4.4). During the moisture-limited regime, the evaporation predicted by MVG model at the maximum diurnal atmospheric forcing is more than three times larger than VG model (Fig. 4.5). The drying below residual saturation allowed by the MVG

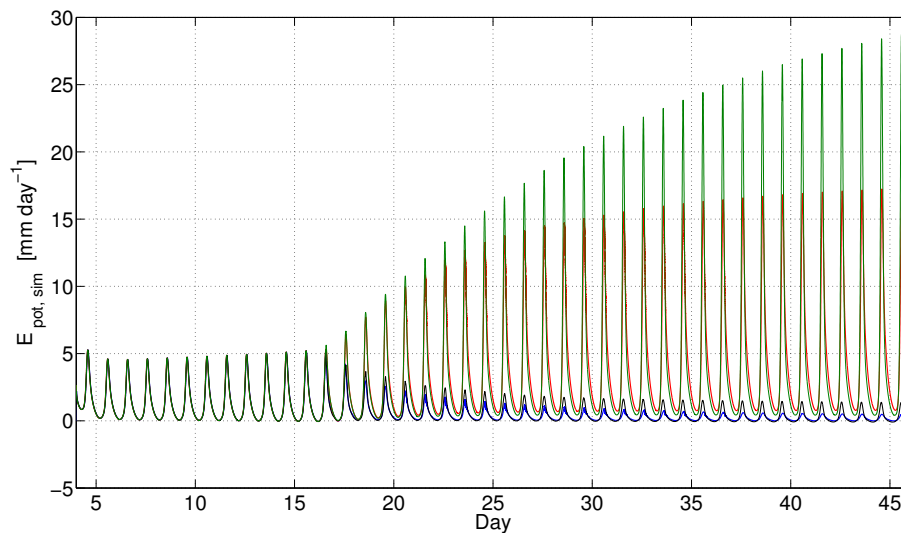


Figure 4.4: Plots of the simulated evaporation  $E_{\text{sim}}$  and of the potential evaporation  $E_{\text{pot}}$ ; the thick lines correspond to  $E_{\text{sim}}$  (blue) and  $E_{\text{pot}}$  (red) for the VG model; the thin lines correspond to  $E_{\text{sim}}$  (black) and  $E_{\text{pot}}$  (green) for the MVG model.

model has an important impact not only on the evaporation during the moisture-limited regime. The drier conditions predicted by the MVG model yield larger daily temperature fluctuations, which result in sensible heat fluxes 35% larger and ground heat fluxes larger by  $\sim 20\%$  at the daily peak of solar radiation, and more negative at nighttime (Fig. 4.5).

Although further investigations and accurate measurements are required, the implications of these results go certainly beyond laboratory or field soil dynamics and might have significant effects on numerical predictions at a variety of spatiotemporal scales.

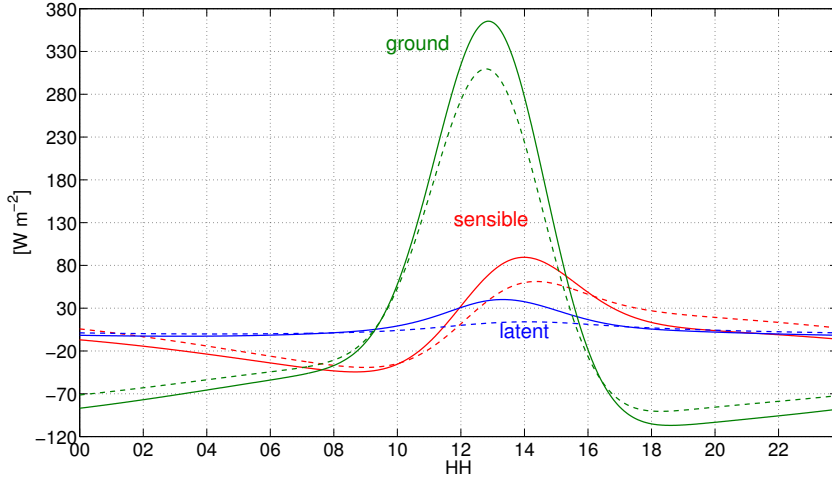


Figure 4.5: Plots of the simulated ground (green), latent (blue) and sensible (red) heat fluxes at day 45; the solid curves correspond to the MVG model; the dashed curves to the VG model.

## 4.A Appendixes: Parameterizations

### 4.A.1 Hydraulic Parameters

The unsaturated hydraulic conductivity  $K(\psi, T)$  is defined as:

$$K(\psi, T) = [\mu_L(T_0)/\mu_L(T)]K_r(\psi)K_{\text{sat}} \quad (\text{m s}^{-1}), \quad (4.15)$$

where  $K_{\text{sat}}$  is the saturated value. Temperature effects on  $K$  appear due to dependence of the kinematic viscosity  $\mu$  on  $T$ , which is parameterized as:

$$\mu_L(T) = e^{-c_1 - c_2/T + c_3/T^2} \quad (\text{Kg m}^{-1} \text{s}^{-1}), \quad (4.16)$$

with  $c_1 = 6.434$ ,  $c_2 = 2414 \text{ K}$ , and  $c_3 = 6.673 \cdot 10^5 \text{ K}^2$ .

The dependence of the relative hydraulic conductivity  $K_r$  on the matric potential, being related to the water-retention curves, is described in Sec. 4.3. The water-vapor molecular diffusivity in unsaturated soil is:

$$D_V(\psi, T) = \frac{(\phi - \theta_L(\psi, T))^{10/3}}{\phi^2} D_{V,m}(T), \quad (4.17)$$

where

$$D_{V,m}(T) = 2.12 \cdot 10^{-5} \left[ \frac{T}{273.15 \text{ K}} \right]^2 \quad (\text{m}^2 \text{s}^{-1}), \quad (4.18)$$



is the vapor diffusion coefficient in air;

$$\rho_L(T) = (d_1 + d_2 T - d_3 T^2) \quad (\text{Kg m}^{-3}) \quad \text{is the liquid density} \quad (4.19)$$

$$\rho_V^*(T) = \frac{a_0}{T} e^{a_1 - a_2/T - a_3 T} \quad (\text{Kg m}^{-3}) \quad \text{is the vapor density} \quad (4.20)$$

and  $d_1 = 658.2$ ,  $d_2 = 2.509 \text{ K}$ ,  $d_3 = 4.6 \cdot 10^{-3} \text{ K}^2$ ,  $a_0 = 10^{-3} \text{ Kg m}^3 \text{ K}$ ,  $a_1 = 31.3716$ ,  $a_2 = 6014.79 \text{ K}$ ,  $a_3 = 7.92495 \cdot 10^{-3} \text{ K}^{-1}$ .

The diffusion coefficients for water vapor  $D_{\psi,V}$  and  $D_{T,V}$  in Eq. 4.5 are obtained by expanding the vapor-density gradient (Eq. 4.4) in terms of  $\psi$  and  $T$ ; i.e.

$$\nabla \rho_V = \frac{g \rho_V}{R_V T} \nabla \psi + \left( h \frac{d \rho_V^*}{dT} - \frac{g \rho_V \psi}{R_V T^2} \right) \nabla T \quad (4.21)$$

( $R_V = 461.5 \text{ J Kg}^{-1} \text{ K}^{-1}$  and  $g = 9.81 \text{ m s}^{-2}$ ) which, inserted into Eq. 4.3 gives:

$$D_{T,V} = \eta D_V \left( h \frac{d \rho_V^*}{dT} - \frac{g \rho_V \psi}{R_V T^2} \right), \quad (4.22)$$

$$D_{\psi,V} = D_V \frac{g \rho_V}{R_V T}. \quad (4.23)$$

where  $\eta$  is an empirical factor that accounts for the enhancement of vapor flow due to temperature gradients [*Philips and de Vries*, 1957], assumed equal to one in this study.

#### 4.A.2 Thermal Parameters

We use the relation proposed by *Chung and Horton* [1987] to describe the soil thermal conductivity

$$\lambda(\psi, T) = b_1 + b_2 \theta_L(\psi, T) + b_3 \theta_L^{1/2}(\psi, T) \quad (\text{J m}^{-1} \text{ s}^{-1} \text{ K}^{-1}), \quad (4.24)$$

with the empirical parameters  $b_1$ ,  $b_2$  and  $b_3$  listed in Tab. 3.1. The volumetric heat capacity of the soil

$$C(\psi, T) = (1 - \phi) c_S \rho_S + c_L \rho_L(T) + c_P \rho_V(\psi, T) \theta_V(\psi, T) \quad (\text{J m}^{-3}) \quad (4.25)$$

accounts for the solid, liquid and gas contributions;  $c_S \rho_S = 1.92 \cdot 10^6 \text{ J m}^{-3}$  is the volumetric heat capacity of the solid matrix [*de Vries*, 1963],  $c_L = 4182 \text{ J Kg}^{-1} \text{ K}^{-1}$ ,  $c_P = 1005 \text{ J Kg}^{-1} \text{ K}^{-1}$  the specific heat of water vapor at constant pressure and

$$L(T) = L_0 - (c_L - c_P)(T - T_0) \quad (\text{J Kg}^{-1}), \quad (4.26)$$

(with  $L_0 = 2.453 \cdot 10^6 \text{ J Kg}^{-1}$ ) the latent heat of vaporization at  $T_0 = 25^\circ \text{C}$ .

**4.A.3 Atmospheric forcing parameterizations**

The absolute air humidity is

$$Ha_{\text{air}} = \frac{p_V}{T_{\text{air}} R_V} \quad (\text{Kg m}^{-3}), \quad (4.27)$$

where the vapor pressure  $p_V$  is

$$p_V = Hr_{\text{air}} p_V^* \quad (\text{mbar}), \quad (4.28)$$

$p_V^*$  is the saturated vapor pressure (from WMO CIMO guide 2008<sup>1</sup>)

$$p_V^* = 6.112 \exp\left(\frac{17.62(T_{\text{air}} - 273.15)}{243.12 + (T_{\text{air}} - 273.15)}\right) \quad (\text{mbar}), \quad (4.29)$$

and

$$Hr_{\text{air}} = \overline{Hr} + A_{Hr} \cos\left[2\pi\left(\frac{t - t_{\text{max,Hr}}}{24}\right)\right], \quad (4.30)$$

$$T_{\text{air}} = \overline{T_{\text{air}}} + A_{T_{\text{air}}} \cos\left[2\pi\left(\frac{t - t_{\text{max,T}}}{24}\right)\right], \quad (4.31)$$

are the air relative humidity and the air temperature, respectively.

$Hr_{\text{air}}$  oscillates around a mean value  $\overline{Hr} = 0.3$  with fluctuations of semi-amplitude  $A_{Hr} = 0.2$ ; the diurnal peak of  $Hr_{\text{air}}$  occurs at  $t_{\text{max,Hr}} = 1$  AM, in correspondence with the minimum of air temperature, as often measured [see, e.g. *Assouline et al.*, 2010].

$T_{\text{air}}$  oscillates daily around a mean value  $\overline{T_{\text{air}}} = 25^\circ\text{C}$  by  $\pm A_{T_{\text{air}}} = 5^\circ\text{C}$ .

Finally, we assign the net radiation as a Morlet's wavelet:

$$R_N = -R_{N,N} + A_{R_N} \exp(-((t - t_{\text{max,R}_N})^2)/6) \cos((t - t_{\text{max,R}_N}/256)), \quad (4.32)$$

which is lowered in the negative region by a quantity  $R_{N,N} = 80 \text{ W m}^{-2}$  to simulate a constant radiative cooling at nighttime. The amplitude of  $R_N$  is  $A_{R_N} = 500 \text{ W m}^{-2}$  with the peak occurring at  $t_{\text{max,R}_N} \equiv t_{\text{max,T}} = 1$  PM (Fig. 4.2).

<sup>1</sup> <http://www.wmo.int/pages/prog/www/IMOP/publications/CIMO-Guide/Ed2008Up2010/Part-I/WMO8Ed2008partICh4Up2010en.pdf>

# Bibliography

- Anderson, E. A. (1976), A point energy and mass balance model of a snow cover, *Tech. Rep. Tech. Rep NWS-19*, NOAA, Silver Spring, Md.
- Assouline, S., K. Narkis, S. W. Tyler, I. Lunati, M. B. Parlange, and J. S. Selker (2010), On the diurnal soil water content dynamics during evaporation using dielectric methods, *Vadose Zone J.*, 9, 709–718.
- Brooks, R. H., and A. T. Corey (1964), Hydraulic properties of porous media, *Hydrology Paper No. 3*, Colorado State Univ.
- Brutsaert, W. H. (1966), Probability laws of pore-size distributions, *Soil Sci.*, 101, 85–91.
- Campbell, G. S., and S. Shiozawa (1992), Prediction of hydraulic properties of soils using particle size distribution and bulk density data, international Workshop on Indirect Methods for Estimating the Hydraulic Properties of Unsaturated Soils, 1992.
- Carsel, R. F., and R. S. Parrish (1988), Developing joint probability distributions of soil water retention characteristics, *Water Resour. Res.*, 24(5), 755–769.
- Chung, S. O., and R. Horton (1987), Soil heat and water flow with a partial surface mulch, *Water Resour. Res.*, 23(12), 2175–2186.
- Ciocca, E., Lunati, I. and M. B. Parlange (2013), Effects of the water-retention curve on evaporation from dry soils, *Internal report*.
- de Vries, D. A. (1958), Simultaneous transfer of heat and moisture in porous media, *Trans. Am. Geophys. Union*, 39(5), 909–916.
- de Vries, D. A. (1963), *The thermal properties of soils - in Physics of Plant Environment*, 210-235 pp., North-Holland.
- Edlefsen, N. E., and A. B. C. Anderson (1943), Thermodynamics of soil moisture, *Hilgardia*, 15, 31–298.
- Fayer, M. J., and C. S. Simmons (1995), Modified soil water retention functions for all matric suctions, *Water Resour. Res.*, 31(5), 1233–1238.

## Bibliography

---

- Grant, S. A. and A. Salehzadeh (1996), Calculation of temperature effects on wetting coefficients of porous solids and their capillary pressure functions, *Water Resour. Res.*, 32(2), 261–270.
- Hopmans, J. W. and J. H. Dane (1986), Temperature dependence of soil water retention curves, *Soil Sci. Soc. Amer. J.*, 50(3), 562–567.
- Jury, W. A. and E. E. Miller (1974), Measurement of the transport coefficients for coupled flow of heat and moisture in a medium sand *Soil Sci. Soc. Amer. Proc.*, 38, 551–557.
- Kay, B. D., and P. H. Groenevelt (1974), On the interaction of water and heat transfer in frozen and unfrozen soils: I. Basic theory: The vapor phase. *Soil Sci. Soc. Amer. Proc.*, 38, 395–400.
- Lebeau, M., and J. Konrad (2010), A new capillary and thin film flow model for predicting the hydraulic conductivity of unsaturated porous media., *Water Resour. Res.*, 46, W12554.
- Lunati, I., F. Ciocca, and M. B. Parlange (2012), On the use of spatially discrete data to compute energy and mass balance., *Water Resour. Res.*, 48, W05542.
- Milly, P. C. D. (1982), Moisture and heat transport in hysteretic, inhomogeneous porous media: a matric head-based formulation and a numerical model, *Water Resour. Res.*, 18(3), 489–498.
- Milly, P. C. D. (1984), A simulation analysis of thermal effects on evaporations from soil, *Water Resour. Res.*, 20(8), 1087–1098.
- Mualem, Y. (1976), A new model for predicting the hydraulic conductivity of unsaturated porous media, *Water Resour. Res.*, 12(3), 513–522.
- Nimmo, J. R. and E. E. Miller (1986), The temperature dependence of isothermal moisture vs. potential characteristics of soils, *Soil Sci. Soc. Amer. J.*, 50(3), 1105–1113.
- Peters, A., and W. Durner (2008), A simple model for describing hydraulic conductivity in unsaturated porous media accounting for film and capillary flow, *Water Resour. Res.*, 44, W11417.
- Philips, J. R., and D. A. de Vries (1957), Moisture movements in porous materials under temperature gradients, *Transaction of American Geophysical Union*.
- Ross, P. J., J. Williams, and K. L. Bristow (1991), Equations for extending water-retention curves to dryness, *Soil Sci. Soc. Am. J.*, 55, 923–927.
- Rossi, C., and J. R. Nimmo (1994), Modeling of soil water retention from saturation to oven dryness, *Water Resour. Res.*, 30(3), 701–708.
- Saito, H., J. Simunek, and B. P. Mohanty (2006), Numerical analysis of coupled water, vapor and heat transport in the vadose zone, *Vadose Zone J.*, 5, 784–800, doi:10.1029/2010WR009866.
- Sakai, M., S. B. Jones, and M. Tuller (2011), Numerical evaluation of subsurface soil water evaporation derived from sensible heat balance, *Water Resour. Res.*, 47, W02547, doi:10.1029/2010WR009866.

- Seneviratne, S., T. Corti, E. Davin, J. E. Hirschi, M., I. Lehner, B. Orlowsky, and A. Teuling (2010), Investigating soil moisture-climate interactions in a changing climate: A review, *Earth-Science Rev.*, 99, 125–161, doi:10.
- Smits, K. M., V. V. Ngo, A. Cihan, T. Sakaki, and T. H. Illangasekare (2012), An evaluation of models of bare soil evaporation formulated with different land surface boundary conditions and assumptions, *Water Resour. Res.*, 48(12).
- Tokunaga, T. K. (2009), Hydraulic properties of adsorbed water films in unsaturated porous media., *Water Resour. Res.*, 45, W06415.
- Tuller, M., and D. Or (2001), Hydraulic conductivity of variably saturated porous media: Film and corner flow in angular pore space, *Water Resour. Res.*, 37, 1257–1276.
- Van Genuchten, M. T. (1980), A closed-form equation for predicting the hydraulic conductivity of unsaturated soils, *Soil Sci. Soc. Amer. J.*, 44, 892–898.
- Webb, S. W. (2000), A simple extension of two-phase characteristic curves to include the dry region, *Water Resour. Res.*, 36(6), 1425–1430.
- Zhang, Z. F. (2011), Soil water retention and relative permeability for conditions from oven-dry to full saturation, *Vadose Zone J.*, 10, 1299–1308.



## 5 Multi Functional Heat Pulse Probes for Planar Heat Flux Measurements: a Laboratory Experiment

**Abstract:** *Ground heat flux is difficult to measure precisely. Soil heat flux plates are unreliable due to perturbation of heat and water flux field's induced by their presence.*

*Measurements obtained using tri-needles heat pulse probes are more reliable but also restricted along one direction and they cannot account for changes in flux orientation and needles misalignment, which may bias ground heat flux measurements.*

*Penta-needles multi functional heat pulse probes (MFHPPs) allow partially overcoming these problems as they provide 2D information. We investigate the ability of MFHPPs to measure controlled two-dimensional heat fluxes, generated across an oven-dried coarse sand layer packed in a special cylindrical chamber. The sand is heated at the bottom by an aluminum disk screwed on top of a standard kitchen hot plate supplied by stabilized DC. MFHPPs measurements without insulation of the vertical wall, which allows a radial (horizontal) dispersive heat flux component, are matched with numerical simulations realized by using temperatures from thermocouples placed within the sand to assign optimized boundary conditions. The largest deviations are 13 % in magnitude and 11.6 % in direction.*

*This demonstrates that the penta-needles structure of the MFHPPs allows a better heat flux estimation than previous methods thanks to information along the orthogonal direction.*

*With few adjustments at the needles structure a 3D scan would be achievable. By improving the estimation of the incoming heat flux within the soil the comparison between simulations and experiment during transient regimes will be possible.*

## **5.1 Introduction**

Ground heat flux ( $G$ ) is crucial in the surface energy balance. For years the lack of closure of the surface balance equations was attributed to errors associated with the eddy covariance measurements of latent and sensible heat fluxes *Mauder and Foken* [2006] (or the spatial variability *Mauder et al.* [2010], or the advection *Aubinet et al.* [2010]). Recently, *Lunati et al.* [2012] and *Higgins* [2012] showed how discrete and inaccurate measurements of  $G$  may be responsible for almost the entire energy residual variance of the surface energy budget in field measurements.

$G$  at the soil surface is commonly estimated with the combination method [*Fuchs and Tanner*, 1968; *Fuchs*, 1986] which accounts for a time averaged heat flux measured across a vertical soil layer at known depth plus a correction for heat storage change in the soil between this layer and the surface.

Assuming  $dz$  the thickness of the vertical soil layer,  $G$  is described by the mono-dimensional Fourier's conduction law:

$$G = -\lambda_s(dT/dz) \quad (\text{W m}^{-2}) \quad (5.1)$$

where  $\lambda_s$  is the soil thermal conductivity ( $\text{W m}^{-1} \text{K}^{-1}$ ) and  $dT/dz$  the vertical temperature gradient ( $\text{K m}^{-1}$ ).

The soil heat flux plates (HFP) are the most common probes used for measuring  $G$ . They are built of thermopile sensors embedded in a resin disk of known thermal conductivity  $\lambda_{\text{hfp}}$ . However, unless  $\lambda_s = \lambda_{\text{hfp}}$ , the heat flux field will be distorted across the plates, which deteriorate the accuracy of the measurements. Suggested analytical corrections [see, e.g., *Philips*, 1961] for the heat flux deflections induced by the HFP are generally ignored because they are complex and require additional measurements. The self-calibrating HFP are able to generate a heat pulse of known power to correct the deflection error; they have a large diameter ( $\approx 8$  cm) and require a high power supply which is not always available on the field.

Moreover, proper installation ensuring good contact soil-plate is generally difficult and condensation may occur on the plates surfaces [*Fuchs*, 1986] because the transport of both heat and water is physically prevented across the HFP. *Cobos and Baker* [2003] showed that HFP underestimate  $G$  particularly in coarse soils whereas three-needles heat-pulse probes led to more accurate results because they allow measuring in situ both  $\lambda_s$  and vertical temperature gradients between the outer needles.

Heated-needle techniques have been developing for years. *Campbell et al.* [1991] proposed the dual-probe heat-pulse method to estimate soil thermal properties and soil water content obtaining successful results in both laboratory [e.g. *Bristow et al.*, 1994b] and field measurements [e.g. *Tarara and Ham*, 1997; *Heitman et al.*, 2003], and further developments allowed soil volumetric heat capacity [*Bristow*, 1998] and electrical conductivity measurements.

Numerical and experimental investigations of the ability of heat-pulse needle-probes have been mainly addressed toward Darcy water flux quantification [*Ren et al.*, 2000; *Mori et al.*, 2003, 2005; *Kamai et al.*, 2008], solute transport *Mortensen et al.* [2006] and subsurface evaporation estimate *Heitman et al.* [2008a,b]; *Sakai et al.* [2011]; *Xiao et al.* [2011], whereas much



less attention has been dedicated to heat fluxes.

*Cobos and Baker* [2003] compared the HFP and the three-needles heat pulse probes in a special chamber (see *Watts et al.* [1990]) where vertical heat fluxes across the soil were generated. The intensity of the heat fluxes, used as reference values in the comparison, was calculated subtracting from the electrical power supplied the heat loss at the bottom and the sides. However, they provided a little information about the effectiveness of the chamber insulation and the induced temperature field. Furthermore, the analysis performed to calculate the heat loss revealed sensible side loss which questions the mono-dimensionality of the generated fluxes.

Due to the inability of the three-needle probes to detect and correct for a rotation of the needles and/or of the heat flux, questions about the performance of the three-needle probes and their applicability on the field may be raised.

We investigate the ability of penta-needle MFHPPs, e.g., [*Mori et al.*, 2003, 2005; *Mortensen et al.*, 2006] (described in Sec. 5.2) to quantify two dimensional heat fluxes generated in the needle plane. A special apparatus (described in Sec. 5.3) is built and two MFHPPs (MFHPP 1 and MFHPP 2 in Fig. 5.2, respectively) are placed at different heights in 0.1 m of oven-dried medium-textured sand.

The setup allows capturing both horizontal (radial) and vertical heat flux components and inferring the real magnitude and direction of the heat flux. The measurements are compared with numerical simulations which are used as references. The temperatures obtained from thermocouples are employed to numerically reproduce the temperature field and the heat fluxes at steady-state through a novel minimization process (see Sec. 5.4). The main advantage of this approach is that precise information about the thickness and the thermal properties of the materials surrounding the sand is not needed.

## 5.2 MFHPP Theory

MFHPPs (Fig. 5.1) are designed to monitor in situ the coupled heat, water and solute transport. They measure temperatures and apply inverse modeling techniques to instantaneously infer soil thermal properties (heat capacity, heat diffusivity and from them the heat flux density), moisture content and solute transport properties (solute concentration and dispersion) within the same soil volume.

MFHPPs replace multiple probes and avoid issues such as: different footprints and soil volumes, invasive multiple installations, mutual interactions among the probes. A MFHPP consists of six needle sensor placed in cross pattern; four along one direction and the remaining two in the orthogonal direction. The needle at the intersection of the two orthogonal directions (Fig. 5.1.A) is a heater which sends transient heat pulses whereas the other needles consist of thermistors, with thermocouples installed at the tip of the shortest needles (5 and 6 in Fig. 5.1.A,C) and in the middle of the longest (3 and 1 in Fig. 5.1.A,B). The needle 4 (Fig. 5.1.A) is part of the Wenner array used to measure solute concentration in the soil water; it is not

## Chapter 5. Multi Functional Heat Pulse Probes for Planar Heat Flux Measurements: a Laboratory Experiment

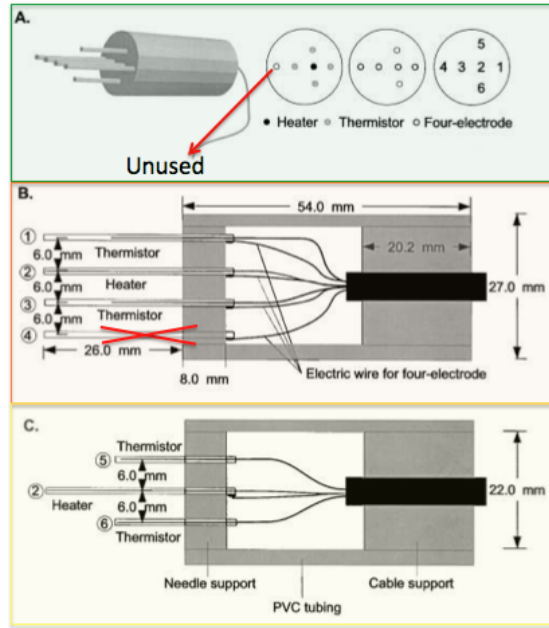


Figure 5.1: Schematic of the MFHPP (adapted from *Mori et al.* [2003]) including: (A) MFHPP body and the needles displacement; (B) the view from the side; (C) the view from the top.

employed in this study, in which we use only a penta-needle array (1,2,3,5,6, in Fig. 5.1.A). A detailed description of the MFHPPs is given by *Mori et al.* [2003]. The needle is approximated as an infinite line source of negligible thickness and the soil is assumed homogeneous and isotropic. Analytically, for a heat pulse of duration  $t_0$  (s) and energy per unit time and length  $q'$  ( $\text{J m}^{-1} \text{s}^{-1}$ ), the temperature variations  $\Delta T$  ( $^{\circ}\text{C}$ ) at a certain time  $t$  (s) and radial distance  $x$  (m) from the heater

$$\Delta T(x, t) = \frac{q'}{4\pi C\kappa} \left[ Ei\left(\frac{-x^2}{4\kappa(t-t_0)}\right) - Ei\left(\frac{-x^2}{4\kappa t}\right) \right], \quad (5.2)$$

where  $C$  and  $\kappa$  are the volumetric heat capacity ( $\text{J m}^{-3} \text{K}^{-1}$ ) and the heat diffusivity ( $\text{m}^2 \text{s}^{-1}$ ), respectively, and  $Ei(y)$  is the exponential integral function with argument  $y$  [*Abramowitz and Stegun*, 1964]. Temperatures variations recorded at the four thermistors surrounding the heater are fitted to Eq. 5.2 optimizing the unknown parameters  $C$  and  $\kappa$  by least square errors method.  $t_0$ ,  $q'$  and the perpendicular distances between the thermistors and the heater  $x$  are provided.  $x$  is manufactured at 6 mm (Fig. 5.1.B,C) however small deflections from this value are not unusual.

Before the experiments, an accurate thermistor-heater distance was obtained by measuring with the MFHPPs in an agar solution of known thermal properties,  $C$  and  $\kappa$  (set as known parameters in Eq. 5.2), and by fitting  $r$ . The resulting  $r$  were all in the range between 5.81 mm and 5.95 mm.

The soil thermal conductivity  $\lambda_s$  by the MFHPPs is calculated from the ratio of fitted  $C$  and  $\kappa$ .

By using the temperature measurements of the thermistors needles, magnitude and direction of the heat flux vector  $\vec{G}$  on the plane perpendicular to the needles is inferred from the vectorial sum of Eq. 5.1 along the two orthogonal directions:

$$\vec{G} = -\lambda_s \left( \frac{\partial T}{\partial z} \hat{z} + \frac{\partial T}{\partial r} \hat{r} \right) \quad (\text{W m}^{-2}) \quad (5.3)$$

where  $r$  and  $z$  are the radial (horizontal) and vertical coordinates of unit vectors  $\hat{r}$  and  $\hat{z}$ , respectively.

### 5.3 Experimental Set-up and Measurements

The experimental setup consists of a PVC cylinder (height = 0.4 m, inner width = 0.19 m, wall thickness = 0.01 m, thermal conductivity =  $0.19 \text{ W K}^{-1} \text{ m}^{-1}$ ) placed on a standard kitchen heat plate which serves as heat source. Stabilized DC current is supply by an adjustable laboratory power generator (Elind 50HS 6.4D, 300 W power, 0÷50 V, 0÷6.4 A, LL Trading, Italy). A Pt-100 thermal probe ( $\pm 0.01^\circ\text{C}$ ) is placed on the semi-circular heat coil underneath the heat plate to accurately measure the source temperature.

The side and the bottom of the plate are insulated using polystyrene. An aluminum disk (thickness = 0.03 m, thermal conductivity  $\approx 140 \text{ W K}^{-1} \text{ m}^{-1}$ ) is placed at the bottom of the cylinder over the heat plate to create a homogenous surface temperature at the bottom of the soil. To reduce the contact resistances between the heat plate and the aluminum disk and between the disk and the soil, a thermally conductive silica gel [Electrolube HTSP, thermal conductivity  $\approx 3 \text{ W K}^{-1} \text{ m}^{-1}$ ] is applied.

The heat plate is screwed at the bottom of the aluminum disk to improve both the contact and heat conduction. The temperature on the horizontal face at the bottom of the soil is measured by five type T (Copper-Constantan) twisted wire thermocouples [Omega Newport, UK] with soldered tips have been stuck on both horizontal faces by using thermally conductive resin [Rapid Epoxy resin, Araldite, Switzerland], carefully checking for only the tips to be in contact with the aluminum.

Temperature fluctuations between the thermocouples stuck on the aluminum disk are  $\pm 0.3^\circ\text{C}$ , which proves the homogeneity of the heat supply.

The PVC cylinder can be thermally insulated on the external side by applying a polystyrene cube of edge = 0.5 m (Fig. 5.2); in this study the insulation is intentionally not applied to permit horizontal heat dissipation.

The soil column is instrumented with thermocouples and two MFHPPs (Fig. 5.2). The soil used is a coarse quartz sand [Carlo Bernasconi SA, Switzerland] with a bulk density  $\rho_b = 1.58 \text{ Kg m}^{-3}$ , dried in the oven before being homogeneously packed within the chamber. Three arrays, each consisting of three thermocouples stuck at 0.025 m, 0.05 m and 0.075 m along a fiber glass plate (very poor thermal conductor) are vertically placed within the sand to monitor the temperature; two arrays are attached to the inner wall of the chamber along a diameter and the third is placed at the center of the column (Fig. 5.2).

## Chapter 5. Multi Functional Heat Pulse Probes for Planar Heat Flux Measurements: a Laboratory Experiment

Two MFHPPs are buried into the sand at different heights and distances from the center of the column, in a position ensuring two thermistors horizontally placed along the radial direction and two along the vertical direction; the probes are placed such that they lie on the diameter connecting the three thermocouple arrays.

On top of the sand a stainless steel lid (thickness = 0.1 m, thermal conductivity =  $16 \text{ W K}^{-1} \text{ m}^{-1}$ ) is placed to ensure a homogeneous heat distribution (Fig. 5.2). Five thermocouples are stuck at the bottom of the lid to measure the temperature. All thermocouples are connected to a solid state multiplexer [model AM25T, Campbell Scientific]; the temperature is recorded every minute.

Temperature measurements of the two MFHPPs are regulated by a multiplexer [model AM16/32B, Campbell Scientific]. The heat pulses, each of the duration of eight seconds and sent once every one hour are regulated by a multichannel switch [model SDM-CD16AC AC/DC controller, Campbell Scientific].

The thermistors of the MFHPPs measure every second from ten seconds before the heat pulse and until 180 seconds after. All the multiplexers and the switch are controlled by a datalogger [model CR1000, Campbell Scientific], which also regulates the instantaneous data acquisition on a PC. The experiments are conducted in a laboratory where temperature is kept constant at  $20.5 \pm 0.4^\circ \text{C}$ . The experiment is conducted by applying to the heat plate an electrical power of

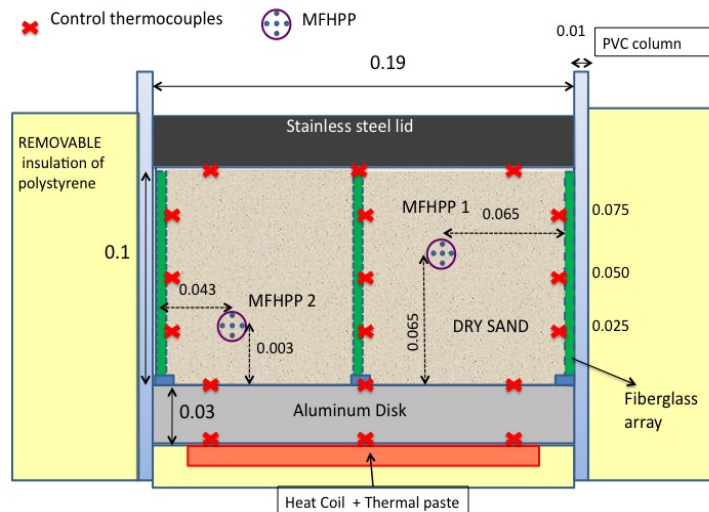


Figure 5.2: Sketch of the front side of the 2D heat flux chamber with cylindrical geometry. The numbers without units refer to distances in meters; the control thermocouples are used as boundary conditions for the simulations. The distances from the bottom of the soil and the inner wall of the chamber of the MFHPP 1 (shallower) and MFHPP 2 (deeper) are referred to the heater needle.

6.45 W (15 V at 0.43 A). Measurements with the MFHPPs are performed after two days from the beginning of the heating, when the steady-state is attained, and are repeated for one day.

## 5.4 Analysis

Numerical simulations are used to interpolate temperature measurements from the control thermocouples within the chamber and reproduce the soil temperature field. We use the heat equation in cylindrical coordinates:

$$\rho C \frac{\partial T}{\partial t} - \frac{1}{r} \frac{\partial}{\partial r} \left( \lambda_s r \frac{\partial T}{\partial r} \right) - \frac{1}{r^2} \frac{\partial}{\partial \theta} \left( \lambda_s \frac{\partial T}{\partial \theta} \right) - \frac{\partial}{\partial z} \left( \lambda_s \frac{\partial T}{\partial z} \right) = Q \quad (5.4)$$

where  $\theta$  represents the azimuthal angle and  $Q$  a source term.

In a homogeneous soil at the steady-state, assuming axial symmetry and the absence of internal heat sources/sinks, the first and the third term on the left hand side and the right hand side disappear, respectively, and Eq. 5.4 reduces, after simple manipulations, to

$$\frac{\partial}{\partial r} \left( \lambda_s r \left( \frac{\partial T}{\partial r} + \frac{\partial T}{\partial z} \right) \right) + \frac{\partial}{\partial z} \left( \lambda_s r \left( \frac{\partial T}{\partial r} + \frac{\partial T}{\partial z} \right) \right) = 0. \quad (5.5)$$

Eq. 5.5 is the form of the heat equation considered in this study. Being the generated planar temperature fields symmetric around the center of the column, we define the computational domain as  $r \in [0, R]$ ,  $z \in [0, H]$ , where  $R$  and  $H$  are the radius and height of the column respectively and  $r$  and  $z$  the horizontal and vertical coordinates. At the bottom we assign the temperature obtained by averaging the readings of the five thermocouples stuck on the aluminum disk at the soil bottom along the entire radius  $R$ . At the lateral surface  $[0, z]$  corresponding to the center of the column we assign a zero flux condition due to symmetry along the whole height, whereas at the external lateral surface  $[R, z]$  (in contact with the PVC) we assign a Neumann boundary condition based on Eq. 5.1:

$$\left( \lambda_s \left( \frac{\partial T}{\partial r} \hat{r} + \frac{\partial T}{\partial z} \hat{z} \right) \right) \vec{n}_r = \left[ \frac{\lambda}{Z} \right]_{\text{side}} (T_{\text{amb}} - T_{\text{side}}) \quad (5.6)$$

and at the top boundary  $[r, H]$

$$\left( \lambda_s \left( \frac{\partial T}{\partial r} \hat{r} + \frac{\partial T}{\partial z} \hat{z} \right) \right) \vec{n}_z = \left[ \frac{\lambda}{Z} \right]_{\text{top}} (T_{\text{amb}} - T_{\text{top}}) \quad (5.7)$$

where  $\vec{n}_r$  and  $\vec{n}_z$  are the unity vectors perpendicular to the external lateral surface and to the top, respectively, and oriented outward;  $T_{\text{amb}}$  is the laboratory temperature and the suffixes side and top refer to the external lateral and the upper boundary, respectively.

$T_{\text{side}}$  are computed based on the temperatures measured by the thermocouples placed in the vertical arrays (close to the inner wall of the chamber and in the center of the soil column), whereas  $T_{\text{top}}$  is computed based on the temperatures by the thermocouples stuck on the stainless steel lid on top of the sand.

The gap between measured and simulated temperatures is minimized by fitting (using the least squares method) an effective ratio of thermal conductivity and thicknesses of the lateral

## Chapter 5. Multi Functional Heat Pulse Probes for Planar Heat Flux Measurements: a Laboratory Experiment

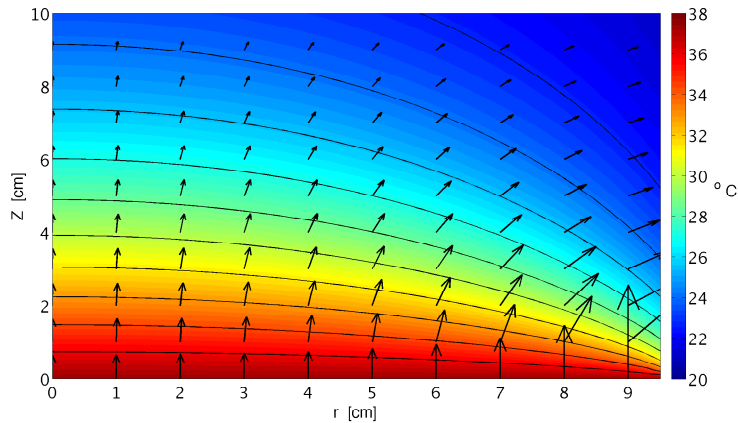


Figure 5.3: 2D simulated temperature field at the steady-state. The arrows indicate magnitude and direction of the temperature gradients, whereas the solid black lines are isotherms.

layer(s) of the chamber (Eq. 5.6) and another effective ration for the top layer(s) of the chamber (Eq. 5.7) . This approach prevents from requiring knowledge of the thermal and geometrical properties of the layer(s) surrounding the soil. However, it does not allow a direct fit of the soil thermal conductivity  $\lambda_s$ .

Since an independent measure of the thermal conductivity of the sand (e.g. by calorimetry) is not provided by the supplier, we calculate  $\lambda_s$  used in the numerical simulations by the empirical relation from *Johansen* [1975]:

$$\lambda_s = \frac{0.135\rho_b + 64.7}{2700 - 0.947\rho_b}. \quad (5.8)$$

$\lambda_s$  values calculated and measured by the MFHPPs are listed in Tab. 5.1. To solve Eq. (5.5) with the described boundary conditions the finite element solver *pdetool* of Matlab is used on a triangular unstructured mesh of 2353 nodes (4544 triangles). The solution of nodes of the triangular mesh is then interpolated onto a cartesian grid of regular mesh which allows simulating values corresponding exactly to the needles position.

### 5.5 Results and Discussion

An applied electrical power of 6.45 W produces average vertical temperature gradient of about  $2^\circ\text{C}/\text{cm}$  at the steady-state (Fig. 5.3). Gradients are steeper in the first centimeters above the heat source, characterized by a large lateral dissipation. The range of temperatures (between  $20^\circ\text{C}$  and  $38^\circ\text{C}$ ) is commonly experienced in shallow dry bare soils exposed to the sun.

Isotherms are almost horizontal and parallels in the center, but they are bent close to the wall of the chamber and horizontal dissipation cannot be neglected (Fig. 5.4). We find good agreement between the simulation and the temperatures measured by the MFHPPs along the

horizontal direction, in particular for the MFHPP 2 (closer to the bottom and further from the center) whereas the measurements by the MFHPP 1 are slightly overestimated (underestimated) closer to (further from) the center by the numerical simulation.

The temperatures shown in Fig. 5.4 are averaged over one day of steady-state; the associated small error bars, indicating the standard deviations, reveal the absence of perturbations of the heat flow within the chamber. Steady-state conditions are confirmed by the constant values of  $\lambda_s$  measured by the MFHPPs (Tab. 5.1), which display negligible variability over one day at steady-state conditions. Moreover, the measured values of  $\lambda_s$  agree very good with the values calculated from Eq. 5.8 and employed in the simulation.

This proves the reliability of the MFHPPs in estimating thermal properties. Fig. 5.5 compares measured and simulated heat fluxes. The heat flux direction measured by the MFHPP 2 is tilted with respect to the vertical by  $\sim 19^\circ$  and this agrees with the results of the simulations ( $\sigma_{\phi_G} = -1.6\%$ ). The measured magnitude  $|G|$  differs from the simulated by 13%. The agreement for the MFHPP 1 is less good for the direction,  $+9.8^\circ$  ( $\sigma_{\phi_G} = +11.6\%$ ) but better for the magnitude ( $\sigma_{|G|} = -8.3\%$ ). However, the comparisons are within an acceptable range of

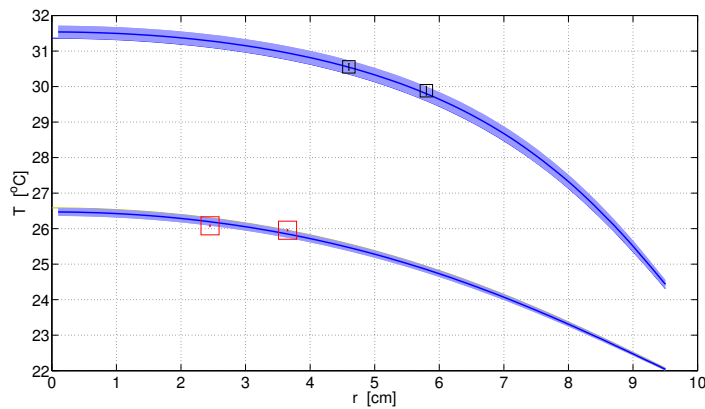


Figure 5.4: Comparison between the one-day averaged temperature measured at the steady-state by the MFHPP 1 (red squared dots) and the MFHPP 2 (black squared dots), and the simulations (solid lines) along the radial direction. The error bars represent the standard deviations of the temperature measurements. The shaded purple bands show the simulated temperatures at  $\pm 0.001$  m from the vertical position of the needles.

agreement accounting for all the difficulties presented by this study and the MFHPPs are able to capture the main features of the heat flux generated across the soil.

The restriction to the analysis at the steady-state might be overcome by replacing the aluminum disk with another of a material less thermally conductive (e.g. stainless steel) which allows to estimate the heat flux crossing it and flowing into the soil. This heat flux could be therefore assigned as Neumann boundary condition at the bottom, extending the investigation to the transient phases of heating/cooling, so common in presence of diurnal cycle.

In this first study, the two effective parameters in Eq. 5.6 (lateral) and Eq. 5.7 (top) are fitted with six and one (averaged) point measurements, respectively; increasing the number of

## Chapter 5. Multi Functional Heat Pulse Probes for Planar Heat Flux Measurements: a Laboratory Experiment

	$ G $ [W m <sup>-3</sup> ]	$\phi_G$ [°]	$\sigma_{ G }$ [%]	$\sigma_{\phi_G}$ [%]	$\lambda_s$ [W m <sup>-1</sup> K <sup>-1</sup> ]
MFHPP 1	23.75	84.09	-8.3	+11.6	0.227
Simulated	25.90	74.33			0.231
MFHPP 2	41.48	71.33	-13.0	-1.6	0.223
Simulated	47.10	72.51			0.231

Table 5.1: Measured and simulated magnitude  $|G|$  and direction (with respect to the horizontal)  $\phi_G$ , with the relative difference in percent  $\sigma_{|G|}$  and  $\sigma_{\phi_G}$ .  $\lambda_s$  are the thermal conductivities of the oven-dried sand measured by the MFHPPs (averaged over one day of steady-state) and calculated using Eq. 5.8. The signs – and + refer to underestimation and overestimation of the simulated value, respectively.

points (e.g. by using arrays with more thermocouples in the center and at the inner wall of the chamber) will generate more reliable references.

The MFHPPs reveal their potential in accurately measuring both magnitude and direction of heat fluxes that are not vertical. The presence of two additional thermistors in the orthogonal direction (with respect to the tri-needle probes used by *Cobos and Baker* [2003]) is of crucial importance to check for the effective direction of the heat flux and eventually correct an imperfect alignment of the needles along the direction of the flux, if this is known.

With the current displacement of the thermocouples within the thermistors, these check and corrections, impossible for *Cobos and Baker* [2003], are allowed over planes perpendicular to the needles. Slightly modifying the position of two of the four thermocouples (e.g. moving those of needles 1 and 3 in Fig. 5.1 from the middle to the tip of the needles), it would be possible to scan all the three main orthogonal directions. Moreover, by adding a thermistor in the same needle of the heater would allow to calculate the fluxes using a better linearization than with only two points, therefore reducing the possible error of discretization (see *Lunati et al.* [2012]). Although tests with different powers supply and different soils (also wet) should be performed to finally validate both the goodness of the measurements and the approach used to check their accuracy, these results already reveal how the MFHPPs may definitely contribute to overcome the issues related to reliable estimates of  $\vec{G}$ , crucial component of the surface energy budget.



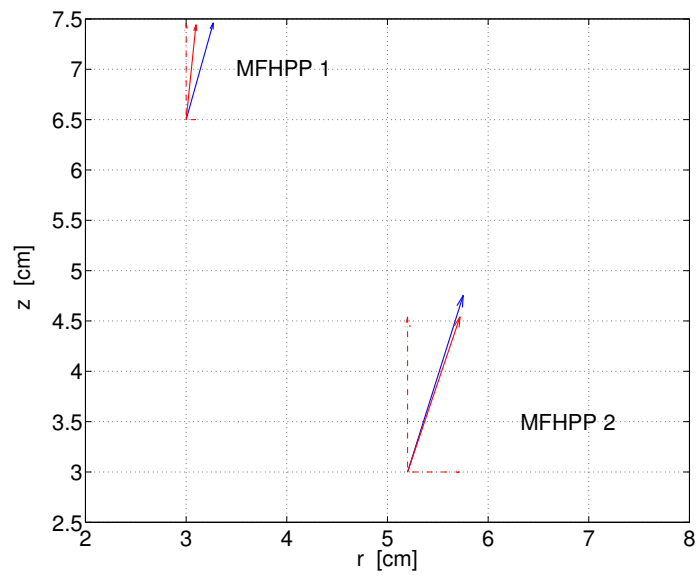


Figure 5.5: Heat fluxes measured by the MFHPP 1 and MFHPP 2 (solid red arrows) with the corresponding horizontal and vertical components (red dot-dashed arrows), compared with the simulated heat fluxes (blue solid arrows). Magnitudes and directions of the solid arrows are listed in Tab. 5.1.



# Bibliography

- Abramowitz, M., and I. A. Stegun (1964), *Handbook of mathematical functions with formulas, graphs and mathematical tables*, Dover Publications, USA.
- Aubinet, M., et al. (2010), Direct advection measurements do not help to solve the night-time CO<sub>2</sub> closure problem - evidence from three inherently different forests., *Agric. Forest Meteorol.*, 150(5), 651–654, doi:10.1016/j.agrformet.2010.01.016.
- Bristow, K. L. (1998), Measurement of thermal properties and water content of unsaturated sandy soil using dual-probe heat-pulse probes, *Agric. For. Meteorol.*, 89, 75–84.
- Bristow, K. L., R. D. White, and G. J. Kluitenberg (1994b), Comparison of single and dual probes for measuring soil thermal properties with transient heating, *Aust. J. Soil. Res.*, 32, 447–464.
- Campbell, G. S., K. Calissendorf, and H. J. Williams (1991), Probe for measuring soil specific heat using heat-pulse method., *Soil Sci. Soc. Am. J.*, 55, 291–293.
- Ciocca, F., I. Lunati, N. Van de Giesen, and M. B. Parlange (2012), Heated optical fiber for distributed soil-moisture measurements: a lysimeter experiment, *Vadose Zone J., Special Edition*, doi:10.2136/vzj2011.0199.
- Cobos, D. R., and J. M. Baker (2003), In situ measurements of soil heat flux with the gradient method, *Vadose Zone J.*, 2, 589–594.
- Fuchs, M. (1986), *Heat flux. Methods of soil analysis: Part 1 - Physical and mineralogical methods*, 957-968 pp., SSSA Book Ser. 5. 2nd ed. ASA and SSSA., Madison, WI.
- Fuchs, M., and C. B. Tanner (1968), Calibration and field test of soil heat flux plates, pp. 326–320, *soil Sci. Soc. Am. Proc.*
- Heitman, J., R. Horton, T. J. Sauer, and T. M. DeSutter (2008a), Sensible heat observations reveal soil water evaporation dynamics, *J. Hydrometeorol.*, 9, 165–171, doi:10.1175/2007JHM963.1.
- Heitman, J. L., J. M. Basinger, G. J. Kluitenberg, J. M. Ham, J. M. Frank, and P. L. Barnes (2003), Field evaluation of the dual-probe heat-pulse method for measuring soil water content, *Vadose Zone J.*, 2, 552–560.

## Bibliography

---

- Heitman, J. L., X. Xiao, R. Horton, and T. J. Sauer (2008b), Sensible heat measurements indicating depth and magnitude of subsurface soil water evaporation, *Water Resour. Res.*, *44*, W00D05, doi:10.1029/2008WR006961.
- Higgins, C. W. (2012), A-posteriori analysis of surface energy budget closure to determine missed energy pathways, *Geophys. Res. Lett.*, *39*, L19,403.
- Johansen, O. (1975), Thermal conductivity of soils, Ph.D. thesis, Norwegian Univ. of Science and Technol., Trondheim, (CRREL draft transl. 637, 1977).
- Kamai, T., A. Tuli, G. J. Kluitenberg, and J. W. Hopmans (2008), Soil water flux density measurements near 1 cm d<sup>-1</sup> using an improved heat pulse probe design, *Water Resour. Res.*, *44*, W00D14, doi:10.1029/2008WR007036.
- Lunati, I., F. Ciocca, and M. B. Parlange (2012), On the use of spatially discrete data to compute energy and mass balance., *Water Resour. Res.*, *48*, W05542.
- Mauder, M., and T. Foken (2006), Impact of post-field data processing on eddy covariance flux estimates and energy balance closure, *Meteorol. Z.*, *15*(6), 597–609, doi:10.1127/0941-2948/2006/0167.
- Mauder, M., R. L. Desjardins, E. Pattey, and D. Worth (2010), An attempt to close the daytime surface energy balance using spatially-averaged flux measurements, *Boundary Layer Meteorol.*, *136*(2), 175–191, doi:10.1007/s10546-010-9497-9.
- Mori, Y., J. W. Hopmans, A. P. Mortensen, and G. J. Kluitenberg (2003), Multi-functional heat pulse probe for the simultaneous measurement of soil water content, solute concentration, and heat transport parameters, *Vadose Zone J.*, *2*, 561–571.
- Mori, Y., J. W. Hopmans, A. P. Mortensen, and G. J. Kluitenberg (2005), Estimation of vadose zone water flux from multi-functional heat pulse probe measurements, *Soil Sci. Soc. Am. J.*, *69*, 599–606, doi:10.2136/sssaj2004.0174.
- Mortensen, A. P., J. W. Hopmans, Y. Mori, and J. Simunek (2006), Multi-functional heat pulse probe measurements of coupled vadose zone flow and transport, *Adv. Water Res.*, *29*, 250–267.
- Philips, J. R. (1961), The theory of heat flux meters., *J. Geophys. Res.*, *66*, 571–579.
- Ren, T., G. J. Kluitenberg, and R. Horton (2000), Determining soil water flux and pore water velocity by a heat pulse technique, *Soil Sci. Soc. Am. J.*, *64*(2), 552–560.
- Sakai, M., S. B. Jones, and M. Tuller (2011), Numerical evaluation of subsurface soil water evaporation derived from sensible heat balance, *Water Resour. Res.*, *47*, W02547, doi:10.1029/2010WR009866.
- Tarara, J. M., and J. M. Ham (1997), Measuring soil water content in the laboratory and field with dual-probe heat-capacity sensors., *Agron. J.*, *89*, 535–542.

Watts, D. B., E. T. Kanemasu, and C. B. Tanner (1990), Modified heat-meter method for determining soil heat flux., *Agric. For. Meteorol.*, 49, 311–330.

Xiao, X., R. Horton, T. J. Sauer, J. L. Heitman, and T. Ren (2011), Cumulative soil water evaporation as a function of depth and time, *Vadose Zone J.*, 10, 1016–1022, doi: 10.2136/vzj2010.0070.



## **6 Heated Optical Fiber for Distributed Soil-Moisture Measurements: A Lysimeter Experiment**

This chapter was previously published with the following citation:

Ciocca, F, Lunati, I., Van de Giesen, N., Parlange, M.B., 2012:  
Heated Optical Fiber for Distributed Soil-Moisture Measurements: a Lysimeter Experiment.  
*Vadose Zone J.*, doi:10.2136/vzj2011.0199.

Francesco Ciocca\*  
Ivan Lunati  
Nick Van de Giesen  
Marc B. Parlange



An Actively Heated Fiber Optics method is tested to estimate soil moisture profiles along 30 meters of fiber optic cable buried in a large coil in a lysimeter variably saturated with depth. A comparison with independent soil moisture measurements shows an excellent matching in wet soil, while a significant underestimation occurs in dry conditions.

F. Ciocca, School of Architecture, Civil and Environmental Engineering, EPF, Lausanne, Switzerland; I. Lunati, Institute of Geophysics, Univ. of Lausanne, Switzerland; N. Van de Giesen, Faculty of Civil Engineering and Geosciences, TU Delft, Netherlands; M.B. Parlange, School of Architecture, Civil and Environmental Engineering, EPF, Lausanne, Switzerland. \*Corresponding author (francesco.ciocca@epfl.ch).

Vadose Zone J.  
doi:10.2136/vzj2011.0199  
Received 20 Dec. 2011.  
Open Access Article

© Soil Science Society of America  
5585 Guilford Rd., Madison, WI 53711 USA.  
All rights reserved. No part of this periodical may be reproduced or transmitted in any form or by any means, electronic or mechanical, including photocopying, recording, or any information storage and retrieval system, without permission in writing from the publisher.

## Heated Optical Fiber for Distributed Soil-Moisture Measurements: A Lysimeter Experiment

An Actively Heated Fiber Optics (AHFO) method to estimate soil moisture is tested and the analysis technique improved on. The measurements were performed in a lysimeter uniformly packed with loam soil with variable water content profiles. In the first meter of the soil profile, 30 m of fiber optic cable were installed in a 12 loops coil. The metal sheath armoring the fiber cable was used as an electrical resistance heater to generate a heat pulse, and the soil response was monitored with a Distributed Temperature Sensing (DTS) system. We study the cooling following three continuous heat pulses of 120 s at  $36 \text{ W m}^{-1}$  by means of long-time approximation of radial heat conduction. The soil volumetric water contents were then inferred from the estimated thermal conductivities through a specifically calibrated model relating thermal conductivity and volumetric water content. To use the pre-asymptotic data we employed a time correction that allowed the volumetric water content to be estimated with a precision of  $0.01\text{--}0.035 \text{ (m}^3 \text{ m}^{-3}\text{)}$ . A comparison of the AHFO measurements with soil-moisture measurements obtained with calibrated capacitance-based probes gave good agreement for wetter soils [discrepancy between the two methods was less than  $0.04 \text{ (m}^3 \text{ m}^{-3}\text{)}$ ]. In the shallow drier soils, the AHFO method underestimated the volumetric water content due to the longer time required for the temperature increment to become asymptotic in less thermally conductive media [discrepancy between the two methods was larger than  $0.1 \text{ (m}^3 \text{ m}^{-3}\text{)}$ ]. The present work suggests that future applications of the AHFO method should include longer heat pulses, that longer heating and cooling events are analyzed, and, temperature increments ideally be measured with higher frequency.

Abbreviations: AHFO, Active Heated Fiber Optics method; CB, capacitance-based; DTS, distributed temperature sensing;  $I_{AS}$ , Anti-Stokes intensity;  $I_S$ , Stokes intensity; TDR, time domain reflectometry.

**In recent years**, optical fiber distributed temperature sensing (DTS) based on Raman scattering has been increasingly employed in environmental monitoring (e.g., Selker et al., 2006a; Selker et al., 2006b; Westhoff et al., 2007; Freifeld et al., 2008; Tyler et al., 2008, 2009; Vercauteren et al., 2011; Keller et al., 2011). DTS has proven accurate to measure temperature along the entire fiber optic cable (whose length can exceed 30,000 m), affording a spatial resolution of 1 m and temporal frequencies greater than one measurement per minute.

DTS has also been used to estimate distributed thermal properties from the response to the diurnal temperature cycle (Steele-Dunne et al., 2010). Despite the attractive simplicity of DTS, which only requires the burial of the cable, the application is limited to conditions where there is a sensitive response to the diurnal cycle (e.g., sunny days, top bare soil, etc.). To overcome these limitations, variants have been proposed in which DTS is used to monitor the soil response to active heating of the metal sheath that protects the optical fiber (Active Heated Fiber Optics method, AHFO). This method has been used to track groundwater water movement (e.g., Perzmaier et al., 2004, 2006; Aufleger et al., 2005) and to measure soil moisture, where it has proven successful in distinguishing between dry, wet, and saturated soils (Weiss, 2003; Perzmaier et al., 2004, 2006). This application of AHFO potentially offers an alternative to more established techniques to measure soil moisture such as capacitance-based (CB) probes (see, e.g., Nadler and Lapid, 1996; Mohamed et al., 1997; Seyfried and Murdock, 2001, 2004) or Time Domain Reflectometry (TDR) (see, e.g., Topp et al., 1980; Campbell, 1990; Topp et al., 2000; Robinson et al., 2003; Jones and Or, 2004; Seyfried and Murdock, 2004; Assouline et al., 2010). A review of the state-of-the-art of soil moisture measurement techniques was presented by Hopmans et al. (1999) and Robinson et al. (2008).

Weiss (2003) showed that it is possible to infer the water content from the soil-temperature response to active heating. The thermal properties of the soil were obtained through the



classical probe method, which is based on an asymptotic analysis of the thermal response (see, e.g., Carslaw and Jaeger, 1959; deVries and Peck, 1958), and the water content was inferred using a calibration equation. However, the method was unable to detect changes of soil moisture below 6%.

More recently, Sayde et al. (2010) proposed a different approach which requires, in addition to DTS, independent measurements of water content. They obtained an empirical calibration curve by fitting the temperature increase as a function of the measured water content and suggested that this procedure might lead to more accurate water-content estimates by avoiding the use and consequent inversion of thermal properties.

However, the calibration curve depends heavily on the soil type and on the experimental setup (e.g., pulse duration and specific characteristic of the fiber optic cable), and lacks a clear physical relationship between the coefficients and the physical parameters.

In this study, we test the AHFO technique using a large vertical coil installed within a lysimeter filled with loamy soil and we measure the spatial variability of the soil moisture. Similar to Weiss (2003), we apply the cylindrical probe method (see, e.g., Carslaw and Jaeger, 1959; deVries and Peck, 1958) to analyze the temperature evolution and estimate the thermal conductivity along the cable. To improve the estimate of the thermal properties, we introduce a time correction (Van der Held and Van Drunen, 1949; deVries, 1952; Shiozawa and Campbell, 1990; Bristow et al., 1994) that allows reducing the duration of the heat pulse and the consequent possible perturbation of the water content. The volumetric water content is obtained by inverting the thermal conductivity model of Lu et al. (2007), with parameters specifically calibrated for our soil. The results were compared with independent soil moisture measurements made with capacitance sensors installed at several depths in the lysimeter.

## Theoretical Background Raman Backscattering and DTS Measurements

When a pulsed laser beam propagates through a fiber optic cable, a portion of the photons are backscattered and collected by a photodetector that quantifies their intensity and the elapsed time between emission and detection. Any inhomogeneity of the optical fiber causes backscattering; in addition to the cable end and possible ruptures of the cable, impurities and density fluctuations contribute to the return signal measured by the photodetector. In all of these cases photons are usually backscattered at wavelength equal to wavelength of the incident laser beam ( $\lambda_o = 1064$  nm in our case). This elastic scattering is referred to as Rayleigh (elastic) backscatter and involves the largest portion of the energy of the returning light.

In addition to the elastic backscattering, a less intense, inelastic backscattering occurs in the optical fiber, which is associated with the Raman effect and produces return signals of a different wavelength

than the incident beam. The signal characterized by a wavelength  $\lambda_s > \lambda_o$  is called the Stokes component, whereas the signal with wavelength  $\lambda_A < \lambda_o$  is called the Anti-Stokes component. The ratio between the intensity of these two components (equally spaced from  $\lambda_o$ ) depends on the temperature. While Stokes backscattering is generated by silica molecules that are in the vibrational ground state, Anti-Stokes backscattering requires the molecule to be in a vibrational excited state and, therefore, increases with the thermal excitation. The ratio between the intensities of Anti-Stokes ( $I_{AS}$ ) and Stokes ( $I_S$ ) components depends exponentially on the temperature,  $T$  [i.e.,  $I_{AS}/I_S \sim \exp(-\Delta E/k_B T)$ , where  $\Delta E$  is the energy shift from the Rayleigh peak and  $k_B$  the Boltzmann constant]. Therefore, the temperature can be inferred from the relative intensity of the Anti-Stokes to Stokes components.

A sufficient number of photons have to be collected to obtain a satisfactory signal-to-noise ratio and thus accurate temperature measurements. This determines the minimum time over which photons have to be collected and the maximum spatial resolution achievable by DTS. Usually, the lower limit to guarantee a good signal/noise ratio is on the order of 1 m (e.g., Weiss, 2003; Sayde et al., 2010), which is the distance over which the temperature is averaged in DTS measurements. We refer to Gratton and Meggitt (2000), Selker et al. (2006a, 2006b), and Tyler et al. (2009) for more details about the physical principle of DTS.

## Estimation of Thermal Properties by the Probe Method

If an accurate technique to measure temperature is available, the thermal properties of the soil can be inferred from the temperature response to heating. In AHFO, the fiber optic cable is used both as a temperature sensor (exploiting the dependence of the Raman scattering on temperature) and as a heat source by generating an electric current in the metal sheath that protects the fiber.

The problem of a line heat source in a homogeneous medium is well known and has given origin to the probe method to measure the thermal conductivity of soil (see, e.g., Carslaw and Jaeger, 1959; deVries and Peck, 1958). The simplest approximation is to consider the cable as an infinitely long line source of infinitesimal radius Carslaw and Jaeger (1959), deVries and Peck (1958), Shiozawa and Campbell (1990), Bristow et al. (1994).

Analytical solutions also exist for the more realistic case of a cylindrical heat source covered by an insulating sheath and buried in a homogeneous isotropic medium (Carslaw and Jaeger, 1959). We will regard the cylindrical heat source of external radius  $a$  (m) as a perfect conductor of thermal capacity per unit cable length  $S$  ( $J m^{-1} K^{-1}$ ) and we will assume that the insulation has negligible thermal capacity and thermal resistance per unit cable length  $R$  ( $K W^{-1} m^{-1}$ ); the properties of the soil surrounding the cable are the thermal conductivity  $\lambda$  ( $W m^{-1} K^{-1}$ ), the volumetric heat capacity  $C$  ( $J m^{-3} K^{-1}$ ), and the thermal diffusivity  $K = \lambda/C$  ( $m^2 s^{-1}$ ).

Assuming a constant heat source of strength  $Q$  ( $\text{W m}^{-1}$ ) per unit cable length, the temperature increment with respect to the initial temperature is (Carslaw and Jaeger, 1959)

$$\Delta T(t) = T(t) - T(0) = \frac{Q}{\lambda} G(b, \beta, \tau), \quad [1]$$

where  $t$  is the elapsed time since the heating started,

$$b = 2\pi R\lambda, \quad [2]$$

$$\beta = 2\pi a^2 C/S, \quad [3]$$

$$\tau = Kt/a^2, \quad [4]$$

and

$$G(b, \beta, \tau) = \frac{2\beta^2}{\pi^3 C} \int_0^\infty \frac{1 - \exp(-u^2 \tau)}{u^3 \Delta_1(b, \beta, u)} du, \quad [5]$$

with

$$\Delta_1(b, \beta, u) = [uJ_0(u) - (\beta - bu^2)J_1(u)]^2 + [uY_0(u) - (\beta - bu^2)Y_1(u)]^2, \quad [6]$$

where  $J_n(u)$  and  $Y_n(u)$  are the Bessel functions of order  $n$  of the first and second kind, respectively. For  $\tau \gg 1$ , Eq. [1] can be written as,

$$\Delta T(t) = \frac{Q}{4\pi\lambda} \left[ 2b + \ln \frac{4\tau}{c} - \frac{(4b-3)}{2\beta\tau} + \frac{\beta-2}{2\beta\tau} \ln \frac{4\tau}{c} + \dots \right] \quad [7]$$

where  $c = 1.7811 = \exp \gamma$ , and  $\gamma = 0.5772\dots$  is the Euler-Mascheroni constant. At the lowest order in  $\tau$  and after some simple manipulations, we obtain

$$\Delta T(t) = \frac{Q}{4\pi\lambda} \left[ \ln(t) + 2b + \ln \left( \frac{4K}{a^2 c} \right) \right], \quad [8]$$

which shows that the temperature increment depends logarithmically on time when  $t \gg a^2/K$  and that the effects of the insulating sheath do not affect the proportionality constant,  $Q/4\pi\lambda$ , which depends only on the heat source and on the thermal conductivity of the medium. Analogously to the classical Cooper-Jacob method for pumping-test interpretation (see, e.g., Bear, 1979), Eq. [8] allows estimating the thermal conductivity of the soil from the slope of the linear regression between the temperature increments,  $\Delta T$ , and the logarithm of time,  $\ln(t)$ . Once the thermal conductivity has been estimated, the thermal diffusivity  $K$  can be obtained from the intercept of the linear regression if  $b$  and  $a$  are known; and from the diffusivity one can calculate the volumetric heat capacity,  $C$ . For a heat source of finite duration  $\Delta t_h$ , the problem can be divided into a heating phase,  $0 < t < \Delta t_h$ , in which the

solution is again given by Eq. [1], and a cooling phase,  $t > \Delta t_h$ , in which the temperature increase can be written as a superposition of two solutions, one with positive and the other with a negative heat source, i.e.,

$$\Delta T(t) = \frac{Q}{\lambda} [G(b, \beta, \tau) - G(b, \beta, \tau - \Delta\tau_h)], \quad [9]$$

where  $\Delta\tau_h = K\Delta t_h / a^2$  is the dimensionless heating time. The second term in Eq. [9] represents an imaginary cooling, which is necessary to obtain a zero heat source term after heating ceases. At later time,  $t \gg (a^2/K) + \Delta t_h$ ,  $G(b, \beta, \tau)$  and  $G(b, \beta, \tau - \Delta\tau_h)$  can be asymptotically expanded for large  $\tau$  and  $\tau - \Delta\tau_h$ , respectively, which yields, at lowest order and after some manipulations,

$$\Delta T(t) = \frac{Q}{4\pi\lambda} \ln \left( \frac{t}{t - \Delta t_h} \right). \quad [10]$$

Equation [10] shows that the long-time analysis of the cooling phase allows the estimation of the thermal conductivity from the slope of the linear regression between  $\Delta T$  and  $\ln[t/(t - \Delta t_h)]$ . The first neglected term is

$$\frac{Q}{4\pi\lambda} \Delta\tau \left[ \frac{(4b-2)}{2\beta\tau^2} - \frac{\beta-2}{2\beta\tau^2} \ln \frac{4\tau}{c} \right]$$

which is proportional to  $1/\tau^2$  and approaches zero faster than the first neglected term in Eq. [8], which is proportional to  $1/\tau$  (see Eq. [7]). This indicates that the solution for the cooling approaches the asymptotic limit (Eq. [10]) more rapidly than the heating solution. We observe that this analysis does not allow estimating the heat capacity. If Eq. [8] and [10] are applied to pre-asymptotic data, the probe method leads to a systematic underestimation of the thermal conductivity (see, e.g., Bristow et al., 1994). Van der Held and Van Drunen (1949) have proven that this issue can be reduced by adding a time correction,  $t_0$ , to the argument of  $\ln(t)$  in Eq. [8] which reduces the difference with the exact solution, Eq. [1], and allows improving the estimate of the thermal properties from non-asymptotic measurements. deVries (1952) applied a similar strategy to analyze data from a cooling event and added a time correction,  $t_0$ , in Eq. [10] obtaining

$$\Delta T(t) = \frac{Q}{4\pi\lambda} \ln \left( \frac{t + t_0}{t - \Delta t_h + t_0} \right). \quad [11]$$

Once  $t_0$  is determined, the thermal conductivity can be inferred from the slope of the linear regression between  $\Delta T$  and  $\ln[(t + t_0)/(t - \Delta t_h + t_0)]$ .

## Estimation of the Water Content from the Thermal Conductivity

With the probe method presented in the previous section we have at our disposal two strategies to estimate the thermal conductivity from

the temperature response of the soil: one is based on the analysis of the heating phase and allows, in principle, also the estimation of the volumetric heat capacity; the other is based on the analysis of the cooling phase. As both the thermal conductivity and the volumetric heat capacity of the soil depend on the soil moisture, it is possible to infer the water content from the estimated thermal properties when reliable constitutive relationships are available. Despite the advantages of retrieving the soil moisture from the volumetric heat capacity (Bristow et al., 1993), an accurate estimate requires knowledge of the inner cable radius and of the thermal resistance of the insulator, and a sufficiently long heating time, which might perturb the soil state by providing a large amount of energy. More fundamentally, the exponential dependence of the heat capacity on the intercept of the linear regression requires an unrealistically precise estimate of the intercept to obtain reliable volumetric heat capacity. For these reasons, we concentrate on the use of the thermal conductivity to infer the water content.

Several constitutive relationships to describe the dependence of  $\lambda$  on the volumetric water content (from now on also indicated with  $\theta$ ) exist (see, e.g., Johansen, 1975; Chung and Horton, 1987; Côté and Konrad, 2005; Lu et al., 2007; Jougnot and Revil, 2010). Here we employ the model from (Lu et al., 2007) (Fig. 1) that expresses the thermal conductivity of moist soil as

$$\lambda = (\lambda_{\text{sat}} - \lambda_{\text{dry}})Ke + \lambda_{\text{dry}}, \quad [12]$$

where  $\lambda_{\text{dry}}$  and  $\lambda_{\text{sat}}$  are the thermal conductivities of the dry and saturated soil, respectively:

$$K_e = \exp \left\{ \alpha \left[ 1 - \left( \frac{\theta}{\theta_{\text{sat}}} \right)^{(\alpha-1.33)} \right] \right\}, \quad [13]$$

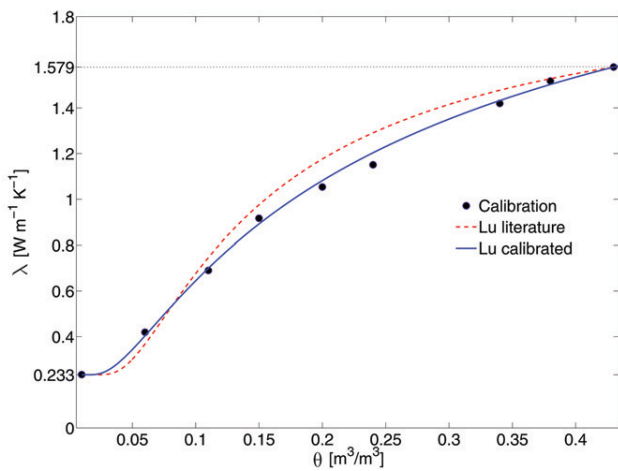


Fig. 1. Thermal conductivity ( $\lambda$ ) as a function of the volumetric water content ( $\theta$ ) according to model from Lu et al. (2007). The black dots represent the points acquired in laboratory using the Multi-Function Heat Pulse Probes. The blue dashed line is the curve with the standard value  $\alpha$  from Lu et al. (2007) for fine soils. The solid line is the best fit of the black dots, with parameter  $\alpha_{\text{Fit}}$ . The values of  $\theta_{\text{sat}}$ ,  $\theta_{\text{res}}$ ,  $\lambda_{\text{sat}}$ ,  $\lambda_{\text{dry}}$ ,  $\alpha$ , and  $\alpha_{\text{Fit}}$  are listed in Table 1.

is the Kersten number (Johansen, 1975);  $\theta_{\text{sat}}$  the saturated volumetric water content; and  $\alpha$  a parameter that depends on the soil texture.

## Error Analysis

Inferring  $\theta$  from the temperature response to heating involves two steps: the first requires the estimation of  $\lambda$  from the analysis of the temperature increment as a function of time; the second requires the use of constitutive relationships linking  $\lambda$  to  $\theta$ . To assess the accuracy of the measurements it is important to quantify how the errors propagate from the estimated linear-regression parameters to  $\theta$ . Given a linear relationship between  $\Delta T$  and  $\ln(t)$ ,  $\ln[t/(t - \Delta t_h)]$  or  $\ln[(t + t_0)/(t + t_0 - \Delta t_h)]$ , a simple linear regression provides the parameters  $m$  and  $b$  (the slope and the intercept, respectively) of the straight line that minimizes the sum of the squared residuals. Assuming a negligible error on the time, the variance of the measured temperature increments is

$$\sigma^2 = \frac{1}{N-2} \sum_{i=1}^N [mx_i + b - \Delta T_i]^2, \quad [14]$$

where the subscript  $i$  denotes the  $i$ th measurement, and  $x_i = \ln(t_i)$  for the analysis of the heating phase,  $x_i = \ln[t_i/(t_i - \Delta t_h)]$  and  $x_i = \ln[(t_i + t_0)/(t_i + t_0 - \Delta t_h)]$  for the analysis of the cooling phase with and without time correction  $t_0$ , respectively. The uncertainty on the slope and the intercept is obtained by propagating the uncertainty on the temperature increments, which yields

$$\sigma_m^2 = \frac{N}{\Delta} \sigma^2, \quad [15]$$

and

$$\sigma_b^2 = \frac{\sum_{i=1}^N x_i^2}{\Delta} \sigma^2, \quad [16]$$

respectively, with

$$\Delta = N \sum_{i=1}^N x_i^2 - \left[ \sum_{i=1}^N x_i \right]^2. \quad [17]$$

Propagating the uncertainty to thermal conductivity we obtain

$$\frac{\sigma_\lambda^2}{\lambda^2} = \frac{\sigma_m^2}{m^2} + \frac{\sigma_Q^2}{Q^2}, \quad [18]$$

which shows that the relative error on the thermal conductivity is simply equal to the relative error on the slope, when the relative error on the heat-source strength  $\sigma_Q/Q$  is negligible. On the other hand, the relative uncertainty on the volumetric heat capacity calculated by standard error propagation through Eq. [8], (see, e.g., Taylor, 1997) is

$$\frac{\sigma_C^2}{C^2} = (1 + 4\pi\lambda R)^2 \frac{\sigma_\lambda^2}{\lambda^2} + \frac{b^2}{m^2} \left( \frac{\sigma_m^2}{m^2} + \frac{\sigma_b^2}{b^2} \right) + 4 \frac{\sigma_a^2}{a^2} + (4\pi\lambda R)^2 \frac{\sigma_R^2}{R^2}, \quad [19]$$

which is always larger than the relative error on  $\lambda$ . Notice that the relative variances of the slope and the intercept are amplified by a factor  $(b/m)^2$ . The exponential dependence on the ratio  $b/m$ , as given by Eq. [8], brings this term to be a multiplier of the uncertainty, unavoidably leading to large errors whenever the ratio is not small. Moreover, an accurate estimate of  $C$  requires an accurate measurement of the (small) external source radius,  $a$ , and of the thermal resistance of the insulator,  $R$ . Propagation of  $\sigma_\lambda$  through Eq. [13] provides the uncertainty  $\sigma_\theta$  on the retrieved values of  $\theta$ . Assuming unaffected by error the values of  $\lambda_{dry}$  and  $\lambda_{sat}$ , the error on the volumetric water content is

$$\sigma_\theta = \left| \frac{dK_c}{d\theta} \right|^{-1} \sigma_{K_c} = \left| \frac{dK_c}{d\theta} \right|^{-1} \frac{\sigma_\lambda}{\lambda_{sat} - \lambda_{dry}} = \left| \frac{d\lambda}{d\theta} \right|^{-1} \sigma_\lambda, \quad [20]$$

which

shows that the error on  $\lambda$  is amplified in regions of large water content, where  $d\lambda/d\theta$  is small.

## Experimental Setup

### The Lysimeter and the Soil

The deployment of a fiber optic cable has been performed in a weighable lysimeter at EPFL (Fig. 2). The lysimeter, a polyester tank of height 2.50 m and diameter 1.20 m, is placed on three high-accuracy loading cells (not used in this work). The top of the lysimeter is flush with the surrounding soil surface and exposed to meteorological forcing. The bottom of the lysimeter has been prepared with a filter consisting of 0.25 m of gravel topped with 0.25 m of coarse sand. The remaining 2 m have been filled with an alluvial loam from Conthey, VS, in southern Switzerland. To obtain as homogenous as possible packing, the lysimeter was filled through successive steps each involving a gentle deposition of soil followed by several saturation-drainage cycles in an attempt to achieve ideal settling. During the filling, the lysimeter was equipped with nine capacitance-based 5TM probes (Decagon Device Inc.) and nine type T (copper-constantan) thermocouples, which were placed in the soil at the nine different depths (see Fig. 2). Data were collected every 60 s by a Campbell CR5000 datalogger for the 5TM probes and by a solid state multiplexer for thermocouples (Campbell AM25T) and directly transferred to a PC installed in the basement. Several soil samples were taken to determine particle size distribution, bulk density, porosity, and residual water saturation (Table 1). The dry-soil,  $\lambda_{dry}$ , and saturated soil,  $\lambda_{sat}$ , thermal conductivity were measured in small samples filled with oven-dried and saturated soil, respectively, by means of two five-needles multi-function heat pulse probes (MFHPP) (Mori et al., 2003; Kamai

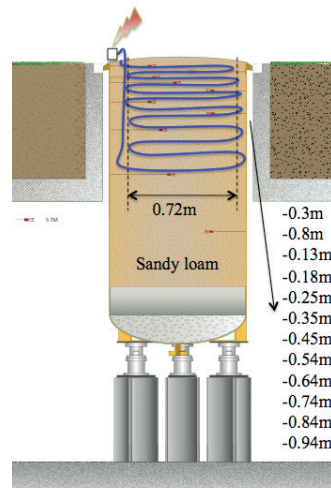


Fig. 2. The EPFL weighable lysimeter has been equipped with several sensors during the campaign of summer 2010. The optical fiber (sketched with a blue line) is installed in the lysimeter forming nine loops at approximate depth indicated in the drawing. To obtain independent volumetric water content measurements, 5TM probes (represented by small prongs) are also installed in the lysimeter at depths 0.3, 0.8, 0.13, 0.18, 0.25, 0.35, 0.45, 0.60, and 1 m.

et al., 2008); the measured values are in good agreement with the values reported by Lu et al. (2007) for a similar type of loam. Independent measurements of  $\lambda$  at different soil saturations were also obtained with the same technique employed for  $\lambda_{dry}$  and  $\lambda_{sat}$ . A calibrated Lu model was obtained by fitting the experimental data with the free parameter  $\alpha_{Fit}$  and values  $\lambda_{dry}$  and  $\lambda_{sat}$  from the laboratory measurements. In Fig. 1, the calibrated Lu curve is compared with a curve employing the standard value of  $\alpha$  for fine soils from Lu et al. (2007). The similarity between Conthey loam and fine-textured soils is due to the high fraction of fine particles (smaller than 200  $\mu\text{m}$ ) and the low bulk density, which is much closer to silt and clay than to pure sand (see, e.g., Lu et al., 2007). We observe small difference between the two curves at medium water contents [between 0.2 and 0.3 ( $\text{m}^3 \text{m}^{-3}$ )], where the inferred  $\theta$  can differ by 0.04 ( $\text{m}^3 \text{m}^{-3}$ ) depending on the curve employed. This suggests that Lu's model with standard values of  $\alpha$  provides a good approximation and can be used to estimate the water content

Table 1. Properties of the loam (from Conthey, VS, southern Switzerland).

Property†	Value	Unit
Coarse sand (200–2000 $\mu\text{m}$ )	17‡	%
Fine sand (50–200 $\mu\text{m}$ )	38‡	%
Coarse silt (20–50 $\mu\text{m}$ )	18.3‡	%
Fine silt (2–20 $\mu\text{m}$ )	16.7‡	%
Clay (<2 $\mu\text{m}$ )	10‡	%
$\theta_{sat}$	0.43‡	[ $\text{m}^3 \text{m}^{-3}$ ]
$\theta_{res}$	0.08‡	[ $\text{m}^3 \text{m}^{-3}$ ]
$\rho_b$	1.3‡	[ $\text{kg m}^{-3}$ ]
$\lambda_{dry}$	0.233§	[ $\text{W m}^{-1} \text{K}^{-1}$ ]
$\lambda_{sat}$	1.579§	[ $\text{W m}^{-1} \text{K}^{-1}$ ]
$\alpha$	0.27¶	[-]
$\alpha_{Fit}$	0.67§	[-]

† Subscripts: sat, saturation value; res, residual value; dry, dry value; Fit, fitted value.

‡ Laboratory granulometric analysis.

§ Laboratory tests with heat pulse probes.

¶ Lu et al. (2007).

with a reasonable accuracy in cases where a specific calibration of the model is not available. All soil parameters relevant for this study are summarized in Table 1.

### DTS and Optical Fiber

The optical fiber was installed during the lysimeter filling. The cable used (BRUsteel from Brugg Cable) consists of a stainless steel loose tube containing four multimode 50  $\mu\text{m}$  cores and 125  $\mu\text{m}$  cladding fibers; it is armored with an outer sheath of interlaced metal wires, which guarantees flexibility and high protection in outdoor applications, and covered by a polyamide jacket for thermal and electrical insulation. The external cable diameter is 3.8 mm and the total cable length is 280 m. Figure 3 shows the different layers characterizing the composite structure of the fiber cable. The fiber optic cable is connected to a DTS ORYX (Sensornet Inc.) which employs a laser pulse time of 10 ns corresponding to a spatial resolution of 1 m, and acquires measurements at a frequency of 1/15 Hz. About 32-m of fiber optic cable were buried in the lysimeter during the filling starting at from depth of 0.94 m from the surface. The cable was installed in a long spiral consisting of twelve rings of approximate diameter 0.72 m; the vertical distance between rings decreases approaching the surface as sketched in Fig. 2. To preserve the shape and the depth of the spiral, the fiber has been wound around some thin bamboo sticks that were temporarily inserted in the soil and removed at the end of the filling (see Fig. 4). This technique avoided the presence of a permanent rigid structure in the lysimeter that could potentially disturb the packing, but the lack of anchorage left the fiber and the probes free to move during the natural settling that unavoidably occurred with time and exposure to meteorological conditions (rainfall, wind, evaporation). Since a subsidence of about 0.05 m was observed during the 3 mo between the end of the filling and the experiments, a depth uncertainty of about 0.02 m can be realistically estimated with respect to the value reported in Fig. 2. Before entering and after exiting the soil, the cable was immersed in two calibrating baths placed in the basement: a cold bath consisting of ice at temperature  $-0.4^\circ\text{C}$  and a warm bath consisting of water mixed through an aquarium bubbler and kept at  $21^\circ\text{C}$  by a thermistor. The temperatures of the baths were monitored by two PT100 (Campbell Sci.) and the averaged temperature recorded over the entire duration of the experiment (about 24 h) was used to calibrate the optical fiber. The use of cold and hot baths allowed calibrating both the offset and the slope. We have observed a deterioration of the declared sensitivity of the DTS ORYX ( $0.1^\circ\text{C}$ ), which has been estimated of the order of  $\pm 0.4^\circ\text{C}$  based on the temperature fluctuations in the calibrating baths (see Fig. 5). This sensitivity loss can be due, for instance, to slight differences in the vibrational energy between the molecules that cause a broadening of the Stokes and Anti-Stokes Raman peaks; to the differential attenuation that leads to changes in the input-output intensity ratio; or to the intensity loss in the transmission due to the splicing between the connectors and the fibers.



Fig. 3. The BRUsteel cable. From left to right: the nylon jacket (1), the inter-laced steel wires (2), the stainless steel loose tube (3), the four multimode fibers (4). In (3) is applied the electrical heating. From Brugg Cables (<http://www.bruggcables.com>), technical sheet of the BRUsteel fiber cable.



Fig. 4. Installation of the fiber optic cable. During uniform packing of the lysimeter, the soil is saturated and the fiber optic cable is wrapped around a bamboo-stick structure, which is removed after filling.

### Fiber Heating and Probe-Method Measurements

To generate the heat source necessary for the probe method, the metal sheath was heated allowing an electric current to flow through the buried portion of the cable. A few centimeters of the Polyamide cover were removed at the two points immediately outside the soil; two small battery clamps were fixed to the uncovered metal sheath of the BRUsteel and plugged to the domestic electric network at 230 VAC. To avoid shock risks, the clamps were put in two boxes for electric cable filled with foam for thermal insulation. To reduce both the applied voltage and the current intensity along the sheath, a power consumer with two regulations was connected to the circuit. A switch allowed the electric current to start/stop, while a Voltmeter and an Amperometer monitored voltage and current intensity, respectively. Of the six heating events performed over a 24-h period (from the afternoon of 28 October through the morning of 29 Oct. 2010), three had an electrical voltage of 63 V and three a more intense voltage of 115.6 V. Since the measured resistance of the metal sheath is  $0.365 \Omega \text{ m}^{-1}$ , the dissipated power can be calculated to be about  $11 \text{ W m}^{-1}$  and  $36 \text{ W m}^{-1}$  for the low and high voltage events, respectively. These powers are of the same order of magnitude as those applied by Weiss (2003) and Sayde et

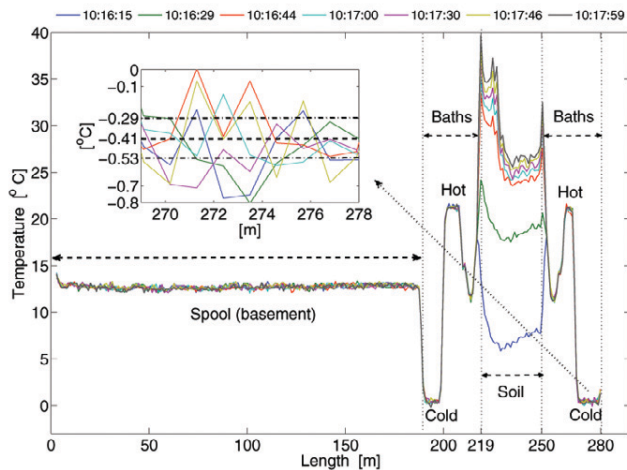


Fig. 5. Temperature profiles measured by the optical fiber during a heating pulse. The subplot shows the temperature in the cold bath which displays fluctuations on the order of  $\pm 0.4^\circ\text{C}$  around the mean value of  $-0.41^\circ\text{C}$  (dashed line, measured with PT100 probe  $\pm$  standard deviation over the entire experiments duration).

al. (2010), i.e.,  $20 \text{ W m}^{-1}$ . All heating events lasted  $\Delta t_h = (120 \pm 1) \text{ s}$  and were followed by long cooling periods.

## Results

### Temperature Measurements during Heating and Cooling

The temperature profile along the whole fiber optic cable length is shown in Fig. 5 for several times during one of the heating events. From the profile, the calibrating baths are clearly visible, and it is possible to identify the heated portion of the cable as the section between the lengths 219 m and 250 m. Due to the partial burial of the fiber optic cable, the two extreme values of this portion are excluded from the following data analysis. The length of the fiber considered is therefore 30 m (larger fiber-length values correspond to deeper soil). In this section, the temperature response of the soil to the heating is clearly visible, and shows a more rapid increase and larger temperature increments close to the surface. This indicates a lower thermal conductivity near the surface, which is consistent with the typically lower volumetric water content of the shallower soil. An example of measured temperature-increment profiles along the buried section of the fiber optic cable during cooling is shown in Fig. 6. As in the heating phase, the shallow soil displays a reduced ability to transfer heat and the temperature relaxation to its value before heating is slower. Compared to the heating phase which has a duration of 120 s, the cooling phase is longer 300 s after heating stopped the temperature-increment is still well-visible. After 800 s, the temperature-increment reduces to zero almost everywhere, except close to the surface where a small positive increment is detectable. The temperature increments observed during our experiments were of the same magnitude as those measured in other studies (e.g., Weiss, 2003 and Sayde et al.,

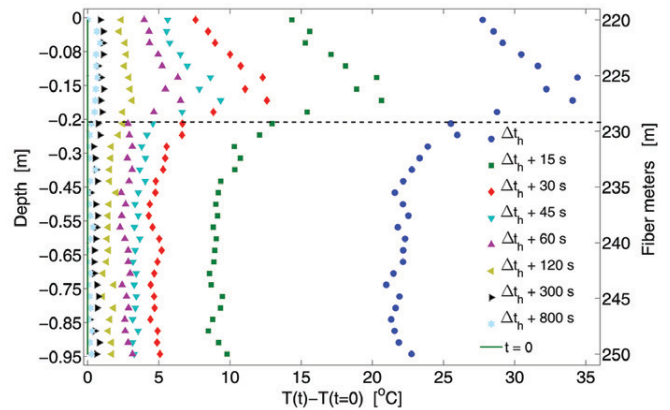


Fig. 6. Temperature increments,  $T(t) - T(t = 0)$ , measured by the fiber optic cable during cooling (heat pulse stopped at  $\Delta t_h = 120 \text{ s}$ ). The dashed line highlights the interface between two zones showing different responses to the heat pulses: in the shallower zone (approximately the initial 9 m of the buried fiber) temperature sensitively increases during heating, whereas the deeper zone shows a limited temperature increment.

2010). Note that the temperature measured by the optical fiber during heating and cooling is not the temperature of the soil. Due to the presence of the polyamide jacket, which acts as an insulation layer (see Estimation of Thermal Properties by the Probe Method), the actual temperature increment in the soil is smaller and it is unlikely that it can induce rapid water redistribution around the fiber optic cable.

### Determination of the Thermal Properties by the Probe Method

The soil-temperature response to the heat pulse is used to determine the thermal properties of the soil. The probe method can be applied both to the heating and the cooling phase by employing the asymptotic solutions for late time (Eq. [8] and [10], respectively). For the data collected in this experiment, a tentative analysis of the heating phase showed that the duration  $\Delta t_h = 120 \text{ s}$  was too short to approach the asymptotic solution. This was verified by plotting  $\Delta T(t_i) - \Delta T(t_{i-1}) / \ln(t_i) - \ln(t_{i-1})$  as a function of  $\ln(t_i)$  for all the times  $t_i$  at which temperature measurements were available (seven per heating event). This diagnostic plot (not presented here) showed that this quantity was decreasing during the entire heating phase, which indicates that the asymptotic solution was not approached within 120 s. In contrast to the heating phase, the cooling phase offers the advantage of longer duration and more rapid approach to the asymptotic solution (see the discussion at the end of Estimation of Thermal Properties by the Probe Method, which shows how the first term neglected is order  $\ln \tau / \tau^2$  instead of order  $\ln \tau / \tau$ ). On the other hand, the signal-to-noise ratio tends to decrease at later time, such that the first point to be included in the linear regression to estimate the thermal conductivity has to be carefully chosen. The diagnostic plot employed for the heating phase is not effective for the cooling phase because the differences

between temperature increments become very small for  $t \gg \Delta t_h$  due to the unfavorable signal/noise ratio. To verify the degrees of accuracy of the asymptotic approximation, we compare the thermal conductivity values obtained considering only temperature increments measured after a threshold time,  $t_{thr} > \Delta t_h$ . By increasing the threshold, the estimated values of thermal conductivity tend to the asymptotic value, whereas the uncertainty increases due to the fewer data points employed and, most importantly, to the deterioration of the signal/noise ratio. The diagnostic plots for the linear regressions of the three cooling events yielded similar results and revealed a good repeatability of the experiment, which is a direct consequence of the minor water-content variations over the entire period. As the three cooling events yielded statistically consistent estimates, we decided to perform a simultaneous linear regression of all data, which allows a significant reduction of the statistical uncertainty by increasing the number of data points. All the results presented in the remainder of the paper are obtained by simultaneous analysis of the three cooling events. Figure 7 shows the diagnostic plot from simultaneous linear regression of the three cooling events. The thermal conductivity is plotted as a function of the threshold time (i.e., as a function of the time from which temperature increments are included in the linear regression) for two representative meters of fiber, one close to the surface and the other close to the bottom of the spiral of fiber optic cable. For both fiber intervals, the estimated thermal conductivities initially grow when the threshold time is increased, which indicates that the temperature increment is not yet asymptotic and that the thermal conductivity is systematically underestimated. After a certain threshold time, the estimated thermal conductivities remain constant within statistical uncertainty. The threshold after which the estimated  $\lambda$  values remain constant is the optimal starting point, because it is consistent with the assumption that the solution is

asymptotic and allows to minimize the uncertainty propagation to the slope which tends to rapidly grow if the threshold is raised further. Indeed, as it is evident from the error analysis in Error Analysis, the points characterized by larger  $x_i = \ln[t_i/(t_i - \Delta t_h)]$  are more effective in reducing the propagation of the variance of the measured temperature increments to the uncertainty of  $m$  (Eq. [15] and [17]); in contrast the use of points characterized by small  $x_i = \ln[t_i/(t_i - \Delta t_h)]$  leads to small  $\Delta$  (Eq. [17]). (Note that a smaller slope uncertainty does not necessarily mean that the hypothesis of linear dependence is better satisfied, as it is evident from Fig. 7). The threshold values are 170 s and 90 s for the shallower and the deeper fiber meter, respectively. The different thresholds for the shallower and deeper measurements is due to the fact that, for the solution to be asymptotic, we have to require that  $t - \Delta t_h \gg a^2 c/\lambda$ , and shallower soil is drier and has lower  $\lambda$ . According to the results of the diagnostic plot, Fig. 7, and to account for the difference between dry and wet soil, we have chosen a threshold of 170 s for the first 9 m of optical fiber (in dryer soil) and a threshold of 90 s for the remaining part of the fiber. The estimated thermal conductivities are plotted in Fig. 8 (blue squares) as a function of the fiber length and show an abrupt transition from a region of lower to a region of higher thermal conductivity around the 0.2-m depth.

### Determination of Thermal Properties with Time Correction

If the asymptotic limit of Eq. [9] is not yet reached, the analysis above leads to a systematic underestimation of the thermal conductivity as it can be clearly observed from Fig. 7. Since the diagnostic plot suggests that the data are not yet strictly asymptotic, we repeat the analysis introducing a time correction,  $t_0$ , in Eq. [11] (Van der Held and Van Drunen, 1949; deVries, 1952). The standard method to infer  $t_0$ , which is based on an analysis of the increment ratio  $\Delta t/\Delta T$  (see, e.g., Van der Held and Van Drunen, 1949), has proven inapplicable to our data due to the large fluctuations of the increment ratio at later time. Therefore, we proceed differently and perform a nonlinear regression of  $\Delta T$  as function of  $t$  with two free parameters,  $t_0$  and  $\lambda$ . (For this purpose we have used the nonlinear-regression package `cftool` of MATLAB; <http://www.mathworks.ch/help/toolbox/curvefit/cftool.html>; accessed February 2012). The uncertainty on  $\lambda$  (indicated by the error bars in Fig. 8) is calculated from the equations presented in the Error Analysis section assuming that the uncertainty on  $t_0$  can be neglected. As for the case without time correction, we determine the optimal threshold time from a diagnostic plot analogous to the one in Fig. 7. The threshold time,  $t_{thr}$ , is determined independently for each meter of the optical fiber and varies between 45 s and 100 s in shallower soil (above the abrupt transition in thermal conductivity), and between 15 s and 45 s in deeper soil. The values of  $t_0$  are all negative and range from  $-26$  to  $-66$  s close to the surface, and from  $-12$  to  $-24$  s toward the bottom of the fiber optic cable coil. Note that these threshold times are significantly shorter than those from the analysis without  $t_0$ , indicating that earlier data can be employed to obtain an accurate estimate of the thermal

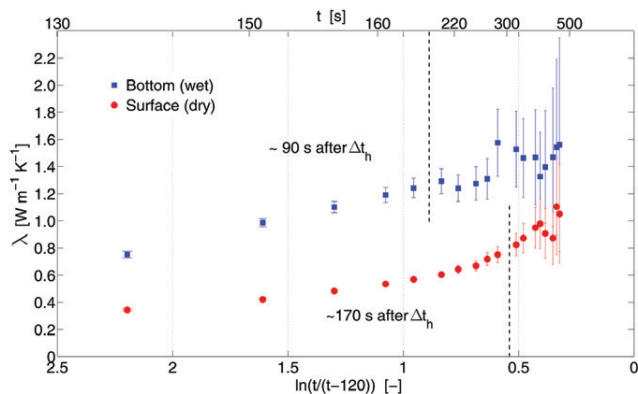


Fig. 7. Diagnostic plots of two representative sections of the optical fiber: one at the bottom of the coil (meter 248, blue), the other close to the surface (meter 226, red). The thermal conductivity is plotted as a function of the time from which temperature increments are included in the linear regression. Shown are the results for three cooling events considered together. The dashed vertical lines indicate the time after which the estimated thermal conductivities are consistent within statistical uncertainty (i.e., 90 s for the deeper and 170 s for the shallower fiber section, respectively).

conductivity. Negative values of the time correction,  $t_0$ , in Eq. [11] have also been found in previous studies (e.g., Van der Held and Van Drunen (1949) and Bristow et al. (1994)) and confirm that the data analyzed are not yet asymptotic. More negative values close to the surface indicate that in dry conditions the asymptotic regime is reached later than in wet conditions, when the time corrections are closer to zero. The results of this analysis are plotted in Fig. 8 and show that the estimated thermal conductivity is systematically larger and the statistical error significantly reduced compared to the results obtained without time correction.

### Estimate of the Volumetric Water Content

According to the constitutive relationships in Fig. 1, the variation of thermal conductivity along the fiber indicates the presence of a variably wetted soil (under the assumption of constant soil texture and bulk density), with a clear distinction between the drier zone around the initial nine meters of fiber optic cable (shallower soil) and the wetter zone (deeper soil). The volumetric water contents obtained by inverting the calibrated Lu's model (solid line in Fig. 1) are presented in Fig. 9 as a function of the fiber depth, which has been estimated from the geometry of the coil. The error bars indicate the error propagation obtained from Eq. [20]. The error on  $\theta$  is smaller in the dryer region, grows in the wet region, and exhibits a maximum at about 0.54 to 0.58 m from the surface for both cases. This larger error is due to the dependence of  $\sigma_0$  on  $|dK_c/d\theta|^{-1}$  (Eq. [20]) which amplifies the uncertainty in a region where the constitutive relationship is rather flat. In Fig. 9 the results obtained both with and without time correction are compared with the volumetric water contents independently measured by nine 5TM probes. The analysis without time correction  $t_0$  yields a systematic underestimation of the water content, whereas the agreement between DTS and 5TM probes is substantially improved when  $t_0$  is introduced. In particular, between 0.2 and 1 m the agreement is excellent, with an accuracy of  $0.04 \text{ (m}^3 \text{ m}^{-3}\text{)}$  in the worst case at the 0.6-m depth. At depths shallower than 0.2 m, both analysis (with and without time correction) noticeably underestimate the volumetric water content.

### Conclusions

Through analysis of the cooling phase of a heated optical fiber we have estimated the thermal conductivity of the soil and inferred the volumetric water content. The approach relies on the use of asymptotic solutions for the propagation of heat and on the availability of reliable models (Lu et al., 2007) to relate thermal conductivity and soil moisture. Comparison with independent measurements of soil moisture (obtained using 5TM probes) demonstrated that AHFO measurements underestimate the water content in drier soils. This is due to the longer time required for the temperature increment to become asymptotic in poorly conductive media. In wetter soils, however, the estimation of volumetric water content was excellent. In this region, the introduction of a time correction allows to reduce the statistical uncertainty of volumetric water content measurements below  $0.02 \text{ (m}^3 \text{ m}^{-3}\text{)}$ . For future application of

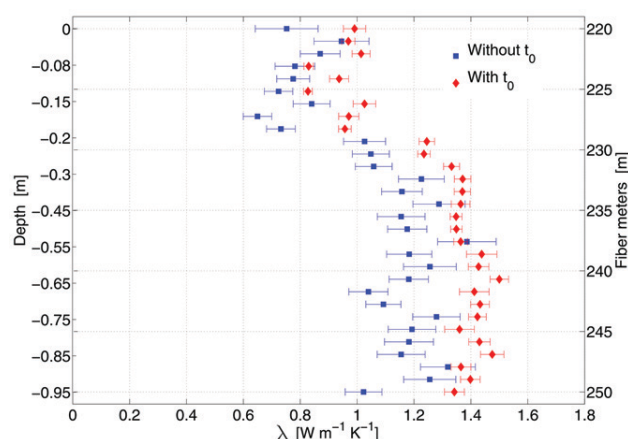


Fig. 8. Estimated thermal conductivities as a function of the fiber length in the case with time correction  $t_0$  (red diamonds) and without (blue squares).

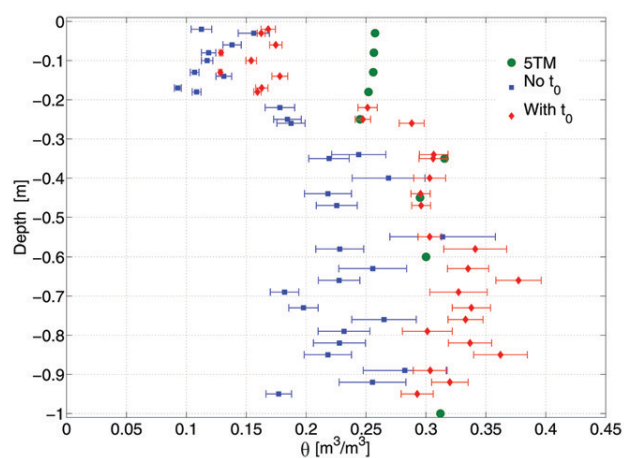


Fig. 9. Volumetric water contents at different depths estimated from thermal conductivities by inversion of the Lu et al. (2007) model with calibrated parameter  $\alpha_{\text{Fit}}$  for the case of  $\lambda$  inferred with  $t_0$  (diamonds) and without (squares). Circles represent the independent 5TM measurements.

the AHFO method, there are areas for improvement. One should make use of longer heating and cooling events to allow a more sound application of the asymptotic solutions to the temperature-increment evolution in dry soils. Note that the asymptotic analysis offers the advantage of not requiring one to account for the effects of the polyamide insulator. The BRUsteel cable consists of a central steel loose tube protected by steel interlaced wires and by 0.3 mm of nylon jacket. The effect of this composite structure has been clearly observed at early time when the measured temperature increment was uniform along the entire cable and influences the behavior of pre-asymptotic temperature increments. To reduce the statistical uncertainty of the method and the error propagation on the estimated volumetric water content ideally more data points should be used in the linear regression. This can be addressed in practice by allowing for longer heating and cooling phases and making use of DTS devices that measure with higher frequency



than the one employed in the present study. The results presented here are very encouraging and demonstrate that the error can be reduced and a good estimate of volumetric water content can be obtained in wet soils by employing a time correction. Future studies should allow for longer heat pulses to improve the signal/noise ratio. This will also require an assessment of the effects of larger heat supply on soil water redistribution.

## Acknowledgments

The authors are grateful to the reviewers for the helpful suggestions which greatly improved the quality of the manuscript. Special thanks are also addressed to J. Golay, F. Comino, M. Froidevaux and S. Varun (EPFL), D. Jougnot (University of Lausanne) and K. Hilgerson (TU Delft) for their precious collaboration. This work was funded by the Swiss National Science Foundation (200021-1222088/1). Ivan Lunati is a Swiss National Science Foundation (SNSF) Professor at the University of Lausanne (supported by the SNSF grant number PP00P2-123419/1).

## References

- Assouline, S., K. Narkis, S.W. Tyler, I. Lunati, M.B. Parlange, and J.S. Selker. 2010. On the diurnal soil water content dynamics during evaporation using dielectric methods. *Vadose Zone J.* 9:709–718. doi:10.2136/vzj2009.0109
- Auñeiger, M., M. Conrad, S. Perzmaier, and P. Porras. 2005. Improving a fiber optics tool for monitoring leakage. *Hydro Rev. Worldwide* 13:18–23.
- Bear, J. 1979. *Hydraulics of groundwater*. Dover, New York. p. 467–472.
- Bristow, K.L., G.S. Campbell, and C. Calissendorff. 1993. Test of a heat pulse probe for measuring changes in soil water content. *Soil Sci. Soc. Am. J.* 57:930–934. doi:10.2136/sssaj1993.03615995005700040008x
- Bristow, K.L., R.D. White, and G.J. Kluitenberg. 1994. Comparison of single and dual probes for measuring soil thermal properties with transient heating. *Aust. J. Soil Res.* 32:447–464. doi:10.1071/SR9940447
- Campbell, J.E. 1990. Dielectric-properties and influence of conductivity in soils at one to 50 MHz. *Soil Sci. Soc. Am. J.* 54(2): 332–341. doi:10.2136/sssaj1990.03615995005400020006x
- Carslaw, H.S., and J.C. Jaeger. 1959. *Conduction of heat in solids*. 2nd ed. Clarendon Press, Oxford, UK.
- Chung, S.O., and R. Horton. 1987. Soil heat and water flow with a partial surface mulch. *Water Resour. Res.* 23(12):2175–2186. doi:10.1029/WR023i012p02175
- Côté, C., and J.-M. Konrad. 2005. A generalized thermal conductivity model for soils and construction materials. *Can. Geotech. J.* 42:443–458. doi:10.1139/t04-106
- de Vries, D.A. 1952. A nonstationary method for determining thermal conductivity of soil in situ. *Soil Sci.* 73:83–90. doi:10.1097/00010694-195202000-00001
- de Vries, D.A., and A.J. Peck. 1958. On the cylindrical probe method of measuring thermal conductivity with special reference to soils. Part 1. Extension of theory and discussion of probe characteristics. *Aust. J. Phys.* 11:255–271. doi:10.1071/PH580255
- Freifeld, B.M., S. Finsterle, T.C. Onstott, P. Toole, and M. Pratt. 2008. Ground surface temperature reconstructions: Using in situ estimates for thermal conductivity acquired with a fiber optic distributed thermal perturbation sensor. *Geophys. Res. Lett.* 35:L14309. doi:10.1029/2008GL034762
- Gratton, K.T.V., and B.T. Meggitt. 2000. *Optical fiber sensor technology*. Kluwer Academic Publishers, Boston, MA.
- Hopmans, J.W., J.M.H. Hendrickx, and J.S. Selker. 1999. Emerging measurement techniques for vadose zone characterization. In M.B. Parlange and J.W. Hopmans, editors, *Vadose zone hydrology: Cutting across disciplines*. Oxford Univ. Press, New York. p. 279–316.
- Johansen, O. 1975. *Thermal conductivity of soils*. Ph.D. diss. Norwegian Univ. of Science and Technol., Trondheim (CRREL draft transl. 637).
- Jones, S.B., and D. Or. 2004. Frequency domain analysis for extending time domain reflectometry water content measurement in highly saline soils. *Soil Sci. Soc. Am. J.* 68(5):1568–1577.
- Jougnot, D., and A. Revil. 2010. Thermal conductivity of unsaturated clay-rocks. *Hydrol. Earth Syst. Sci.* 14:91–98. doi:10.5194/hess-14-91-2010
- Kamari, T., A. Tuli, G.J. Kluitenberg, and J.W. Hopmans. 2008. Soil water flux density measurements near 1cm<sup>-1</sup> using an improved heat pulse probe design. *Water Resour. Res.* 44:W00D14. doi:10.1029/2008WR007036
- Keller, C.A., H. Huwald, M.K. Vollmer, A. Wenger, M. Hill, M.B. Parlange, and S. Reimann. 2011. Fiber optic distributed temperature sensing for the determination of the nocturnal atmospheric boundary layer height *Atmos. Meas. Tech.* 4:143–149.
- Lu, S., T. Ren, Y. Gong, and R. Horton. 2007. An improved model for predicting soil thermal conductivity from water content at room temperature. *Soil Sci. Soc. Am. J.* 71:8–14. doi:10.2136/sssaj2006.0041
- Mohamed, S.O., P. Bertuzzi, A. Bruand, L. Raison, and L. Bruckler. 1997. Field evaluation and error analysis of soil water content measurement using the capacitance probe method. *Soil Sci. Soc. Am. J.* 61:399–408. doi:10.2136/sssaj1997.03615995006100020006x
- Mori, Y., J.W. Hopmans, A.P. Mortensen, and G.J. Kluitenberg. 2003. Multifunctional heat pulse probe for the simultaneous measurement of soil water content, solute concentration, and heat transport parameters. *Vadose Zone J.* 2(4):561–571. doi:10.2113/2.4.561
- Nadler, A., and Y. Lapid. 1996. An improved capacitance sensor for in situ monitoring of soil moisture. *Aust. J. Soil Res.* 34:361–368. doi:10.1071/SR9960361
- Perzmaier, S., M. Auñeiger, and M. Conrad. 2004. Distributed fiber optic temperature measurements in hydraulic engineering- Prospects of the heat-up method. Proceedings of the 72nd ICOLD Annual Meeting Workshop on Dam Safety Problems and Solutions-Sharing Experience, Korean Natl. Comm. on Large Dams, 16–22 May, Seoul, Korea.
- Perzmaier, S., K.H. Straer, T. Strobl, and M. Auñeiger. 2006. Integral seepage monitoring on open channel embankment dams by the DFOT heat pulse method. Proceedings of the 74th Annual Meeting, Int. Comm. on Large Dams, Barcelona, Spain.
- Robinson, D.A., S.B. Jones, J.A. Wraith, D. Or, and S.P. Firedmen. 2003. A review of advances in dielectric and electrical conductivity measurements in soils using time domain reflectometry. *Vadose Zone J.* 2:444–475.
- Robinson, D.A., C.S. Campbell, J.W. Hopmans, B.K. Hornbuckle, S.B. Jones, R. Knight, F. Ogden, J. Selker, and O. Wendroth. 2008. Soil moisture measurement for ecological and hydrological watershed-scale observatories: A review. *Vadose Zone J.* 7:358–389. doi:10.2136/vzj2007.0143
- Sayde, C., C. Gregory, M. Gil-Rodriguez, N. Tuffllaro, S.W. Tyler, N.C. van de Giesen, M. English, R. Cuenca, and J.S. Selker. 2010. Feasibility of soil moisture monitoring with heated fiber optics. *Water Resour. Res.* 46:W06201. doi:10.1029/2009WR007846
- Steele-Dunne, S.C., M.M. Rutten, D.M. Krzeminska, M. Hausner, S.W. Tyler, J.S. Selker, T.A. Bogaard, and N.C. van de Giesen. 2010. Feasibility of soil moisture estimation using passive distributed temperature sensing. *Water Resour. Res.* 46:W03534. doi:10.1029/2009WR008272
- Selker, J., N. van de Giesen, M. Westhoff, W. Luxemburg, and M.B. Parlange. 2006a. Fiber optics opens window on stream dynamics. *Geophys. Res. Lett.* 33:L24401. doi:10.1029/2006GL027979
- Selker, J., L. Thevenaz, H. Huwald, A. Mallet, W. Luxemburg, N. van de Giesen, M. Stejskal, J. Zeman, M. Westhoff, and M.B. Parlange. 2006b. Distributed fiber optic temperature sensing for hydrologic systems. *Water Resour. Res.* 42:W12202. doi:10.1029/2006WR005326
- Seyfried, M.S., and M.D. Murdock. 2001. Response of a new soil water sensor to variable soil, water content, and temperature. *Soil Sci. Soc. Am. J.* 65:28–34. doi:10.2136/sssaj2001.65128x
- Seyfried, M.S., and M.D. Murdock. 2004. Measurement of soil water content with a 50 MHz soil dielectric sensor. *Soil Sci. Soc. Am. J.* 68:394–403. doi:10.2136/sssaj2004.0394
- Shiozawa, S., and G.S. Campbell. 1990. Soil thermal conductivity. *Remote Sens. Rev.* 5:301–310. doi:10.1080/02757259009532137
- Taylor, J.R. 1997. *An introduction to error analysis*. Oxford Univ. Press, Oxford, UK. p. 40–74.
- Topp, G.C., S. Zegelin, and I. White. 2000. Impacts of the real and imaginary components of relative permittivity on time domain reflectometry measurements in soils. *Soil Sci. Soc. Am. J.* 64:1244–1252. doi:10.2136/sssaj2000.6441244x
- Topp, G.C., J.L. Davis, and A.P. Annan. 1980. Electromagnetic determination of soil water content: Measurement in coaxial transmission lines. *Water Resour. Res.* 16:574–582. doi:10.1029/WR016i003p00574
- Tyler, S., S. Burak, J. McNamara, A. Lamontagne, J. Dozier, and J. Selker. 2008. Spatially distributed temperatures at the base of two mountain snowpacks measured with fiber optic sensors. *J. Glaciol.* 54(187):673–679. doi:10.3189/002214308786570827
- Tyler, S.W., J.S. Selker, M.B. Hausner, C.E. Hatch, T. Torgersen, C.E. Thodal, and G. Schladow. 2009. Environmental temperature sensing using Raman spectra DTS fiber optic methods. *Water Resour. Res.* 45:W00D23. doi:10.1029/2008WR007052
- Van der Held, E.F.M., and F.G. Van Drunen. 1949. A method of measuring the thermal conductivity of liquids. *Physica* 15(10):865–881. doi:10.1016/0031-8914(49)90129-9
- Vercauteren, N., H. Huwald, E. Bou-Zeid, J.S. Selker, U. Lemmin, M.B. Parlange, and I. Lunati. 2011. Evolution of superficial lake water temperature profile under diurnal radiative forcing. *Water Resour. Res.* 47:W09522. doi:10.1029/2011WR010529
- Weiss, J.D. 2003. Using fiber optics to detect moisture intrusion into a landfill cap consisting of a vegetative soil barrier. *J. Air Waste Manage. Assoc.* 53:1130–1148. doi:10.1080/10473289.2003.10466268
- Westhoff, M.C., H.H.G. Savenije, W.M.J. Luxemburg, G.S. Stelling, N.C. van de Giesen, J.S. Selker, L. Pfister, and S. Uhlenbrook. 2007. A distributed stream temperature model using high resolution temperature observations. *Hydrol. Earth Syst. Sci.* 11:1469–1480. doi:10.5194/hess-11-1469-2007



## 7 Conclusions and Future Work

The dissertation focused on the investigation of the tight coupling between heat transfer and moisture dynamics in soils. The results presented are based on both theoretical-numerical analysis and field and laboratory measurements. Particular attention has been dedicated to: (i) numerical investigations of water vapor dynamics close to the soil surface; (ii) measurement of key components of energy and moisture transport at different spatiotemporal scales; (iii) analytical-numerical study of both prognostic and diagnostic methods to optimize their use.

In Chapter 2 we showed that the successful estimate of the vapor fluxes (impossible to measure directly) from the residuals of discrete mass and/or energy balances is strongly limited by discretization errors. Residuals of the same order (or larger) may arise if finite difference approximations are used to compute fluxes and storage terms from discrete measurements, leading to a misinterpretation of the underlying physical process.

We demonstrated that residuals are very sensitive to the distance between the measurements and to the presence of nonlinear processes, which suggests the use of the energy balance instead of mass balance for residuals estimate. A careful assessment of the discretization errors is crucial for both diagnostic (results validation) and prognostic (experiments setup) use.

Misinterpretations of the physical processes arise not only because of an improper interpretation of the measurements, but also because measurements of fundamental quantities are of poor quality. Ground heat flux and soil moisture are two critical indicators of energy and moisture transfer in soil, and require to be accurately measured at whole scales.

In Chapter 5 we proved that ground heat flux, which is generally underestimated by classical probes (e.g. ground heat flux plates), is properly measured in both intensity and direction by multi functional heat pulse probes (MFHPPs), which can also provide soil moisture values. MFHPPs measure small soil volumes between equally spaced thermistors, and are therefore only weakly affected by discretization errors.

However, to monitor soil state in large-scale field applications, MFHPPs are not effective because of their small footprint, and other instrumentations are required.

## Chapter 7. Conclusions and Future Work

---

In Chapter 6 we investigated the possibility to infer distributed thermal conductivity and soil moisture profiles along a fiber optic cable, by applying the active distributed temperature sensing (ADTS) method. We showed good agreement with independent measurement in wet and intermediately wet soils, but a significant underestimation in dry conditions, which remains partially unexplained and requires further investigations.

In Chapter 3 we demonstrated the impossibility for the classical water-retention curves which approach infinite at residual saturations to properly describe the moisture-limited evaporation regime, which is typical of dry soils and dominated by vapor. By employing modified water-retention curves that allow vapor transport below residual saturation, we showed that simulations are more consistent with experiments, and predict vapor fluxes three times larger than the classical models.

In Chapter 4 we extended the comparison between classical and modified retention curves to the case of soils exposed to the diurnal atmospheric forcing. We established that the modified retention models predict larger evaporation, but also larger sensible and ground heat fluxes which might have implications for large-scale and global circulation models.

In summary, the present dissertation provided new insights into soil moisture and energy dynamics. We focused on three main sources of misinterpretations of physical processes (errors on measurements, errors on the use of measurements, errors on numerical parameterizations) which may have likely prevented from satisfactorily describing the coupled energy and mass transport, and we provided solutions. We proved that more reliable measurements can be obtained on a variety of spatiotemporal scales (Chapter 5 and Chapter 6), and we provided both diagnostic and prognostic methods to optimize their use (Chapter 2). Finally, we suggested an important improvement to be implemented in numerical model for better describing the vapor transport during dry regimes. The combined effects of these insights may certainly help to overcome the issues related to the modeling/measuring of vapor fluxes at the soil surface.

Many new questions and research opportunities emerged from this thesis.

An interesting challenge is certainly represented by the investigation of the ADTS method in the dry zone close to the soil surface. MFHPPs could be used in the same soil layer for comparison since, despite the different footprint, are based on the same principle.

Another interesting challenge is to obtain accurate matric potential measurements below residual, in order to carefully assess the shape of the extension of the water retention curves. As we demonstrated in Chapter 3, the predictions may differ significantly according to the model employed.

Proper implementation in large scale coupled land-surface models of the energy and moisture

---

dynamics in soils requires to account for the extended water-retention curves provided in Chapter 3 and Chapter 4. As demonstrated, their impact on large scale phenomena such as evaporation, precipitation and runoff might be crucial.

Finally, attention should be focused on the validity of the local equilibrium assumption which we always invoked in this thesis and which considers an instantaneous phase change between liquid and vapor. At the soil surface this assumption is inaccurate and non-equilibrium models, allowing a relaxation time for the phase change should be implemented.



## **A Other Author's Contribution**

In this appendix is attached the full text of *Lunati et al.* [2012].

## On the use of spatially discrete data to compute energy and mass balance

Ivan Lunati,<sup>1</sup> Francesco Ciocca,<sup>2</sup> and Marc B. Parlange<sup>2</sup>

Received 29 February 2012; accepted 13 April 2012; published 22 May 2012.

[1] In many practical applications the state of field soils is monitored by recording the evolution of temperature and soil moisture at discrete depths. We theoretically investigate the systematic errors that arise when mass and energy balances are computed directly from these measurements. We show that, even with no measurement or model errors, large residuals might result when finite difference approximations are used to compute fluxes and storage term. To calculate the limits set by the use of spatially discrete measurements on the accuracy of balance closure, we derive an analytical solution to estimate the residual on the basis of the two key parameters: the penetration depth and the distance between the measurements. When the thickness of the control layer for which the balance is computed is comparable to the penetration depth of the forcing (which depends on the thermal diffusivity and on the forcing period) large residuals arise. The residual is also very sensitive to the distance between the measurements, which requires accurately controlling the position of the sensors in field experiments. We also demonstrate that, for the same experimental setup, mass residuals are sensitively larger than the energy residuals due to the nonlinearity of the moisture transport equation. Our analysis suggests that a careful assessment of the systematic mass error introduced by the use of spatially discrete data is required before using fluxes and residuals computed directly from field measurements.

**Citation:** Lunati, I., F. Ciocca, and M. B. Parlange (2012), On the use of spatially discrete data to compute energy and mass balance, *Water Resour. Res.*, 48, W05542, doi:10.1029/2012WR012061.

### 1. Introduction

[2] Conservation laws are of great importance in the description of physical systems: quantitative predictions are based on mathematical models that describe the evolution of conserved quantities such as mass, momentum components, or energy. When comparing with experimental data, conservation principles can be invoked either to evaluate the quality of the model (an incomplete balance might indicate that additional physicochemical processes need to be considered), or to estimate, from the residual, quantities that cannot be directly measured (typically fluxes).

[3] Since conservation laws can be satisfied only within the experimental accuracy, it is important to establish how different error sources limit the accuracy of the experimental balance. A typical example of the difficulties in closing conservation laws with field data is the energy-budget problem at the land surface [e.g., Foken, 2008], where the role played by the ground heat storage term to obtain a reliable

heat flux estimate has become evident [Heusinkveld *et al.*, 2004; Liebethal *et al.*, 2005].

[4] There are several possible error sources in field data: measurement errors (due to the limited accuracy of the instrument or inaccurate calibration); modeling errors (e.g., due to an incomplete physical description or inappropriate boundary conditions); or parameter uncertainty (accentuated by the presence of heterogeneous structures, which can be treated in a stochastic framework, e.g., by applying kriging for spatial interpolation [Matheron, 1973]). Here we investigate the error introduced by the use of spatially (and temporally) discrete measurements to compute fluxes and storages.

[5] Discrete fluxes have been extensively used in the gradient method [Tanner, 1963] to compute heat flux in field soils [e.g., Kimball *et al.*, 1976; Cobos and Baker, 2003; Liebethal *et al.*, 2005; Assouline *et al.*, 2010] or snow [e.g., Jeffries and Morris, 2006; Sturm *et al.*, 2001], and, more recently, diffusive fluxes of greenhouse gases during soil respiration [Hirano, 2005; Barron-Gafford *et al.*, 2011; Wolf *et al.*, 2011]. The residual of discrete balance equations is also often used to estimate sensible [Sharratt *et al.*, 1992] or latent heat flux at the land surface [Mayocchi and Bristow, 1995; Castelly and Snyder, 2010]; vapor fluxes in field soils [Parlange *et al.*, 1998; Cahill and Parlange, 1998]; subsurface soil water evaporation [Heitman *et al.*, 2008a, 2008b]; or ground surface temperature [Bhumralkar, 1975; Lin, 1980].

[6] The use of quantities (fluxes or storage) estimated directly from discrete measurements makes these approaches prone to discretization error. Although it is well known from

<sup>1</sup>Institute of Geophysics, University of Lausanne, Lausanne, Switzerland.

<sup>2</sup>School of Architecture, Civil and Environmental Engineering, EPF Lausanne, Lausanne, Switzerland.

Corresponding author: I. Lunati, Institute of Geophysics, University of Lausanne, Amphipole - UNIL SORGE, 1015 Lausanne, Switzerland. (ivan.lunati@unil.ch)



numerical analysis that this error can be arbitrarily reduced by decreasing the distance between the measurement points, in practice several physical limitations (e.g., the finite size or the finite footprint of the sensors) and logistic constraints (e.g., the maximum number of probes available or manageable in a field campaign) set an upper limit to the highest possible spatial resolution. Therefore, it becomes important to assess not only the order of the discretization scheme, but also the absolute value of the error that is introduced and depends on initial and boundary conditions.

[7] In section 2 we consider the idealized case of heat conduction under harmonic temperature forcing; the soil is assumed semi-infinite with homogenous heat capacity and thermal conductivity such that the solution depends only on the time and the vertical coordinate, and the problem can be analytically solved. Due to the mathematical similarity between Fourier's, Darcy's, Fick's, and Ohm's laws, the analysis can be easily extrapolated to the case of Darcian flow, Fickian diffusion, or Ohmic electric current.

[8] In real field soils, however, the diurnal cycle causes not only heat conduction, but also mass flow, in which soil-moisture dynamics plays an important role. In section 2.4 we consider the more complex case of coupled heat and moisture transport. Although it is again assumed that the soil is homogeneous, model parameters vary in space due to variation of soil moisture and temperature, which evolve in time. Also in this case, we assume horizontal homogeneity and the problem is reduced to one-dimensional vertical balance equations, as it is common praxis in most field data analyses.

## 2. Heat Conduction With Harmonic Forcing

[9] We consider heat conduction in a homogenous semi-infinite medium without internal sources. Under these assumptions, the flux is proportional to the vertical temperature gradient, i.e.,  $j_z = -\lambda \partial_z T$  (horizontal fluxes are zero), and the thermal energy density can be expressed as  $m = c_v T$ . Although we specifically investigate the heat equation, the analysis presented here naturally applies to any conserved quantity whose mass balance include a diffusive term (e.g., Darcian flow, Fickian mass transport, or Ohmic charge transport).

[10] Since the volumetric heat capacity  $c_v$  and the thermal conductivity  $\lambda$  are constant, the energy balance equation takes the form

$$\frac{\partial}{\partial t} T(z, t) = D \frac{\partial^2}{\partial z^2} T(z, t), \quad (1)$$

where we have defined the thermal diffusivity  $D = \lambda/c_v$ . Equation (1) is the classic heat transfer equation, which has been extensively studied [e.g., *Carslaw and Jaeger*, 1959]. Here we are interested in the temperature evolution when the surface forcing is a harmonic function of time, i.e.,

$$T(0, t) = T_s(t) = A_s \cos \omega t, \quad (2)$$

where  $A_s$  is the amplitude at the surface,  $\omega = 2\pi/\tau$  is the angular frequency, and  $\tau$  is the period of the forcing. Under these assumptions and at sufficiently large times, the

solution is independent of the initial conditions and takes the simple form

$$T(z, t) = A_s e^{-kz} \cos(\omega t - kz), \quad (3)$$

where

$$k = \sqrt{\omega/2D}$$

is the wave number, and  $k^{-1}$  is called penetration depth. Equation (3) describes an exponentially damped temperature wave penetrating the medium with constant velocity  $\omega/k$ ; in other words, temperature oscillations decrease exponentially with the depth, while maxima and minima are delayed by a time interval that increases linearly with the depth. We remark that in the more general case of forcing terms involving multiple frequencies (i.e., also for arbitrary forcing terms which can be decomposed into its constituent frequencies via a Fourier transform), each frequency can be analyzed independently as long as the problem can be considered linear.

### 2.1. Exact Energy Balance for a Layer of Finite Thickness

[11] Let us consider the horizontal layer between depth  $z_T$  and  $z_B$ . The energy balance (per unit horizontal area) for the layer can be obtained by integrating equation (1) over the depth interval  $[z_T, z_B]$ . To simplify calculations that involve trigonometric functions, we work in complex notation and define the temperature solution (equation (3)) as the real part of the complex function

$$\Theta(z, t) = A_s e^{-kz} e^{i(\omega t - kz)}, \quad (4)$$

which is solution of a heat transfer equation analogous to equation (1), i.e.,  $\partial_t \Theta = D \partial_{zz} \Theta$ , but with complex forcing  $\Theta(0, t) = A_s e^{i\omega t}$ . The storage term is the real part of

$$Q(t) = c_v \int_{z_T}^{z_B} \frac{\partial}{\partial t} \Theta(z, t) dz, \quad (5)$$

and the flux difference the real part of

$$F(t) = \lambda \int_{z_T}^{z_B} \frac{\partial^2}{\partial z^2} \Theta(z, t) dz = [f(z_T, t) - f(z_B, t)], \quad (6)$$

where the real part of

$$f(z, t) = -\lambda \frac{\partial}{\partial z} \Theta(z, t) = \lambda k(i+1) \Theta(z, t) \quad (7)$$

is the flux at depth  $z$  and time  $t$ .

### 2.2. Finite-Difference Approximation

[12] In practice, temperature measurements are available at few discrete locations and only approximate energy storage and fluxes can be computed. Let us suppose that data are available at three different depths ( $z_U$ ,  $z_C$ , and  $z_D$ ) as depicted in Figure 1. In this case, only finite difference approximations of the fluxes can be computed. A first-order

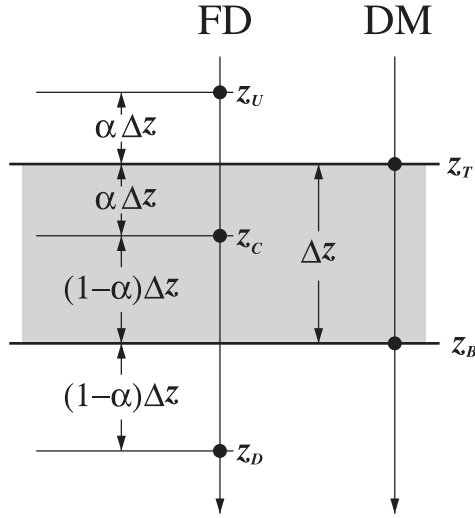


**Figure 1.** The control interval for the finite difference (FD, left) and the direct flux measurement (DM, right) methods.

finite-difference (FD) approximation of equations (5) and (6) yields

$$Q_{\text{FD}}(t) = \Delta z c_v \frac{d}{dt} \Theta(z_C, t) = i\omega \Delta z c_v \Theta(z_C, t) \quad (8)$$

and

$$F_{\text{FD}}(t) = \frac{\lambda}{2\Delta z} \left[ \frac{\Theta(z_D, t) - \Theta(z_C, t)}{(1-\alpha)} - \frac{\Theta(z_C, t) - \Theta(z_U, t)}{\alpha} \right], \quad (9)$$

respectively.

[13] With three temperature measurements, higher-order approximations of the storage term can be computed by linear interpolation of temperature profile between measurements points, which yields the linearly interpolated finite-difference (LFD) approximation

$$Q_{\text{LFD}}(t) = i\omega \Delta z c_v \left\{ \frac{3}{4} \Theta(z_C, t) + \frac{1}{4} [\alpha \Theta(z_U, t) + (1-\alpha) \Theta(z_D, t)] \right\}. \quad (10)$$

[14] Note that both equations (9) and (10) depend on the parameter  $\alpha$ , which measures the relative position of  $z_C$  in the layer: if  $\alpha = 1/2$  the layer is centered on  $z_C$ ; if  $\alpha < 1/2$ ,  $z_C$  is closer to the top of the layer; and if  $\alpha > 1/2$ ,  $z_C$  is closer to the bottom (Figure 1).

### 2.3. Direct Flux Measurement (DM) and Force-Restore Method Approximation

[15] Since it is experimentally possible to measure heat flux, e.g., by employing a heat flux plate (HFP), it is of interest to consider an experimental setup in which fluxes and temperatures are measured at depth  $z_T$  and  $z_B$  (Figure 1). Our goal here is to isolate the effects of the discretization error on the energy balance closure, therefore, we neglect the problem of the accuracy of HFP measurements, including the issues related to the determination of soil properties

and distortion of heat flow field [Philip, 1961; Fuchs and Hadas, 1973]. We simply assume that flux measurements at depth  $z_T$  and  $z_B$  are available, such that  $f(z_T, t)$  and  $f(z_B, t)$  are known exactly.

[16] Under these optimistic assumptions, the only error originates from the discretization storage term, which can be approximated as the real part of

$$Q_{\text{DM}}(t) = i\omega \Delta z c_v [w\Theta(z_B, t) + (1-w)\Theta(z_T, t)]. \quad (11)$$

[17] The parameter  $w$  has been introduced to consider the cases in which the temperature is measured at a single depth or at both depths. The case  $w = 1/2$  corresponds to a linear temperature interpolation in the layer; if  $z_T = 0$  this discretization corresponds to the one employed in the formulation of the force-restored method by Lin [1980]. (From equation (7) it is straightforward to show that  $f(z, t) = Dk[\partial_t \Theta(z, t)/\omega + \Theta(z, t)]$ .) If temperature is measured at a single location, we have either  $w = 0$  or  $w = 1$ ; if  $z_T = 0$ , the case  $w = 1$  corresponds to the original force-restore method of Bhumralkar [1975].

### 2.4. Energy Residual

[18] If storage and flux terms were exactly known (equations (5) and (6)) the residual is identically zero,  $Q(t) - F(t) \equiv 0$ . In practice, however, only approximate storage and fluxes can be computed from discrete data, and the energy balance does not close exactly. The energy budget errors, which originates from discretization and depends on the forcing frequency and on medium properties, can be easily quantified by computing the relative residual.

[19] For the first-order finite-difference approximation, the energy residual normalized by the amplitude of the storage term is given by the real part of

$$R_{\text{FD}}(t) = \frac{Q_{\text{FD}}(t) - F_{\text{FD}}(t)}{|Q_{\text{FD}}|} = r_{\text{FD}}(\alpha, k\Delta z) \frac{Q_{\text{FD}}(t)}{|Q_{\text{FD}}|}, \quad (12)$$

which is a harmonic function of time with angular frequency  $\omega$  equal to the forcing term. The complex function  $r_{\text{FD}} = 1 - F_{\text{FD}}/Q_{\text{FD}}$  (whose analytic expression is given in Appendix A) depends on the relative position of  $z_C$  in the layer  $\alpha$  and on dimensionless layer thickness  $k\Delta z$ , i.e., the layer thickness normalized by the penetration depth  $1/k$ . The modulus of  $r_{\text{FD}}$  is the amplitude of the normalized residual  $|r_{\text{FD}}| = |R_{\text{FD}}|$ , whereas its argument  $\phi_{\text{FD}} = \arg(r_{\text{FD}})$  is the phase shift with respect to the storage term  $Q_{\text{FD}}$ . (Note that  $Q_{\text{FD}}$  has a positive phase shift,  $\pi/2$ , with respect to the temperature at  $z_C$ .)

[20] Figure 2 shows the temporal evolution of storage, flux difference, and residual over one period for a harmonic diurnal forcing ( $\tau = 24$  h). A thermal diffusivity of  $4 \times 10^{-7} \text{ m}^2 \text{ s}^{-1}$ , typical of soil, is used and it is assumed that the layer thickness is 7.5 cm and the central measurement lies 4.5 cm from the top of the layer ( $\alpha = 3/5$ ). In this example, the amplitude of the energy residual is 22% of the approximate storage-term amplitude, and a negative phase shift of about 7.5 h with respect to the approximate storage term.

[21] This simple example shows that the balance cannot be easily closed with discrete data even in absence of

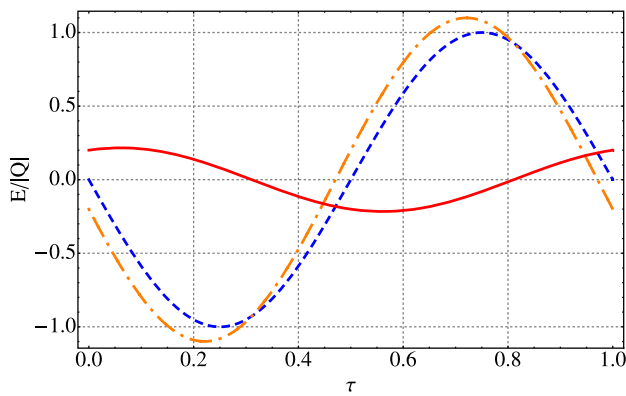


**Figure 2.** Storage term (dashed line), flux term (dot-dashed line), and residual (solid) line as a function of time (period fraction). The medium has thermal diffusivity  $D = 4 \times 10^{-7} \text{ m}^2 \text{ s}^{-1}$  and the forcing term has period  $\tau = 1d$ , which results in a penetration depth  $1/k = 10.5 \text{ cm}$ ; the layer thickness is  $\Delta z = 7.5 \text{ cm}$  ( $k\Delta z = 0.72$ ) and  $\alpha = 3/5$ . Under these conditions the amplitude of the dimensionless residual is  $|R_{\text{FD}}| = 0.22$  and the phase shift  $\phi_{\text{FD}}/2\pi = -0.31$  with respect to the storage term.

modeling and measurement errors; in field conditions energy budget is not expected to close exactly for a layer of arbitrary finite size. The penetration depth is a key parameter to determine the energy residual for a given layer thickness or to estimate the maximum thickness required to keep the residual below a desired threshold. The penetration depth depend both on the properties of the medium and on the forcing period (the values corresponding to different land-surface materials are reported in Table 1). For measurements in field soils under the natural diurnal solar forcing, the 1 day period is particularly relevant and corresponds to a penetration depth that typically ranges from 6 to 12 cm.

[22] The dependence of the normalized residual on the dimensionless layer thickness is shown in Figure 3, where the residuals of the first-order finite-difference  $|R_{\text{FD}}|$ , the linear finite-difference  $|R_{\text{LFD}}|$ , and discrete flux measurements  $|R_{\text{DM}}|$  approximations are compared. (The definition of  $|R_{\text{LFD}}|$  and  $|R_{\text{DM}}|$  are analogous to equation (12) and are given explicitly in Appendix A.) For a layer thickness of the order of the penetration depth,  $k\Delta z \approx 1$ , the energy-budget

error can be severe. The FD approximation of the residual varies between 10% and 50% of the storage term depending on  $\alpha$ , and it remains between 10% and 20% of the storage term when the LFD approximation is employed for the storage term. For a given dimensionless thickness, the residual is very sensitive to the position of the midsensor. If the midsensor is exactly in the center of the layer,  $\alpha = 1/2$ , the error decrease quadratically when the dimensionless thickness is decreased, whereas it decreases only linearly if  $\alpha \neq 1/2$  (see Appendix A and Figures 3a and 3b).

[23] When direct information on the fluxes is available, one can use the DM approximation. In this case, relying only on single temperature measurements (at the top,  $w = 0$ , or at the bottom,  $w = 1$ , of the interval) leads to severe unbalance (Figure 3c). Only the choice  $w = 1/2$ , corresponding to a linear temperature interpolation in the layer, gives acceptable results with an error of the order of 20% of storage-term amplitude for layer thickness equal to the penetration depth.

### 3. Soil-Moisture and Energy Balance Under Evaporative Conditions

[24] In this section we consider the more complex case of a partially saturated soil subject to temperature and evaporative forcing. The evolution of the soil state is described by a system of coupled equations for mass and energy conservation. According to the standard models used in the description of field soils [e.g., Philip and de Vries, 1957; de Vries, 1958], we describe the state of the soil by the (liquid) soil moisture  $\theta_L$  (volume occupied by the liquid water divided by the total volume) and by the temperature.

[25] The conservation equation for the total soil moisture, which includes both the liquid and the vapor component, can be written as

$$\frac{\partial}{\partial t} [\rho_L(T)\theta_L + \rho_V(\theta_L, T)(\phi - \theta_L)] = -\frac{\partial}{\partial z} [j_L(\theta_L, T) + j_V(\theta_L, T)], \quad (13)$$

where  $\phi$  is the porosity;  $\rho_L$  and  $\rho_V$  are the density of the liquid and vapor, respectively; and  $j_L$  and  $j_V$  are the liquid and vapor flux, respectively. In equation (13) we assume that vapor and liquid are in thermodynamic equilibrium and neglect vapor advection (see Appendix B).

**Table 1.** Thermal Diffusivity  $D$  ( $\text{m}^2 \text{ s}^{-1}$ ) and Penetration Depth  $1/k$  (m) for Different Materials and Different Forcing Periods  $\tau$

	$D$ ( $\text{m}^2 \text{ s}^{-1}$ )	$1/k$ (m)					
		$\tau = 1 \text{ yr}$	$\tau = 1 \text{ day}$	$\tau = 0.5 \text{ day}$	$\tau = 1 \text{ h}$	$\tau = 1 \text{ min}$	$\tau = 1 \text{ s}$
Quartz sand, dry	$2.0 \times 10^{-7} \text{ a}$	1.42	0.074	$5.2 \times 10^{-2}$	$1.5 \times 10^{-2}$	$2.0 \times 10^{-3}$	$2.5 \times 10^{-4}$
Quartz sand, water 8.3%	$3.4 \times 10^{-7} \text{ a}$	1.85	0.097	$6.8 \times 10^{-2}$	$2.0 \times 10^{-2}$	$2.5 \times 10^{-3}$	$3.3 \times 10^{-4}$
Sandy clay, water 15.0%	$3.8 \times 10^{-7} \text{ a}$	1.95	0.102	$7.2 \times 10^{-2}$	$2.1 \times 10^{-2}$	$2.7 \times 10^{-3}$	$3.5 \times 10^{-4}$
Soil (average)	$4.6 \times 10^{-7} \text{ b}$	2.15	0.112	$8.0 \times 10^{-2}$	$2.3 \times 10^{-2}$	$3.0 \times 10^{-3}$	$3.8 \times 10^{-4}$
Calcareous earth, water 43.0%	$1.9 \times 10^{-7} \text{ a}$	1.38	0.072	$5.1 \times 10^{-2}$	$1.5 \times 10^{-2}$	$1.9 \times 10^{-3}$	$2.5 \times 10^{-4}$
Snow (fresh)	$5.0 \times 10^{-7} \text{ b}$	2.24	0.127	$8.3 \times 10^{-2}$	$2.4 \times 10^{-2}$	$3.1 \times 10^{-3}$	$4.0 \times 10^{-4}$
Snow (densely packed)	$4.1 \times 10^{-7} \text{ a}$	2.03	0.106	$7.5 \times 10^{-2}$	$2.2 \times 10^{-2}$	$2.8 \times 10^{-3}$	$3.6 \times 10^{-4}$
Water	$1.4 \times 10^{-7} \text{ b}$	1.20	0.063	$4.5 \times 10^{-2}$	$1.3 \times 10^{-2}$	$1.7 \times 10^{-3}$	$2.1 \times 10^{-4}$

<sup>a</sup>Ingersoll and Koeppe [1924].

<sup>b</sup>Carlsaw and Jaeger [1959].

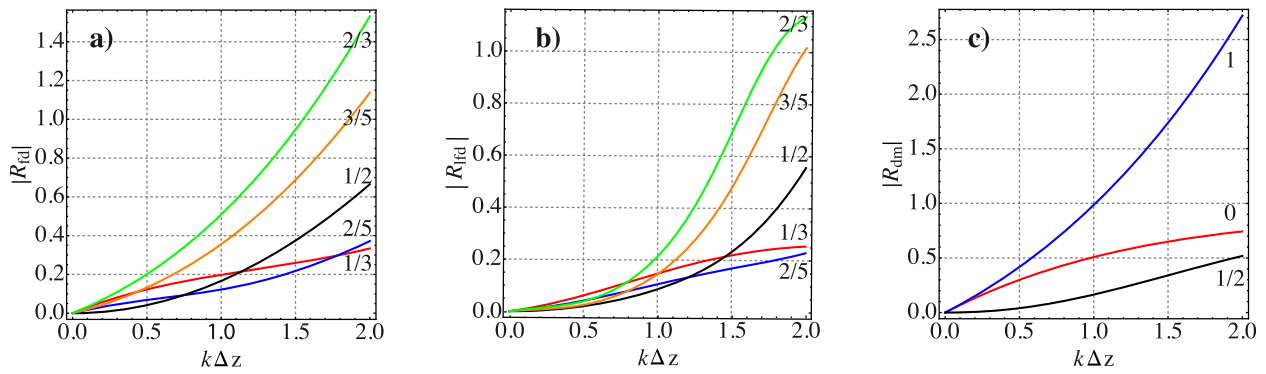


**Figure 3.** Comparison of amplitude of the dimensionless residual among (a) the first-order finite-difference approximation  $|R_{FD}|$ ; (b) the linear finite-difference approximation  $|R_{LFD}|$ ; and (c) the discrete flux measurement  $|R_{dm}|$ . Shown are the curves corresponding to different relative position of the central sensor  $\alpha$  (Figure 1) for the finite-difference approximations and to different values of  $w$  for the discrete flux measurement.

[26] The energy-balance equation is

$$\frac{\partial}{\partial t}[C(\theta_L, T)T] = \frac{\partial}{\partial z} \left\{ \lambda(\theta_L) \frac{\partial T}{\partial z} \right\} - \frac{\partial}{\partial z} [L(T)j_V(\theta_L, T) + c_L T[j_L(\theta_L, T) + j_V(\theta_L, T)]], \quad (14)$$

where  $C$  is the soil heat capacity, which includes the contribution of solid, liquid, and vapor;  $\lambda$  is the thermal conductivity of the soil;  $L$  is the latent heat of vaporization at temperature  $T$ ; and  $c_L$  is the specific heat of liquid water. The specific forms of the functions appearing in equations (13) and (14) are given in Appendix B.

### 3.1. A Numerical Test Case: Evaporation From a Soil Bucket

[27] To investigate mass and energy residuals in case of simultaneous heat and soil-moisture transfer, we consider the problem of evaporation from a soil bucket similar to the experiment by *Assouline et al.* [2010]. A soil bucket of height 25 cm is thermally insulated and can exchange heat and mass only through the soil surface at the upper boundary. We consider three different soils (sand, loam, and clayey loam) with different hydraulic parameters. The Mualem-Van-Genuchten model [*Mualem*, 1976; *van Genuchten*, 1980] is used for matric potential and relative conductivity; whereas the dependence of the thermal conductivity on the soil moisture is described by an empirical model [*Chung and*

*Horton*, 1987]. The relevant parameters are given in Table 2 for the different soils.

[28] At the soil surface we assign a harmonic temperature forcing (with 24 h period and peak-to-peak amplitude 15°C) and a periodic evaporation. The daily evaporative flux is described by Morlet wavelets (Figure 4), and three cycles are considered. The evaporative fluxes applied to the loam and the clayey loam buckets have been reduced by a factor of 2 and 4, respectively, with respect to the evaporation in the sand in order to compensate the lower conductivity and avoid the drying of the surface. Before starting the three evaporation cycles, the system is left relaxing under the sole temperature forcing us to allow the soil moisture to reach a nearly hydrostatic equilibrium.

[29] The numerical solution is computed on a one-dimensional (1-D) grid consisting of 250 cells (1 mm spatial resolution) and with a constant time discretization of 60 s. The coupled equations describing soil-moisture and energy balance (equations (13) and (14)) are discretized by a time-implicit finite-volume scheme. The resulting temperature and soil-moisture solutions are considered the true profiles in the bucket.

[30] To simulate the acquisition of experimental data, the profiles are sampled at discrete locations and used to compute the discrete mass and energy balances. We consider three sets of discrete data characterized by a different depth of the central measurement, i.e.,  $z_C = 4$  cm ( $\alpha = 1/3$ ), 5.5 cm ( $\alpha = 1/2$ ), and 7 cm ( $\alpha = 2/3$ ). In all

**Table 2.** Hydraulic and Thermal Parameters for the Different Soil Types

	Hydraulic Properties <sup>a</sup>						Thermal Properties <sup>b</sup>			Matrix Properties <sup>c</sup>
	$K_s$ (m s <sup>-1</sup> )	$\alpha$ (1 m <sup>-1</sup> )	$m$ (-)	$n$ (-)	$\theta_r$ (-)	$\phi$ (-)	$b_1$ (W m <sup>-1</sup> °C)	$b_2$ (W m <sup>-1</sup> °C)	$b_3$ (W m <sup>-1</sup> °C)	$C_s = \rho_s c_s$ (J m <sup>-1</sup> 3°C)
Sand	$5.25 \times 10^{-5}$	7.25	0.627	2.68	0.045	0.43	0.228	-2.406	4.909	$1.92 \times 10^6$
Loam	$2.89 \times 10^{-6}$	3.6	0.359	1.56	0.078	0.43	0.243	0.393	1.534	$1.92 \times 10^6$
Clayey Loam	$7.22 \times 10^{-7}$	1.9	0.237	1.31	0.095	0.41	-0.197	-0.962	2.521	$1.92 \times 10^6$

<sup>a</sup>*Carsel and Parrish* [1988].

<sup>b</sup>*Chung and Horton* [1987].

<sup>c</sup>*de Vries* [1963].

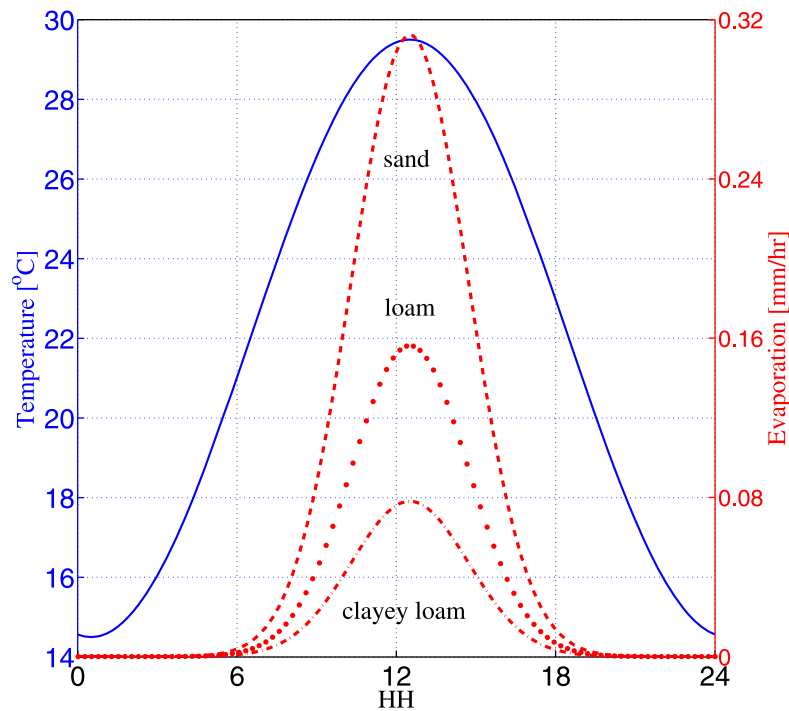


**Figure 4.** Temperature (solid line) and evaporation at the soil surface. The evaporation fluxes are described by Morlet wavelets with different maxima for different soils: the evaporation in loam (dotted line), respectively, clayey loam (dash-dotted line), is twice, respectively, four times, smaller than in sand (dashed line) in order to compensate for the reduced conductivity and avoid drying of the soil surface.

three data sets the position of the shallowest and deepest data are  $z_U = 1$  cm and  $z_D = 10$  cm, respectively, which corresponds to a control interval of thickness  $\Delta z = 4.5$  cm. An example of the soil moisture and temperature evolution for the loamy soil is shown in Figure 5 for the case  $\alpha = 2/3$ , together with the energy and mass balance obtained using a first-order finite difference (FD) approximation for the fluxes and the storage term.

### 3.2. Energy Residual

[31] For each type of soil and discrete data set an energy budget is calculated with the FD scheme. Figure 5c shows the storage term, the convective, and conductive fluxes together with the residual for the loamy soil with  $\alpha = 2/3$ ; all quantities are normalized by the amplitude of the storage term. In the case considered here, conduction is the dominant heat transport mechanism and the contribution of heat convection to the normalized residual is small. Therefore, the energy residual is well described by the analytical solution in equation (12). For a loam moisture between 0.21 and 0.29, the thermal diffusivity is approximately  $D = 3.7 \times 10^{-7} \text{ m}^2 \text{ s}^{-1}$ , which corresponds to a penetration depth  $k^{-1} = 0.1$  m for a 1 day period. The resulting normalized residual for  $\Delta z = 0.045$  m and  $\alpha = 2/3$  is 0.17, which is in good agreement with the residual in Figure 5c.

[32] The energy residuals for all soils and data set are reported in Figure 6, which shows the daily amplitudes of the residuals normalized by the daily amplitude of the heat storage term. The residual is well described by the analytic solutions plotted in Figure 3 (the case considered here corresponds to a dimensionless control interval thickness  $k\Delta z$

of approximately 0.3 for sand, 0.4 for loam, and 0.5 for clayey loam). Also in case of a relatively thin control interval ( $\Delta z = 4.5$  cm), the residuals due to the use of spatially discrete data remain large and very sensitive to the position of the central measurement. For all soils, residuals are about 4% if measurements are equally spaced ( $\alpha = 1/2$ ), but increases rapidly when the measurements point are not uniformly distributed (reaching 18% in case of clayey loam and  $\alpha = 2/3$ ).

### 3.3. Mass Residual

[33] The same analysis is performed for the mass balance equation and the mass residual is computed by a first-order finite difference (FD) scheme. The temporal evolution of the mass residual for the loamy soil with  $\alpha = 2/3$  is shown in Figure 5d, together with the storage term and the liquid flux contribution. The peak-to-peak amplitude varies from 80% of the storage term in the first evaporative cycle, to more than 100% in the third cycle. These mass balance errors are much larger than the energy-balance errors for the same data set (Figure 5c). This is caused by the highly nonlinear nature of the mass balance equation due to the dependence of relative conductivity and matric potential on the water content. Nonlinear effects tend to become larger in dryer media and lead to larger residuals for later evaporative cycles.

[34] The peak-to-peak amplitude of the residual normalized by the peak-to-peak amplitude of the storage term are shown in Figure 7a for all soils and data sets (i.e.,  $\alpha = 1/3, 1/3, 2/3$ ). Even for the relatively close measurements considered here, the normalized residuals are larger

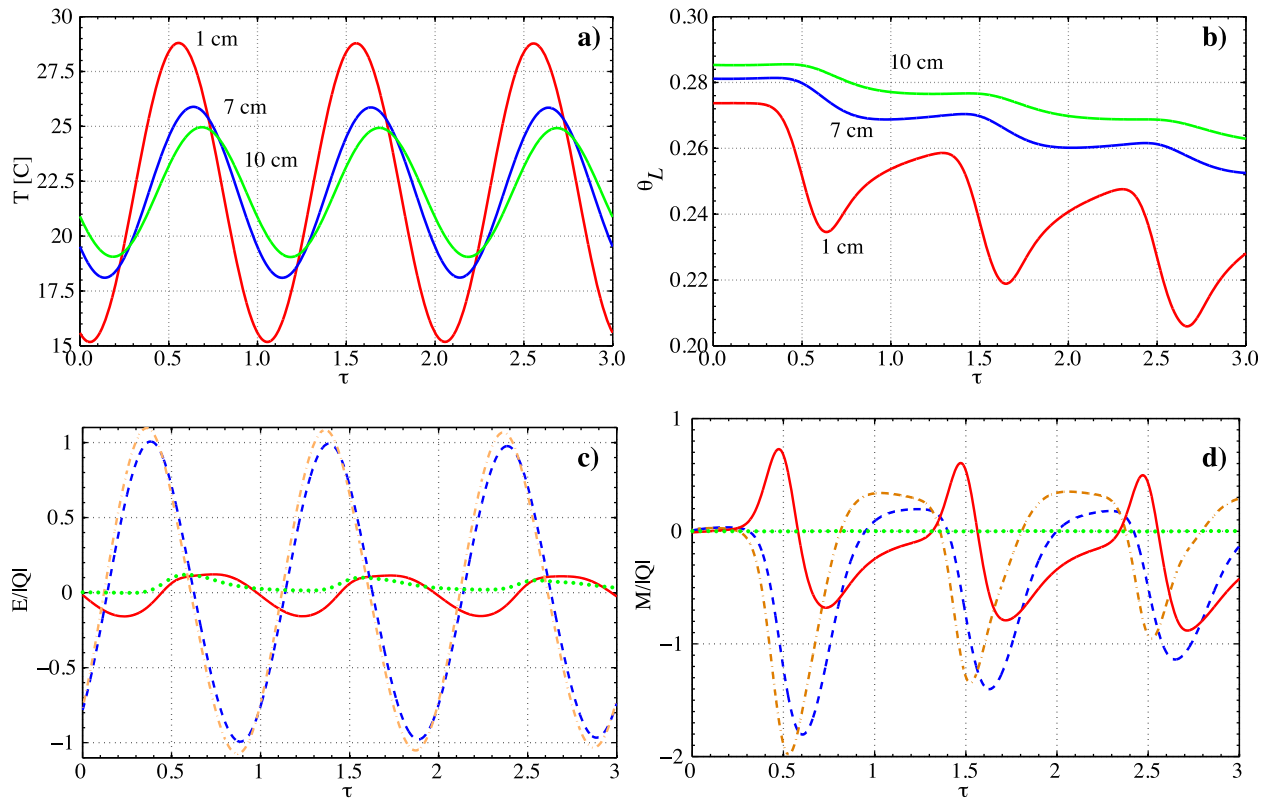


**Figure 5.** (a) Simulated temperature and (b) soil-moisture evolution at three different depths for the loamy soil. These depths correspond to a control layer of thickness  $\Delta z = 4.5$  cm and  $\alpha = 2/3$ . An analysis of the energy balance with (c) this discrete data shows that the contribution of the convective heat fluxes (dotted line) is small compared to the conductive heat flux (dot-dashed line) and the storage (dashed line). The normalized energy residual (solid line) is  $|R_{FD}| \approx 0.14$ . The analysis of the (d) soil moisture balance yields a much larger normalized residual (solid line); the contribution of vapor fluxes (dotted line) is negligible compared to liquid flux (dot-dashed line) and storage (dashed line).

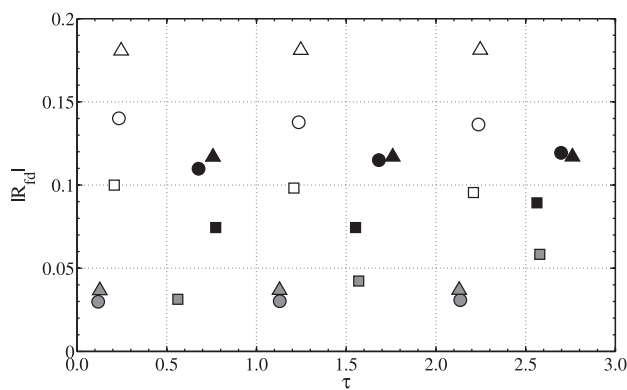


**Figure 6.** Normalized energy balance residual computed with the FD scheme: daily amplitudes for sand (squares), loam (circles), and clayey loam (triangles); the colors correspond to different values of  $\alpha$ , i.e., 1/3 (black), 1/2 (gray), and 2/3 (white). For each evaporative cycle, symbols are placed at the time corresponding to the minimum (most negative) residual.

than 27% in all cases. In contrast to energy residuals, the smallest mass residuals are not obtained for equally spaced measurements ( $\alpha = 1/2$ ), but when the midmeasurement is closer to the surface ( $\alpha = 1/3$ ). This is again due to the nonlinearity of liquid fluxes, which is stronger closer to the surface, where the soil is dryer; having the closer shallowest measurements allows a better description of the fluxes in this critical region, yielding smaller residuals.

[35] The use of the LFD scheme provides to a more accurate estimation of the storage term and leads to a decrease of the residual (Figure 7b). The improvement is particularly sensitive for sand and loam, as well as for data sets with equally spaced measurements ( $\alpha = 1/2$ ). In case of clayey loam, however, improvements are limited, because the mass balance error is dominated by the inaccurate estimate of the shallowest fluxes, which is not improved by the LFD scheme.

### 3.4. Cumulative Residual

[36] In the simple case of pure heat conduction with harmonic forcing (section 2), the residual is a harmonic function of time with angular frequency equal to the forcing term (equation (12)) and the cumulative residual calculated over an integer multiple of the period is zero.

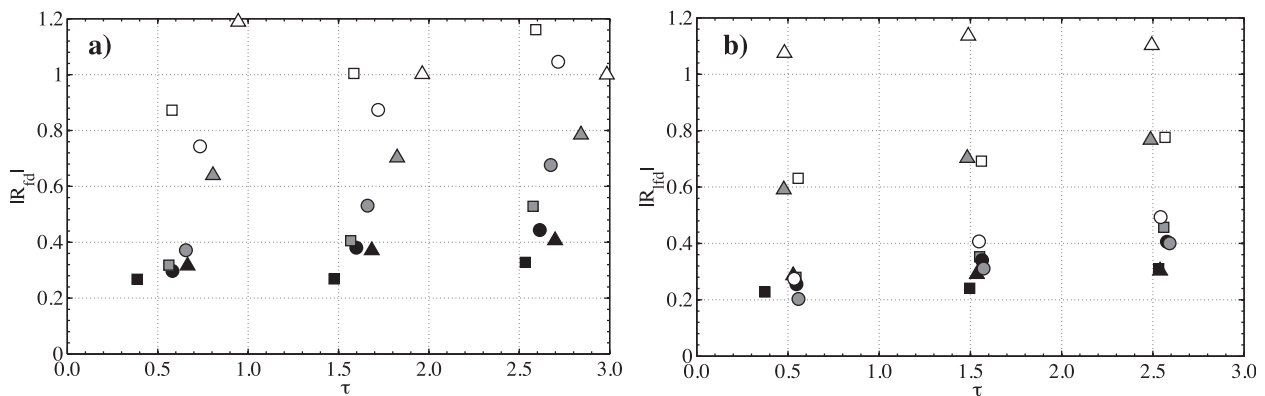


**Figure 7.** Normalized mass balance residual computed with (a) the FD scheme and (b) with the LFD scheme: daily amplitudes for sand (squares), loam (circles), and clayey loam (triangles); the colors correspond to different values of  $\alpha$ , i.e.,  $1/3$  (black),  $1/2$  (gray), and  $2/3$  (white). For each evaporative cycle, symbols are placed at the time corresponding to the minimum (most negative) residual.

[37] In the case of coupled heat and moisture transfer the situation is more complex due to the presence of an evaporative trend and to the intrinsic nonlinearity of the problem, which leads to interaction between frequencies. This is illustrated in Figure 8, which plots the cumulative energy and the mass residuals in loamy soil for  $\Delta z = 0.045$  m and  $\alpha = 2/3$  (Figure 5). A clear negative trend is visible in the cumulative mass residual indicating that the error due to the use of discrete fluxes and accumulation terms does not average out at longer time scale. We observe that the observed trend is consistent with the drying of the bucket. In a field situation, where measurements of vapor flux and storage are not available, this residual could be misinterpreted as a real subsurface evaporation.

#### 4. Conclusions

[38] The use of spatially discrete data to compute energy and mass balance can lead to large residuals in case of periodic forcing, as in case of field measurements where the solar radiation induces a clear diurnal cycle both for surface

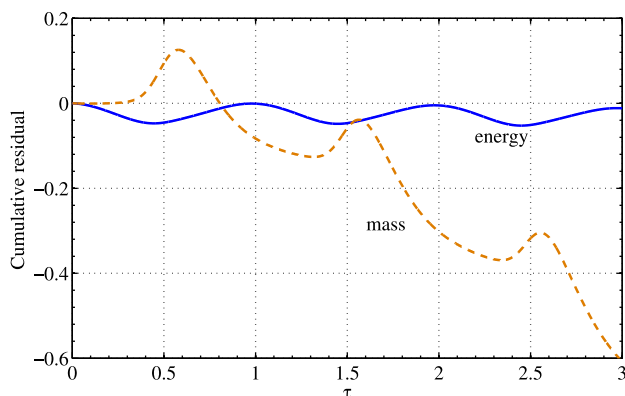


**Figure 8.** Cumulative mass (dotted line) and energy (solid line) residuals for the loamy soil. These cumulative residuals correspond to the data in Figure 5 and are normalized by the peak-to-peak amplitude of the corresponding storage term. The control layer has thickness  $\Delta z = 4.5$  cm and  $\alpha = 2/3$ .

temperature and evaporation. These large residuals appear also without experimental or model errors, and when there is no uncertainty on soil properties: they are solely due to the finite spatial resolution of the data, which is unable to capture the nonlinear temperature and water-content profiles with a satisfactory level of accuracy. If fluxes, storage or residuals computed directly from discrete field measurements are used, this systematic error needs to be quantified because they provide information on the accuracy with which mass or energy balances can be closed for a soil layer.

[39] Considering the case of purely conductive heat transport in homogeneous media, we have shown that residuals up to 20% can be expected for realistic parameters. A key parameter controlling the residual is the penetration depth, which depends both on the forcing period and on the thermal diffusivity. Larger residuals are expected in poorly conductive or highly capacitive soils, as well as in presence of high-frequency forcing. To obtain a satisfactory balance closure, it is necessary to consider control layers which are sufficiently smaller than the penetration depth. Also, the position of the midsensor plays an important role. Errors are smaller when measurements are equally spaced, but they rapidly increase for other experimental configurations.

[40] We have derived analytical solutions to estimate the residual as a function of the layer thickness and the position of the measurements. A layer thickness comparable to the penetration depth (which is of the order of few centimeters for a typical soil subject to diurnal forcing) leads to large residuals, which are very sensitive to the measurement positions and require a careful control of the sensor depth. Our analytical solution can help to design field experiments that enable monitoring fluxes with the desired accuracy.

[41] Although we have discussed the case of conduction dominated heat transport, the results naturally extend to any problem which is diffusion dominated (with fairly homogeneous diffusivity) and provide an indication of the applicability of the gradient based method to compute field fluxes. (In particular, they naturally extend to recent applications of the gradient method to compute diffusive gas fluxes during soil respiration).

[42] By means of numerical simulations, we have also investigated the more complex (and realistic) case of simultaneous moisture and heat transfer in different types of soil (sand, loam, and clayey loam). We have shown that, for the numerical test cases considered here, the energy residual can be described with good approximation by the analytical solution.

[43] The water mass residual, however, has a more complex behavior. We have demonstrated that also for situations in which the energy residual is acceptable, the mass residual is very large. Larger residuals (comparable to the storage term) are obtained for loam and clayey loam due to the lower hydraulic conductivity. The larger mass residuals are caused by the nonlinear nature of liquid fluxes, which is due to the dependence of relative conductivity and matric potential on the water contents.

[44] Our results suggest that a careful assessment of the systematic mass error introduced by the use of spatially discrete data is required before using fluxes and residuals estimated from field measurements.

### Appendix A: Analytical Expressions of the Residual Functions

[45] For any discretization method,  $j = \text{FD, LFD, DM}$ , the normalized residual is

$$R_j(t) = \left(1 - \frac{F_j(t)}{Q_j(t)}\right) \frac{Q_j(t)}{|Q_j(t)|} = r_j(\alpha, \zeta) \frac{Q_j(t)}{|Q_j(t)|},$$

where the complex function  $r_j$  describe the residual in terms of the normalized storage. The flux difference and the storage of the FD method can be written directly from equations (8) and (9). Defining  $\zeta = k\Delta z$  we can readily write

$$\frac{\lambda F_{\text{FD}}}{2\Delta z} = \frac{-1 + (1 - \alpha)e^{2\alpha(1+i)\zeta} + \alpha e^{-2(1-\alpha)(1+i)\zeta}}{\alpha(1 - \alpha)} \Theta(z_C, t)$$

and

$$\frac{\lambda Q_{\text{FD}}}{2\Delta z} = 4i\zeta^2 \Theta(z_C, t),$$

respectively. It immediately follows that

$$r_{\text{FD}}(\alpha, \zeta) = 1 - i \frac{1 - (1 - \alpha)e^{2\alpha(1+i)\zeta} - \alpha e^{-2(1-\alpha)(1+i)\zeta}}{4(1 - \alpha)\alpha\zeta^2},$$

which tends to zero as  $r_{\text{FD}}(\frac{1}{2}, \zeta) \approx -\frac{i}{6}\zeta^2$ , if  $\alpha = 1/2$  and as  $r_{\text{FD}}(\alpha, \zeta) \approx \frac{2}{3}(i+1)(1-2\alpha)\zeta$ , if  $\alpha \neq 1/2$ .

[46] For the LFD scheme,

$$\frac{\lambda Q_{\text{LFD}}}{2\Delta z} = i\zeta^2 \cdot [3 + \alpha e^{2\alpha(1+i)\zeta} + (1 - \alpha)e^{-2(1-\alpha)(1+i)\zeta}] \Theta(z_C, t)$$

yields

$$r_{\text{LFD}}(\alpha, \zeta) = 1 - \frac{i}{\alpha(1 - \alpha)\zeta^2} \frac{1 - (1 - \alpha)e^{2\alpha(1+i)\zeta} - \alpha e^{-2(1-\alpha)(1+i)\zeta}}{3 + \alpha e^{2\alpha(1+i)\zeta} + (1 - \alpha)e^{-2(1-\alpha)(1+i)\zeta}},$$

which tends to zero as  $r_{\text{LFD}}(\frac{1}{2}, \zeta) \approx \frac{i}{12}\zeta^2$ , if  $\alpha = 1/2$  and as  $r_{\text{LFD}}(\alpha, \zeta) \approx \frac{1}{6}(i+1)(1-2\alpha)\zeta$ , if  $\alpha \neq 1/2$ .

[47] For the DM approximation

$$\frac{\lambda F_{\text{DM}}}{2\Delta z} = \frac{\lambda F}{2\Delta z} = 2\zeta(i+1)[1 - e^{-(i+1)\zeta}] \Theta(z_T, t)$$

and

$$\frac{\lambda Q_{\text{DM}}}{2\Delta z} = 4i\zeta^2 [we^{-(i+1)\zeta} + (1-w)] \Theta(z_T, t)$$

lead to

$$r_{\text{DM}}(w, \zeta) = 1 - \frac{(1-i)}{2\zeta} \frac{1 - e^{-(1+i)\zeta}}{we^{-(1+i)\zeta} + (1-w)}.$$

### Appendix B: Parameterization

[48] The liquid-water flux is defined according to the Darcy velocity

$$j_L(\theta_L, T) = -\rho_L(T)K(\theta_L, T)[\partial_z \psi(\theta_L, T) + 1], \quad (\text{B1})$$

where

$$K(\theta_L, T) = [\mu_L(T_0)/\mu_L(T)]K_r(\theta_L)K_{\text{sat}} \quad (\text{B2})$$

is the unsaturated hydraulic conductivity, which depends on the saturated value  $K_{\text{sat}}$ . The dependence of the physical properties of liquid water on the temperature is described by the following relationships:

$$\rho_L(T) = (d_1 + d_2 T - d_3 T^2) \text{ kg m}^{-3}, \quad (\text{B3})$$

$$\mu_L(T) = e^{-c_1 - c_2/T + c_3/T^2} \text{ kg m}^{-1} \text{ s} \quad (\text{B4})$$

(with  $d_1 = 658.2$ ,  $d_2 = 2.509 \text{ K}$ ,  $d_3 = 4.6 \times 10^{-3} \text{ K}^2$ ,  $c_1 = 6.434$ ,  $c_2 = 2414 \text{ K}$ , and  $c_3 = 6.673 \times 10^5 \text{ K}^2$ ). The dependence of the relative conductivity  $K_r$  and the matric potential  $\psi$  on the water content is described by the Mualem–van-Genuchten model, i.e.,

$$K_r(\theta_L) = S_{\text{eff}}^{-1/2} [1 - (1 - S_{\text{eff}}^{1/m})^m]^2, \quad (\text{B5})$$

$$\psi(\theta_L, T) = -[\gamma(T)/\gamma(T_0)]\alpha^{-1}(S_{\text{eff}}^{-1/m} - 1)^{1/n}, \quad (\text{B6})$$

where the effective saturation  $S_{\text{eff}} = \frac{\theta_L - \theta_{LR}}{\theta_{LM} - \theta_{LR}}$  depends on the residual  $\theta_{LR}$  and maximum  $\theta_{LM} = \phi$  water content; and the function  $\gamma(T)$  describes the dependence of the surface tension on the temperature.

[49] The water vapor density is described by the relationship

$$\rho_V(\theta_L, T) = \frac{a_0}{T} e^{a_1 - a_2/T - a_3 T} e^{\psi(\theta_L, T)g/R_V T} \quad (\text{B7})$$



(with  $a_0 = 10^{-3} \text{ kg m}^{-3} \text{ K}$ ,  $a_1 = 31.3716$ ,  $a_2 = 6014.79 \text{ K}$ ,  $a_3 = 7.92495 \times 10^{-3} \text{ K}$ , and  $R_V = 461.5 \text{ J kg}^{-1} \text{ K}$ ) and the vapor flux is assumed to be purely diffusive, i.e.,

$$j_V(\theta_L, T) = -D_V(\theta_L, T) \partial_z \rho_V(\theta_L, T), \quad (\text{B8})$$

where

$$D_V(\theta_L, T) = \frac{(\phi - \theta_L)^{10/3}}{\phi^2} D_{V,m}(T) \quad (\text{B9})$$

is the diffusion coefficient in the porous medium, and

$$D_{V,m}(T) = 2.12 \times 10^{-5} \left[ \frac{T}{273.15 \text{ K}} \right]^2 \text{ m}^2 \text{ s}^{-1} \quad (\text{B10})$$

is molecular diffusion coefficient of water vapor in air.

[50] Finally, the dependence of the thermal properties on the water content is given by

$$\begin{aligned} C(\theta_L, T) &= (1 - \phi) c_s \rho_s + c_L \rho_L(T) + L(T) (\phi - \theta_L) \rho_V(\theta_L, T) \\ \lambda(\theta_L) &= b_1 + b_2 \theta_L + b_3 \theta_L^{1/2}, \end{aligned} \quad (\text{B11})$$

where

$$L(T) = L_0 - (c_L - c_p)(T - T_0) \quad (\text{B12})$$

and  $c_L = 4182 \text{ J kg}^{-1} \text{ K}$ ,  $c_p = 1005 \text{ J kg}^{-1} \text{ K}$ ,  $L_0 = 2.453 \times 10^6 \text{ J kg}^{-1}$ ,  $T_0 = 20^\circ \text{C}$ .

[51] **Acknowledgments.** Ivan Lunati is Swiss National Science Foundation (SNSF) Professor at the University of Lausanne (SNSF grant number PP00P2-123419/1). Francesco Ciocca is supported by the SNSF grant number 200,021-1222088/1.

## References

- Assouline, S., K. Narkis, S. W. Tyler, I. Lunati, M. B. Parlange, and J. S. Selker (2010), On the diurnal soil water content dynamics during evaporation using dielectric methods, *Vadose Zone J.*, *9*, 709–718.
- Barron-Gafford, G. A., R. L. Scott, G. D. Jenerette, and T. E. Huxman (2011), The relative controls of temperature, soil moisture, and plant functional group on soil CO<sub>2</sub> efflux at diel, seasonal, and annual scales, *J. Geophys. Res.*, *116*, G01023, doi:10.1029/2010JG001442.
- Bhumralkar, C. M. (1975), Numerical experiments on the computation of ground surface temperature in an atmospheric general circulation model, *J. Appl. Meteor.*, *14*, 1246–1258.
- Cahill, A. T., and M. B. Parlange (1998), On water vapor transport in field soils, *Water Resour. Res.*, *34*(4), 73–739.
- Carsel, R. F., and R. S. Parrish (1988), Developing joint probability distributions of soil water retention characteristics, *Water Resour. Res.*, *24*(5), 755–769.
- Carlsaw, H. S., and J. C. Jaeger (1959), *Conduction of Heat in Solids*, Oxford University Press, Oxford, UK.
- Castellví, F., and R. L. Snyder (2010), A comparison between latent heat fluxes over grass using a weighing lysimeter and surface renewal analysis, *J. Hydrol.*, *381*, 213–220.
- Chung, S. O., and R. Horton (1987), Soil heat and water flow with a partial surface mulch, *Water Resour. Res.*, *23*(12), 2175–2186.
- Cobos, D. R., and J. M. Baker (2003), In situ measurement of soil heat flux with the gradient method, *Vadose Zone J.*, *2*, 589–594.
- de Vries, D. A. (1958), Simultaneous transfer of heat and moisture in porous media, *Trans. Am. Geophys. Union*, *39*(5), 909–916.
- de Vries, D. A. (1963), The thermal properties of soils, in *Physics of Plant Environment*, edited by R. W. van Wijk, pp. 210–235, North-Holland, Amsterdam.
- Foken, T. (2008), The energy balance closure problem: An overview, *Ecol. Appl.*, *18*(6), 1351–1367.
- Fuchs, M., and A. Hadas (1973), Analysis of the performance of an improved soil heat flux transducer, *Soil Sci. Soc. Am. Proc.*, *37*, 173–175.
- Heitman, J. L., R. Horton, T. J. Sauer, and T. M. De Sutter (2008a), Sensible heat observations reveal soil-water evaporation dynamics, *J. Hydro-meteorol.*, *9*, 165–171.
- Heitman, J. L., X. Xiao, R. Horton, and T. J. Sauer (2008b), Sensible heat measurements indicating depth and magnitude of subsurface soil water evaporation, *Water Resour. Res.*, *44*, W00D05, doi:10.1029/2008WR006961.
- Heusinkveld, B. G., A. F. G. Jacobs, A. A. M. Holtslag, and S. M. Berkowicz (2004), Surface energy balance closure in an arid region: Role of soil heat flux, *Agric. For. Meteorol.*, *122*, 21–27.
- Hirano, T. (2005), Seasonal and diurnal variations in topsoil and subsoil respiration under snowpack in a temperate deciduous forest, *Global Biogeochem. Cycles*, *19*, GB2011, doi:10.1029/2004GB002259.
- Ingersoll, L. R., and O. A. Koepp (1924), Thermal diffusivity and conductivity of some soil materials, *Phys. Rev.*, *24*, 92–93.
- Jeffries, M. O., and K. Morris (2006), Instantaneous daytime conductive heat flow through snow on lake ice in Alaska, *Hydrol. Processes*, *20*, 803–815.
- Kimball, B. A., R. D. Jackson, F. S. Nakayama, S. B. Idso, and R. J. Reginato (1976), Soil-heat flux determination: Temperature gradient method with computed thermal conductivities, *Soil Sci. Soc. Am. J.*, *40*, 25–28.
- Liebenthal, C., B. Huwe, and T. Foken (2005), Sensitivity analysis for two ground heat UX calculation approaches, *Agric. For. Meteorol.*, *132*, 253–262.
- Lin, J. D. (1980), On the force-restore method for prediction of ground surface temperature, *J. Geophys. Res.*, *85*, 3251–3254.
- Matheron, G. (1973), The intrinsic random functions and their applications, *Adv. Appl. Prob.*, *5*, 439–468.
- Mayocchi, C. L., and K. L. Bristow (1995), Soil surface heat flux: Some general questions and comments on measurements, *Agric. For. Meteorol.*, *75*, 43–50.
- Mualem, Y. (1976), A new model for predicting the hydraulic conductivity of unsaturated porous media, *Water Resour. Res.*, *12*(3), 513–522.
- Parlange, M. B., A. T. Cahill, D. R. Nielsen, J. W. Hopmans, and O. Wendroth (1998), Review of heat and water movement in field soils, *Soil Tillage Res.*, *47*, 5–10.
- Philip, J. R. (1961), The theory of heat flux meters, *J. Geophys. Res.*, *66*, 571–579.
- Philip, J. R., and D. A. de Vries (1957), Moisture movement in porous materials under temperature gradients, *Trans. Am. Geophys. Union*, *38*(2), 222–232.
- Sharratt, B. S., G. S. Campbell, and D. M. Glenn (1992), Soil heat flux estimation based on the finite-difference form of the transient heat flow equation, *Agric. For. Meteorol.*, *61*, 95–111.
- Sturm, M., J. Holmgren, and D. K. Perovich (2001), Spatial variations in the winter heat flux at SHEBA: Estimates from snow-ice interface temperatures, *Ann. Glaciol.*, *33*, 213–220.
- Tanner, C. B. (1963), Basic instrumentation and measurements for plant environment and micrometeorology, *Soils Bull.*, *6*, Dep. of Soil Sci., Univ. of Wisconsin, Madison.
- van Genuchten, M. T. (1980), A closed-form equation for predicting hydraulic conductivity of unsaturated soils, *Soil Sci. Soc. Am. J.*, *44*, 892–898.
- Wolf, B., W. Chen, N. Brueggemann, X. Zheng, J. Pumpanen, and K. Butterbach-Bahl (2011), Applicability of the soil gradient method for estimating soil atmosphere CO<sub>2</sub>, CH<sub>4</sub>, and N<sub>2</sub>O fluxes for steppe soils in Inner Mongolia, *J. Plant Nutr. Soil Sci.*, *174*, 359–372.



# Francesco Ciocca

[f.ciocca83@gmail.com](mailto:f.ciocca83@gmail.com)

Italian, born 1983

Languages: Italian (native), English (fluent), French (fluent), German (beginner)

## Education

---

- |           |  |
|-----------|--|
| 2009-2013 | <b>Ph.D. candidate in Environmental Engineering</b><br>École Polytechnique Fédérale de Lausanne (EPFL), Lausanne, CH<br><i>Moisture and Energy Dynamics in Field Soils: the Influence of the Diurnal Cycle</i> . Advisors: Prof. M.B. Parlange and Prof. I. Lunati |
| 2005-2008 | <b>M.Sc. in Environmental Physics</b><br>Università di Torino, Turin, Italy<br><i>Acoustic waves propagation in seawater by Tappert's parabolic equation (in italian)</i> . Advisor: Prof. A. Osborne  |
| 2002-2005 | <b>B.Sc. in Physics</b><br>Università di Torino, Turin, Italy  |

## Professional Summary

---

- |           |  |
|-----------|--|
| 2010-2013 | Teaching assistant at EPFL, analysis I, II and hydrology |
| 2008-2009 | Mathematics teacher at the high school in Turin, Italy   |

## Awards

---

- |      |   |
|------|---|
| 2010 | Outstanding Student Paper Award, American Geophysical Union |
|------|---|

## Publications

---

**Ciocca F.**, I. Lunati and M.B. Parlange (2013), Effects of the Water-Retention Curve on Evaporation from Dry Soils, *Geophysical Resource Letters*, under review.

**Ciocca F.**, I. Lunati, N. van de Giesen, M.B. Parlange (2012), Heated Optical Fiber for Distributed Soil-Moisture Measurements: A Lysimeter Experiment, *Vadose Zone Journal*, Special issue on Inverse Modeling and Parameter Estimation,  
DOI: 10.2136/vzj2011.0199

Lunati I., **Ciocca F.** and M.B. Parlange (2012), On the use of spatially discrete data to compute energy and mass balance, *Water Resources Research*, 48, W05542,  
DOI: 10.1029/2012WR012061

## Reviewer Assignments

---

Hydrology and Earth System Sciences